EMANATION STUDIES

and

SOME NUCLEAR REACTIONS INDUCED BY PROTONS ON IODINE

by

V.P. Narang, M.Sc.

A thesis submitted to the Faculty of Graduate Studies and Research in partial fulfilment of the requirements for the degree of Doctor of Philosophy

Department of Chemistry,
McGill University,
Montreal.

June 1963.

ACKNOWLEDGEMENTS

It is my pleasure gratefully to acknowledge the guidance, criticism, and encouragement received from Professor L. Yaffe through the entire course of this work.

The use of the cyclotron, even at odd hours, was made available through the courtesy of Professor R.E. Bell and through the very kind assistance of Mr. R.H. Mills.

The suggestions and help offered by Drs. T.M. Kavanagh and E.C.B. Pederson and other colleagues of the Radiation Laboratory are gratefully appreciated.

I wish to express my thanks to all my colleagues in the Radiochemistry Laboratory for helpful discussions, particularly Drs. A. Kjelberg and H. Taniguchi who helped me at the beginning of this work.

I also thank Mrs. C. Macfarlane for her help in typing the manuscript and Mrs. M.S. Lafleur, Mr. D.R. Sachdev and Mr. G.B. Saha for proof reading this thesis; also Mr. D.A. Marsden for his assistance with the drawings.

Finally, I wish to express my gratitude to the Department of Chemistry, McGill University, for financial assistance in the form of Research Assistantships and Demonstratorships.

TABLE OF CONTENTS

PART A

PART B

PART A

1. INTRODUCTION

1.1 EMANATION PROCESS

The name Emanation is commonly employed for Element number 86. This nomenclature is, however, not strictly adhered to, since the names Radon and Emanon have also been used for the same element.

The word emanation also refers to the escape of radioactive inert gases from the materials in which they are formed, e.g. Radon from Radium, Krypton and Xenon from the substances undergoing fission[1].

The phenomenon of escape of radioactive inert gases has been exploited in many fields since its discovery. Before dealing with this phenomenon in detail a term called 'Emanating Power', which is used very often in this connection, needs clarification. Hahn[2] was the first to point out that whenever a radioactive inert gas atom is formed as a daughter product of its parent there is a finite probability for its escape, depending upon the physical properties and chemical constitution of its parent and the physical properties of the radioactive inert gas atom itself. Hahn coined the term 'Emanating power' which he defined as the fraction of radioactive inert gas atoms formed in the solid that escapes from the surface of the solid. Thus

$$\text{Emanating Power } (E) = \frac{\text{No. of radioactive inert gas atoms escaped from the surface}}{\text{Total no. of radioactive inert gas atoms formed in the substance}}$$

This definition of Emanating Power implies that E of a substance could be a function of composition, specific surface, crystal structure, temperature of the substance, half-life of the inert gas escaping, and the recoil energy imparted to the radioactive inert gas atoms. The dependence of E, on as many as six parameters, makes the practical determination and mathematical formulation of the system somewhat complicated and in many cases almost impossible.

1.2 THEORY OF THE EMANATION PROCESS

As soon as the radioactive inert gas atoms are formed from the decay of its parent, there could be two possible ways of their escape, viz.

(a) If the parent atoms lie near the surface of the solid bearing them, the recoil energy might be enough to drive them out from the surface of the solid, or

(b) If the radioactive inert gas atoms fail to escape by recoil, there is another possibility that they might escape by diffusion before decay to the ground state.

On the basis of these two possibilities, the first attempt to formulate a theory was made by Ratner[3] and a similar attempt was later made by Flügge and Zimens[4]. The basis of both theories was essentially the same, except that the latter had a stronger mathematical background.

According to Flügge and Zimens[4] the experimental

sample is normally in the form of powder and hence it was presumed that the substance to be studied retains its crystalline form even in the powder state. Thus a single grain of this powder is the repetition many times of the primary crystal unit. This crystal unit has a well-established geometrical shape and dimensions. A number of such primary units form larger units, called secondary particles or grains. If somehow the emanating power of such secondary particles could be established, then it is possible to formulate the emanating power of the entire experimental sample since it is an aggregate of the secondary units.

1.2.1 Emanating power of a single grain

The emanating power of a single grain is due to two different processes according to Flügge and Zimens, viz.

(a) Recoil, and

(b) Diffusion.

The emanating power, E, will be the sum of the two processes. Thus

$$E = E_R + E_D \quad \ldots\ldots\ldots\ldots\ldots\ldots \quad (1)$$

where E_R and E_D stand for emanating power due to recoil and diffusion respectively.

1.2.2 Emanating power due to recoil

Assuming that the concentration of parent atoms is constant in time (during the course of an experiment) and in space, the fraction E_R will be appreciable if the parent atoms

lie near the surface or on the surface or, more precisely, within the recoil range R.

The problem arises when parent atoms lie somewhere inside the grain-lattice and are heterogeneously distributed inside the solid grain. Thus it was assumed that they are homogeneously distributed.

Further, as soon as the radioactive inert gas atom is formed, it has equal probability of going deeper into the surface or escaping by means of direct recoil.

Flügge and Zimens[4] on these considerations derived for a spherical grain the following expression for E_R,

$$E_R = 3/4 \left(\frac{R}{r_o}\right) - 1/16 \left(\frac{R}{r_o}\right)^3 \quad \ldots\ldots\ldots\ldots (2)$$

where R and r_o stand for recoil range and radius of the grain respectively.

For larger grains of dimensions $\sim 10^{-6}$ cm, the expression (2) can be approximated as

$$E_R = 3/4 \left(\frac{R}{r_o}\right). \quad \ldots\ldots\ldots\ldots\ldots\ldots (3)$$

The ratio $3/r_o$ can be replaced by the ratio surface/volume of the sphere and therefore

$$E_R = \frac{R}{4} \left(\frac{\text{surface}}{\text{volume}}\right)$$

$$= \frac{R}{4} \rho \left(\frac{\text{surface}}{\text{mass}}\right) \quad \ldots\ldots\ldots\ldots\ldots (4)$$

where ρ stands for the density of the substance.

J. Kurbatov[5] independently derived an expression for E_R of a cubical grain of edge, $a \gg R$, as

$$E_R = 6\frac{(a - 2R)^2}{4a^3}R + 12\frac{(a - 2R)}{a^3}R^2(0.447) + 8(\frac{R}{a})^3(0.597) \quad \ldots\ (5)$$

The first, second, and third terms in expression (5) stand for the emanating power due to recoil from regions near the faces, near the edges, and near the corners respectively.

But careful study of the expression (5) reveals it could be simplified to the expression (4) given by Flügge and Zimens, if the larger grain size is taken.

The expression (4) does not contain any term which allows for the shape of the grain, and thus it could be applied to any sample.

1.2.3 Emanating power due to diffusion

It is generally accepted that permeation of gases through a continuous solid barrier is a complicated phenomenon, involving a sequence of processes, adsorption of the gases at the interfaces and diffusion through the solid barrier and finally evaporation at the surface. Among all these usually the diffusion is slowest and hence constitutes the rate-determining step.

Diffusion occurs transversely through the lattices along the interface. These interfaces, however, are statistically distributed over the grain so that in the calculation of the total diffusion current passing through

the outer surface one assumes, in order to simplify the calculations, that the grain is homogeneous in all respects.

The diffusion current passing through the surface is further slowed down when it reaches a point near the surface, since here the concentration of radioactive inert gas atoms is higher and the gas-filled pores offer considerable resistance to the diffusion current. The work of Chamie[6] shows that the presence of water vapour offers a positive hindrance and that even the pore size has an effect[7] on the diffusion current.

Taking all these points into consideration, and assuming that there is no adsorption taking place, Flügge and Zimens[4] formulated an expression for emanation power due to diffusion alone as

$$E_D = \frac{3}{2y^2}\left\{\frac{1}{x} - \frac{1}{x}\frac{\sinh y(1-x)}{\sinh y} - 1\right\}$$

$$+ \frac{3}{2y}\left\{\left(1 - \frac{x}{2} - \frac{1}{xy^2}\right)\coth y + \frac{1}{xy^2}\frac{\cosh y(1-x)}{\sinh y}\right\} \quad \ldots\ldots (6)$$

where $x = \frac{R}{r_o}$, $y = r_o\sqrt{\lambda/D}$.

λ is the decay constant of the gas, D is the diffusion coefficient of the radioactive inert gas and R and r_o the recoil range and radius of the grain respectively.

For the larger grain the equation (6) reduces to

$$E_D = \frac{3}{y} = \frac{3}{r_o\sqrt{\lambda/D}}$$

$$= \sqrt{\frac{D}{\lambda}} \left(\frac{\text{surface}}{\text{volume}}\right)$$

$$= \sqrt{\frac{D}{\lambda}} \rho \left(\frac{\text{surface}}{\text{mass}}\right) \quad \ldots\ldots\ldots\ldots\ldots\ldots (7)$$

Thus the total emanating power of a single grain is

$$E = E_R + E_D$$

$$= \left(\frac{R}{4} + \sqrt{\frac{D}{\lambda}}\right) \rho \left(\frac{\text{surface}}{\text{mass}}\right) \quad \ldots\ldots\ldots\ldots\ldots (8)$$

1.2.4 Factors governing emanating power

(a) Effect of temperature:

Temperature has the least effect on E_R, since thermal energies are of the order of 0.025 ev (15°C) to 0.1 ev (higher temperatures) while recoil energies are very high in comparison with thermal energies.

However, diffusion processes are temperature dependent. The dependence of E_D on temperature is given by the relation[4]

$$E_D = Ae^{-E_e/RT} \quad \ldots\ldots\ldots\ldots\ldots\ldots\ldots (9)$$

where A and E_e are constants, R is the gas constant, and T the absolute temperature. E_e is the activation energy, which is experimentally determined, and is given[4] by

$$E_e = \frac{E_D}{2} \quad \ldots\ldots\ldots\ldots\ldots\ldots\ldots\ldots (10)$$

(b) Effect of porosity:

It is a well-established fact that diffusion of

gases through solids is slower than through gases. Thus a highly porous substance will have a high emanating power unless it adsorbs the radioactive inert gas. Diffusion will be rapid even at thermal energies if there is free gas space above the sample. This conclusion can be reached from the consideration of the pore lengths and diameters and inert gas diffusion velocity and is essential to the explanation of the high emanating power of many preparations like Barium palmitate and Barium caproate observed by Strassmann[8]. It was also shown[4,9,10,11] that compressibility has little effect on emanating power of the substance.

(c) Adsorption of inert gas:

If the substance adsorbs the inert gas, its emanating power decreases considerably. This fact was illustrated by various workers[12,13,14,15] for a variety of substances like $Fe(OH)_3$, $Cr(OH)_3$, Fe_2O_3, chabazite, etc., etc.

(d) Indirect recoil effect:

When a recoiling inert gas atom from a grain continues to pass through the lattice spaces of a neighbouring grain (by diffusion) and then escapes from the surface of the solid, Zimens[9] called this a result of indirect recoil.

Thus the total emanating power due to recoil is

$$E_R = E_{R_i} + E_{R_d} \qquad \ldots\ldots\ldots\ldots\ldots (11)$$

where E_{R_i} and E_{R_d} are due to indirect and direct recoil

respectively. Erbacher[16] attributes the high emanating power of some metal hydroxides to be due to the indirect recoil effect. Gotte[17] believed that the indirect recoil effect is very dependent upon the composition of the solid alone.

Zimens[4,9] postulated that a recoil atom, before it slows down to thermal energies, melts a small region of the order 100 Å in diameter along its path. A sort of molten pocket is formed in the grain. This molten pocket may re-solidify in a distorted condition, and that inert gas atoms may diffuse through this distorted material more rapidly than through the normal solid.

1.2.5 Methods of introducing indicator systems

In most of the experiments carried out by the Hahn school in Germany, the following systems of indicators were used:

$_{90}Th^{228}$ (Rd.Th.) $\xrightarrow{\alpha}$ 1.91 y. $_{88}Ra^{224}$ (Thx) $\xrightarrow{\alpha}$ 3.64 d. $_{86}Em^{220}$ (Tn) $\xrightarrow{\alpha}$ 52 s.

$_{88}Ra^{226}$ $\xrightarrow{\alpha}$ 1621 y. $_{86}Em^{222}$ (Rn) $\xrightarrow{\alpha}$ 3.82 d.

$_{88}Ra^{223}$ (Acx) $\xrightarrow{\alpha}$ 11.6 d. $_{86}Em^{219}$ $\xrightarrow{\alpha}$ 3.92 s.

In all the substances to be examined by the emanation method, the introduction of Rd.Th, Radium and Thx was made by common physical and chemical methods. The homogeneous distribution of the parent substance[18] into the substance studied was the major consideration. This was achieved by

co-crystallization when the components form mixed crystals, with metal oxide gels by co-precipitation by means of ammonia or alkali; with zeolites by exchange of bases; and with metals by electrolysis or simple mixing of the ingredients by melting.

1.3 PRACTICAL APPLICATIONS OF EMANATION METHODS

1.3.1 A brief review of applications

Voluminous literature exists dealing with the application of emanation methods. Most of the work in this field was done by the school of Hahn and Zimens in Germany. Among the earliest applications were the studies of the aging of gels, colloids, and hydroxides of some metals. Changes in specific surface were noted, which were due to the shrinkage of the surface with time and hence decrease in emanating power was observed. Reversibility and irreversibility of the emanating power of gels were also studied. All this work is recorded in a review by Hahn[19]. The works of Erbacher[16] and Graue[20] are also relevant in this connection.

Emanation methods were also employed to study the crystal-structure changes and the thermal behaviour of some inorganic compounds. Zimens[21] studied the effect of temperature on calcite and aragonite, the hexagonal and rhombic forms of $CaCO_3$, using the $Ra^{224} \xrightarrow{\alpha} Rn^{220}$ system. The results of these experiments are shown in Fig. 1. The

Figure 1

HEATING CURVES OF CALCITE AND ARAGONITE

Reproduced from K.E. Zimens, Z. physik. Chem. B37, 231 (1937) (Ref. 21)

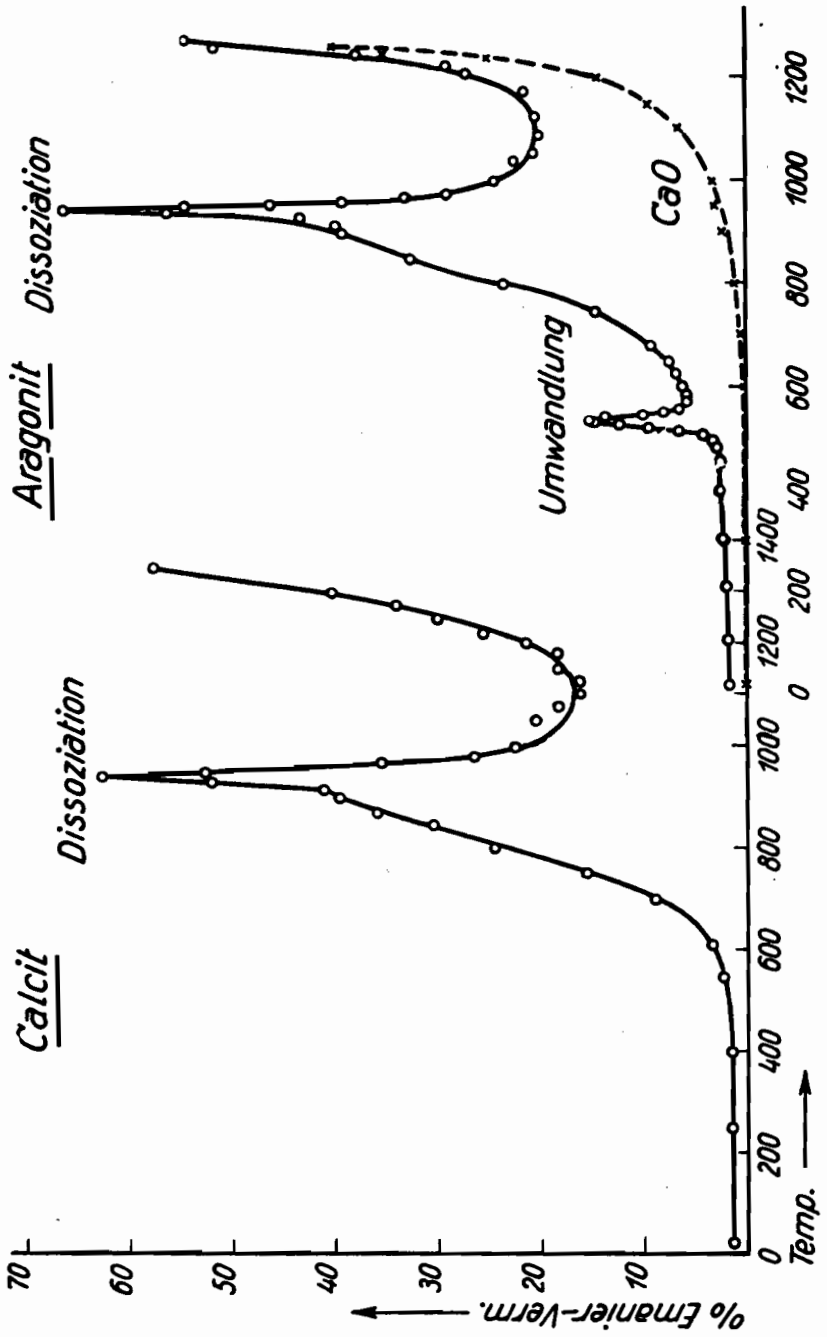
Calcit
Dissoziation
Aragonit
Dissoziation
Umwandlung
CaO
% Emanier-Verm.
Temp.
0
200
400
600
800
1000
1200
1400
10
20
30
40
50
60
70

peaks at 920°C in both cases are associated with the decomposition of $CaCO_3$ into CaO and CO_2. The peak at 530°C in the aragonite curve is associated with the transition of aragonite to calcite. These results were confirmed by taking Debye-Scherrer X-ray photographs at various temperatures.

A similar study by Tammann and Sworykin[22] on $BaSO_4$ shows there was a sudden increase in emanating power at one particular temperature. The explanation given was that a rapid rise of emanating power, which occurs at a definite temperature, is due to lattice 'loosening', and the temperature at which this happens is known as 'loosening temperature'. An extensive study by Tammann shows that this value lies somewhere between 0.5 to 0.6 of the absolute melting point. $BaCl_2$, $Ba(NO_3)_2$, and KNO_3 were similarly studied, and a type of molecular shift in the solid state was proposed. It was suggested that at this temperature reactivity in the solid state begins.

Jagitsch[23] studied the reaction

$$PbO + SiO_2 \longrightarrow PbSiO_3$$

using the $Th^{228} \xrightarrow{\alpha} Ra^{224} \xrightarrow{\alpha} Rn^{220}$ system. It was found that at higher temperatures the emanating power decreases rapidly due to formation of $PbSiO_3$ which has a low emanating power. A review by Hahn[24] on reactions in the solid state, as evidenced by the emanation method, was recently published.

Reviews of the applications of emanation methods were published by Zimens[25] and Hahn[18] which include the developments up to 1942 and 1949 respectively.

An excellent article on emanation methods was contributed by Wahl[26] which incorporated all the developments up to 1950 and in brief the theory of Flügge and Zimens[4].

Cooke and Prout[27] using I^{132} which grows from Te^{132}, instead of using the $Ra^{224} \xrightarrow{\alpha} Rn^{220}$ system, investigated the thermal behaviour of $BaSO_4$, K_2SO_4, and Na_2SO_4.

Zhabrova et al.[28] recently studied the dehydration of the hydroxides of Mg, Ni, Zn, Al, Zr, and Th by the emanation method.

1.3.2 Present work

In the present work the author studied the thermal behaviour of halides using the

$$I^{135} \xrightarrow{\beta^-} Xe^{135}$$

system. The halides selected for this work are of Ag, Cu(I), Hg(II), Tl(I), and Pb(II). The temperature region in which the proposed study was made was from 15°C to 200°C, since some halides have phase transitions in this region of temperature.

It was also proposed to study the validity of the Tammann 'loosening temperature' theory for these halides.

1.4 GENERAL METHODS FOR RADIATION DETECTION AND RADIOACTIVE EMANATION DETECTION

1.4.1 Brief review of detection systems

In spite of the fact that a variety of methods and systems are known to the modern radiochemist which could be employed for specialized detection problems, nevertheless classical methods cannot be ignored, and a knowledge of them is essential since they are still widely used. Price[29], Siegbahn[30], Gatrousis et al.[31] and many others[32,33,34] recently reviewed all the classical and modern techniques for nuclear radiation detection.

The classical methods make use of the ionization chambers, proportional counters, and Geiger-Muller (G-M) tubes. Each of these detector types employs gas-filled chambers.

Consider a gas-filled metallic tube, through which an insulated anode wire is suspended, with a high voltage applied to the anode. The passage of charged particles produces ion pairs within the chamber, and the ionization current thus produced is a function of the voltage applied.

If now the pulse height is plotted against the applied voltage, a line is obtained as shown in Fig. 2. The curve is divided into four main regions.

In region I there is competition between loss of ion pairs by recombination and removal of the charge by collection at the anode. With increasing field, the drift

Figure 2

SCHEMATIC ILLUSTRATION OF THE VARIATION OF THE PULSE SIZE WITH VOLTAGE APPLIED TO A GEIGER-MULLER COUNTER(29)

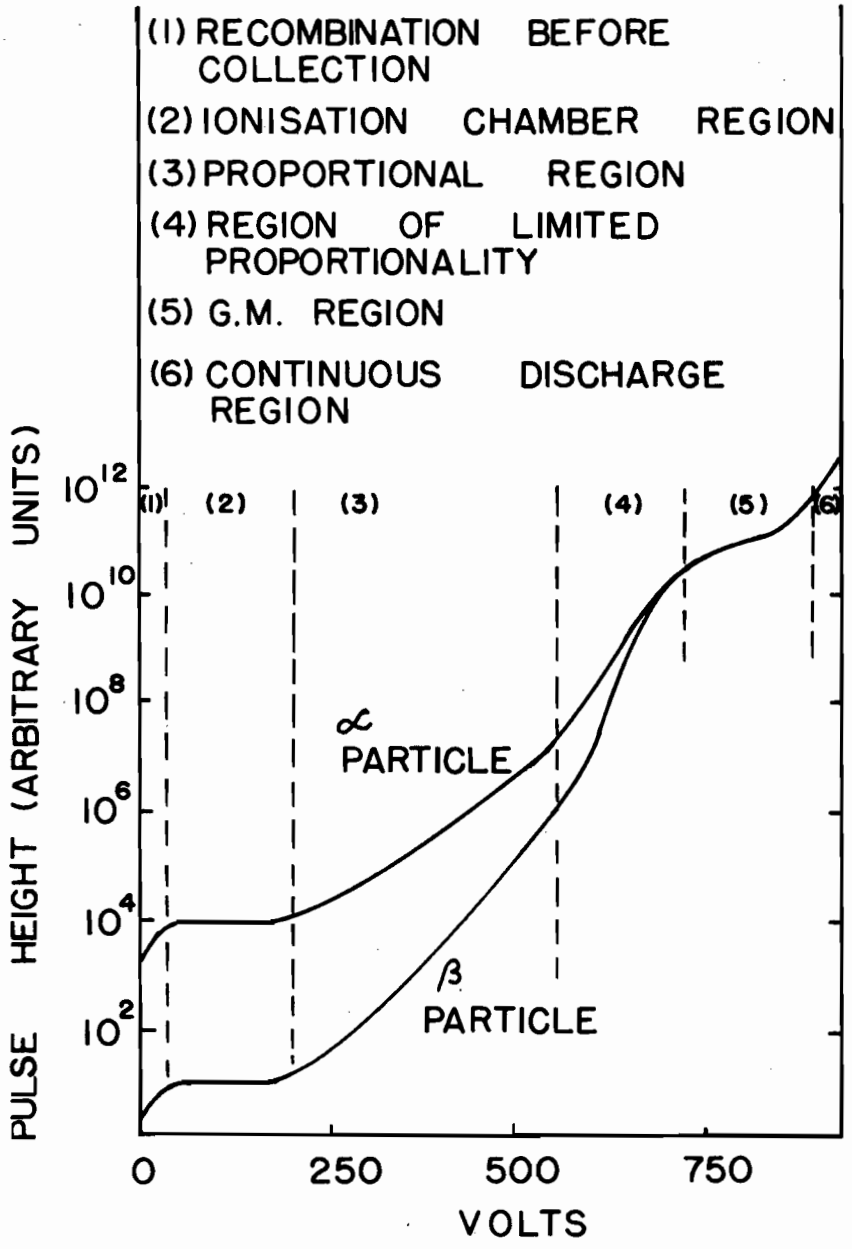
(1) RECOMBINATION BEFORE COLLECTION
(2) IONISATION CHAMBER REGION
(3) PROPORTIONAL REGION
(4) REGION OF LIMITED PROPORTIONALITY
(5) G.M. REGION
(6) CONTINUOUS DISCHARGE REGION
PULSE HEIGHT (ARBITRARY UNITS)
10^{12}
10^{10}
10^{8}
10^{6}
10^{4}
10^{2}
(1)
(2)
(3)
(4)
(5)
(6)
α PARTICLE
β PARTICLE
0
250
500
750
VOLTS

velocity of the ions increases and losses due to recombination are practically negligible as shown in region II. This region is referred to as the 'saturated ion chamber region'. If the field is increased, the ionization current is increased by a constant factor through the phenomena of gas multiplication. The primary electrons are sufficiently accelerated to produce additional ionization. This is shown in region III, which is known as the proportional counting region. In the proportional counters, gas multiplication factors as high as 10^5 or 10^6 are sometimes employed.

Proportional counters are often used in conjunction with pulse height analysers, since gain in pulse size can be achieved while dependence of the pulse size on the primary ionization is preserved. This very fact makes it also possible to discriminate the type and intensity of the radiation causing primary ionization.

In region IV, as shown in Fig. 2, the pulse height at a given voltage is independent of the initial ionizing conditions. As a matter of fact gas multiplication increases the charge to a value that is limited by the characteristics of the chamber geometry and external circuit. This region is referred to as the G-M (Geiger-Muller) region.

A gas-filled tube, operating under the conditions of region IV, is known as a G-M tube. These types of counter are very widely used for measuring negative and positive electron emission. Since the pulses in the G-M

counter are independent of the primary events, these counters cannot be used with pulse height analysers to distinguish the energy as well as the type of ionizing radiation.

1.4.2 Scintillation counters

Whenever ionizing radiation passes through certain inorganic or organic crystals, such as sodium iodide or anthracene, scintillations are emitted. If the material is transparent to its own fluorescence, these scintillations could be picked up by some suitable device like a photo-multiplier tube (PMT) and amplified. The resulting pulses from the PMT, which are electrical in nature, indicate the passage of ionizing radiation through the phosphors. These electrical pulses could be made proportional to the energy loss of the primary radiation in the phosphors and thus, as in the case of proportional counters, in addition to measuring the disintegration rate, the entire energy spectrum of ionizing radiation could be studied.

The inorganic crystals have, in general, higher density than organic crystals and thus higher stopping power and greater efficiency for gamma rays. Quite a few text-books[30,33,34] exist on the subject of scintillation counting.

The properties of ionization chambers, proportional counters, G-M counters, and scintillation counters have been summarized[35] in Table I.

Table I

COMPARATIVE STUDY OF DETECTION SYSTEMS[35]

Detector	Sensitive medium	Detector multiplication	Output signal volts	Resolving times seconds	Efficiency			Electronic gain required
					Beta	X	γ	
Ionization Chamber	Gas	1	10^{-6} to 10^{-3}	10^{-6} to 10^{-3}	low	low	low	very high
Proportional Counter	Gas	10^{2} to 10^{4}	10^{-4} to 10	10^{-6}	high	med.	low	high
Geiger Counter	Gas	10^{7}	0.1 to 10.0	10^{-4} to 10^{-3}	high	med.	low	low
Scintillator Photomultiplier	Solid or liquid	10^{6}	10^{-2} to 10.0	10^{-9} to 10^{-6}	med.	high	very high	med.

med. = medium

1.4.3 Brief review of detection of emanation and radioactive inert gases

(a) Radon type activities:

In the earliest experiments, the emanations of Ra^{226} (1617 y.) and Th^{228} (1.91 y.) were used. The devices varied with the nature of the experiments. In one of the earliest techniques, Hahn[13] used a gamma electroscope which was nothing but a very crude form of ionization chamber.

Hahn[19] published an excellent review in which the methods of preparing sources for emanation and the methods of detecting gamma and beta activities are described.

Other methods of measuring radon and thoron activities have been described[36,37,38,39,40,41] which vary from the torsion balance to a suitable counter. Some of these methods are dealt with in detail in a review by Zimens[25].

A scintillation detection device[42] has recently been reported for the assay of radon gas.

(b) Xenon type activities:

Since xenon and krypton occur in fission products, quite a few direct and indirect methods for their detection and measurement have been reported. A monogram by Momyer[43] includes most of the methods.

One of the earliest methods was filling a suitable chamber with the gases and then measuring the activity in a Geiger or proportional counter[44,45]. The detailed study and problems faced in these methods are given[46] by various workers.

For high specific activity and quantitative work, gas-filled proportional counter tubes were suggested by Bernstein and Ballentine[47]. These tubes are commercially available.

Another method for deposition of rare gases on the cathode in a glow discharge tube was suggested by Hyde and Momyer[48]. This was successfully used by Mathur and Hyde[49] and Moore[50]. The activity of the gases collected this way was directly measured and analysed on a scintillation spectrometer.

An indirect method consisted in collecting the daughter product of the rare gases produced in fission on a negatively charged wire coaxial with the moving gas stream[51,52]. This method, however, is not very efficient, but a good approximation of the half-lives could be obtained from the flow rates and daughter activity as a function of distance along the wire.

2. EXPERIMENTAL

2. 1 PRODUCTION OF RADIO-IODINE

2.1.1 Selection of a suitable Iodine Isotope

A careful study of the Chart of the Nuclides[53] shows that there are no isotopes of iodine in the neutron-excess region which have half-lives of such a value that secular equilibrium is established in the decay to xenon. $I^{128-132}$, I^{134}, and I^{136} all decay to stable xenon. $I^{137-139}$ are very short-lived (24 sec to 2.7 sec). Most of the neutron-deficient isotopes of iodine decay to stable tellurium which made work in this region out of the question, even though production of these isotopes would be a simple matter. Then it was left to select from

$$I^{133} \xrightarrow[21\ hr.]{\beta^-} Xe^{133} \xrightarrow[5.3\ d.]{\beta^-}$$

and

$$I^{135} \xrightarrow[6.7\ hr.]{\beta^-} Xe^{135} \xrightarrow[9.2\ hr.]{\beta^-}$$

The selection was made in the neutron-excess region of the iodine isotopes. I^{135} was chosen for the following

reasons:

(1) The half-life of I^{135} is fairly long (6.7 h.), thus providing enough time to prepare it and the samples under investigation.

(2) The half-life of the daughter, Xe^{135}, is again long (9.2 h.). Consequently, during the period of observation in the phase-change studies, which is usually 20 - 30 minutes, there would not be any appreciable decay of Xe^{135}.

(3) Examination of the decay scheme[54] reveals that the gamma rays of Xe^{135} are very well separated even from the parent I^{135}, as shown in Fig. 3.

(4) The fission yield of I^{135} is quite high both in thermal-neutron and proton-induced fission as shown in Fig. 4 [55] and Fig. 5 [56] respectively.

To detect Xe^{135} emanating from I^{135}, the 250 kev gamma ray was used as a basic standard throughout this work because the branching ratio for the 250 kev gamma ray is 97%, and thus the relative photon intensity is quite high. This fact is evident from Fig. 3.

2.1.2 Target material, preparation and bombardment

I^{135} was produced by the proton-induced fission of uranium in the circulating beam of the McGill Synchrocyclotron. Uranium oxide, U_3O_8, of naturally-occurring isotopic abundance, was the target material and was obtained from Atomic Energy of

Figure 3

SHOWING THE DECAY SCHEME

$$I^{135} \longrightarrow Xe^{135} \longrightarrow Cs^{135} \longrightarrow Ba^{135}$$

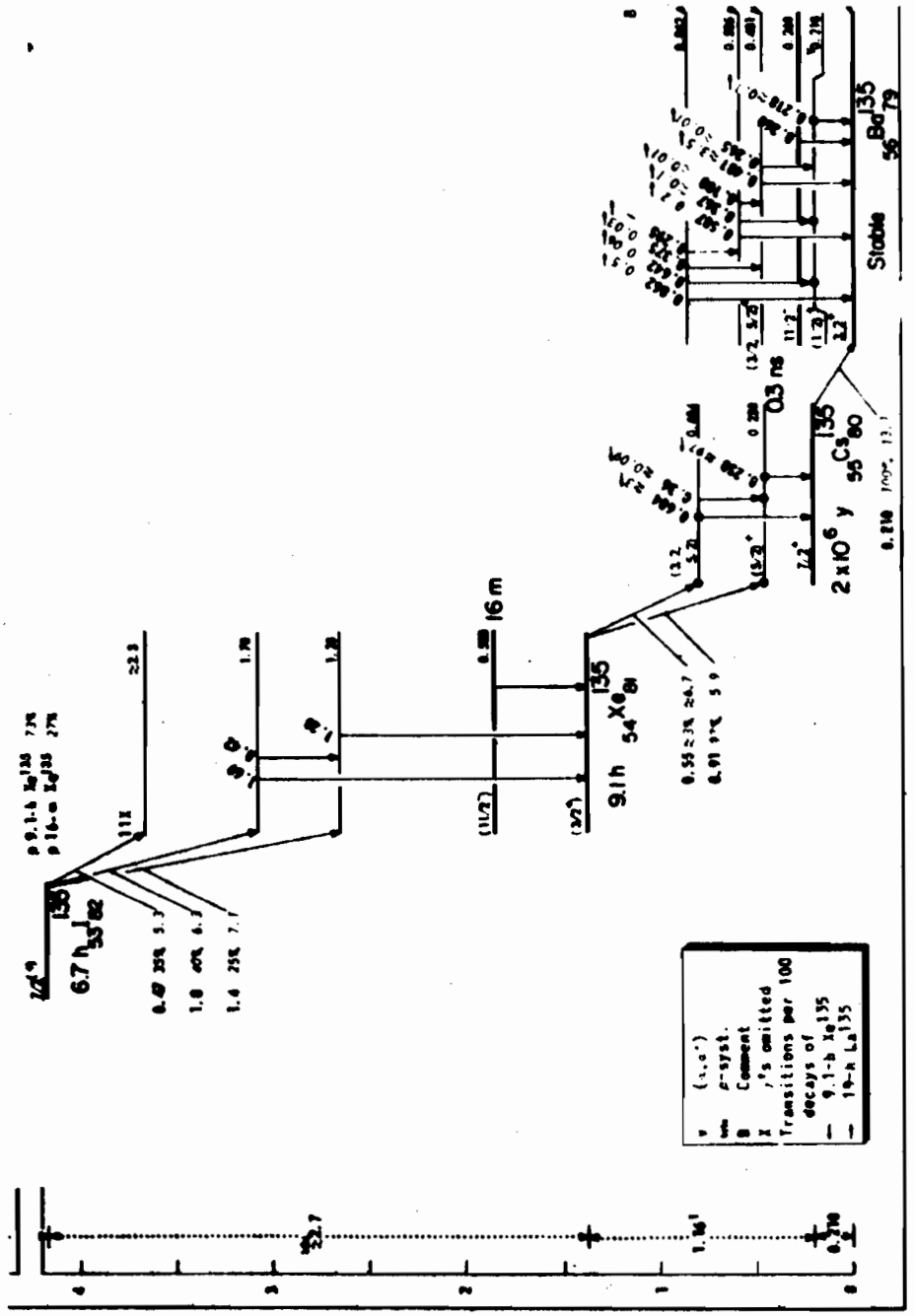
6.7 h
9.1 h
16 m
0.3 ns
2x10^6 y
Stable
Ba 56 79
Cs 55 80
Xe 54 81
Transitions per 100 decays of
9.1-h Xe135
16-h La135

Figure 4

FISSION YIELD CURVE FOR U^{235}, U^{233}, AND Pu^{239}

(Reproduced from A.M. Weinberg and E.P. Wigner: 'Theory of Neutron Chain Reactors', p. 110, reference 55)

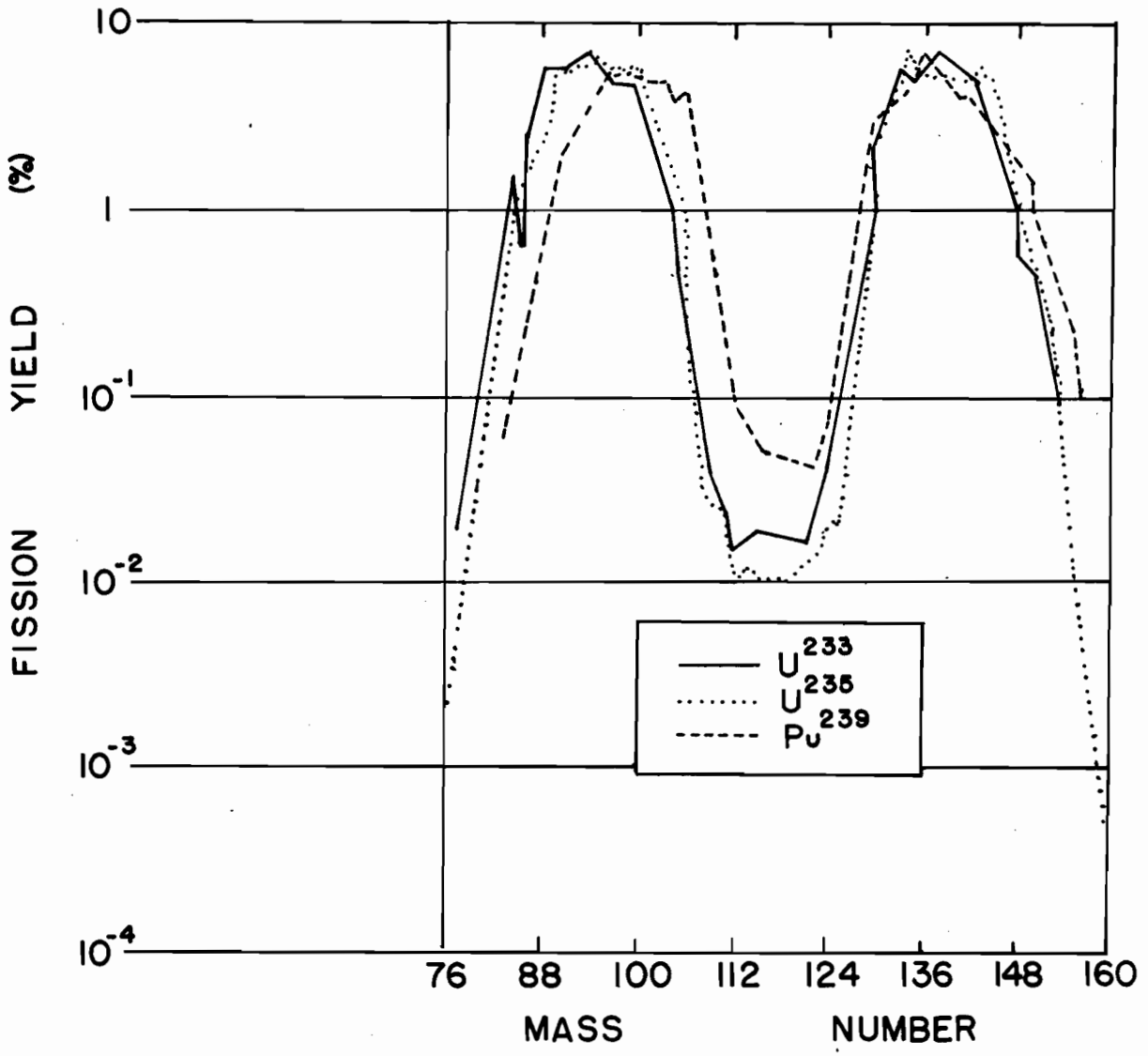
10
1
10^{-1}
10^{-2}
10^{-3}
10^{-4}
FISSION YIELD (%)
76
88
100
112
124
136
148
160
MASS NUMBER
U^{233}
U^{235}
Pu^{239}

Figure 5

FISSION-YIELD CURVE OF PROTON-INDUCED FISSION OF U^{238} AS OBTAINED FROM REFERENCE 56

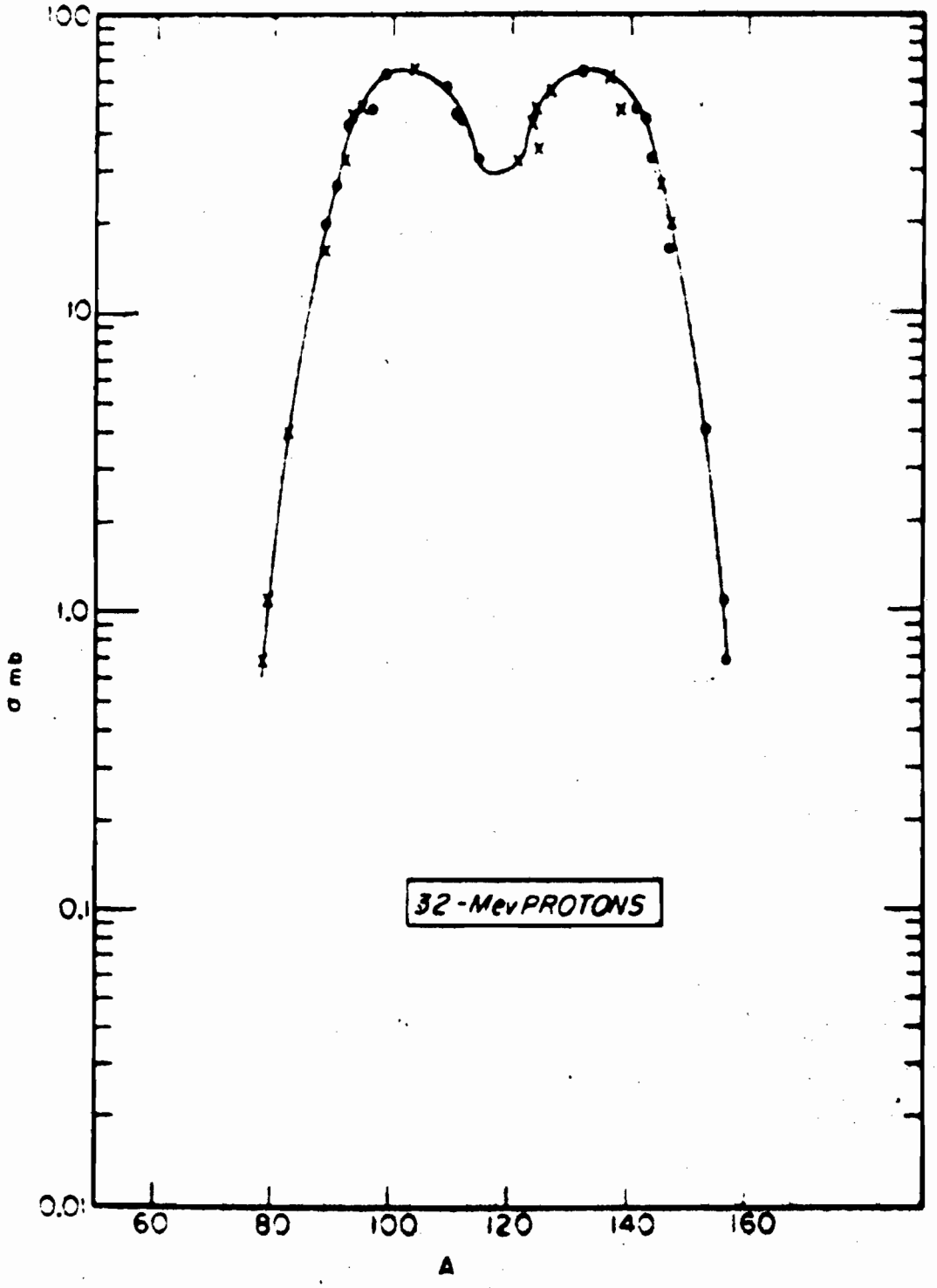

(b)

Canada Limited, in the form of fine powder.

The bombardments were performed at low energies. Since these bombardments were designed only to produce fission, it was not considered necessary to have a very accurate knowledge of proton-beam intensities as well as energies, and hence no internal monitor was used.

About 20 - 25 mgs of natural uranium oxide were packed into thin, uniform pure aluminum tubing with a wall thickness of 0.0015". Both ends of the tube were sealed mechanically and mounted on a target holder as shown in Fig. 6. The target was bombarded in the energy range of 20 - 23 Mev. Kirkaldy's curve[57] of proton energy versus radius of the beam, as illustrated in Fig. 7, was used. This curve was also corrected[58] for radial oscillations of the beam. Each bombardment lasted for a period of about 30 minutes.

The target was allowed to cool for about twelve hours before any chemical separation was performed, thus permitting the decay of the short-lived activities of the iodine.

2.1.3 Target chemistry

Following the irradiation, the aluminum tube was cut open and the powder transferred to a 50 ml centrifuge tube and dissolved in concentrated HNO_3 in a cold bath to avoid losses of iodine. After the powder was dissolved, 10 mgs of I^- carrier were added and iodine was separated by

Figure 6

TARGET HOLDER ASSEMBLY

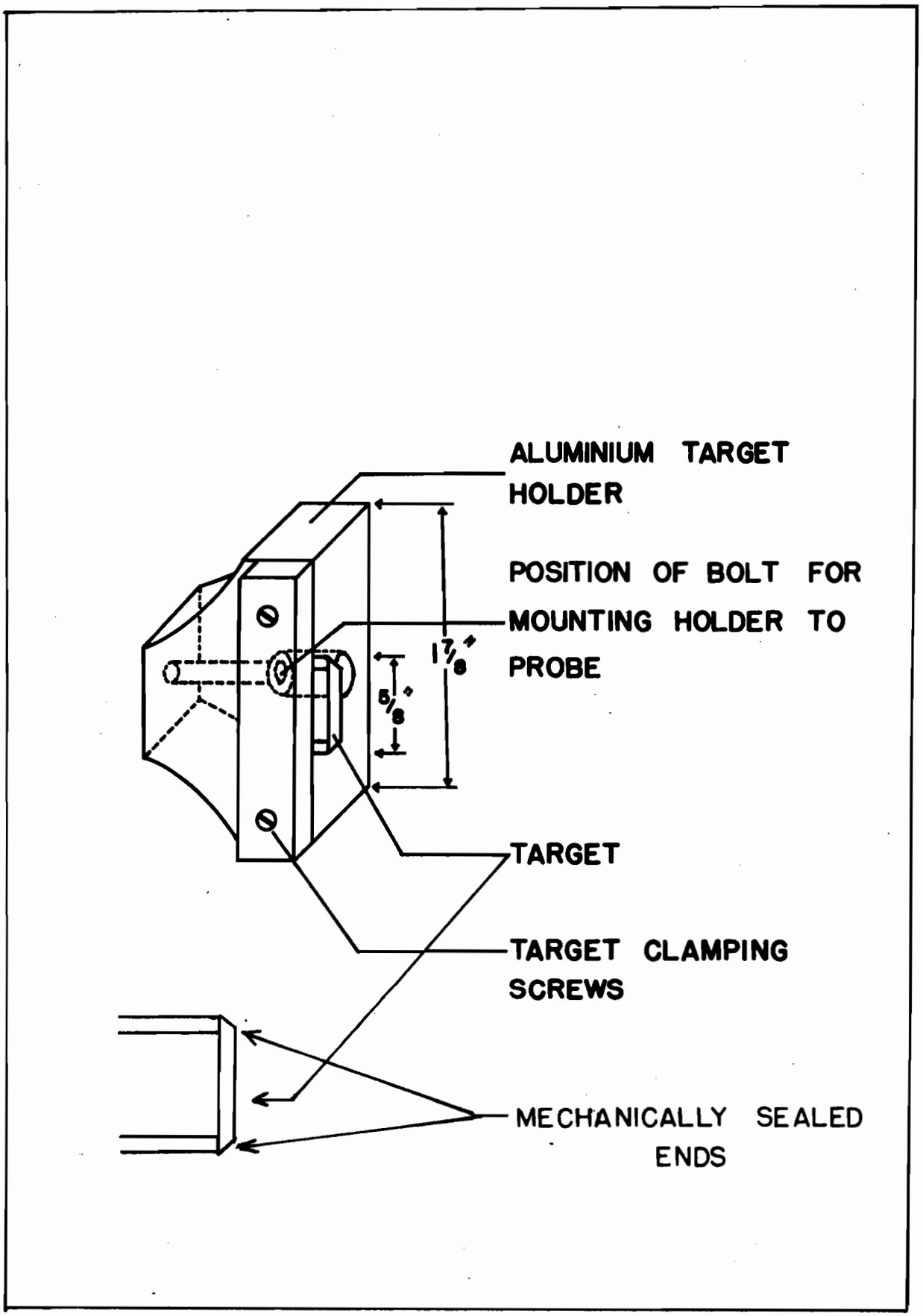
ALUMINIUM TARGET HOLDER
POSITION OF BOLT FOR MOUNTING HOLDER TO PROBE
1 7/8"
5/8"
TARGET
TARGET CLAMPING SCREWS
MECHANICALLY SEALED ENDS

Figure 7

PROTON BEAM ENERGY VERSUS PROBE DISTANCE

OF THE McGILL SYNCHROCYCLOTRON

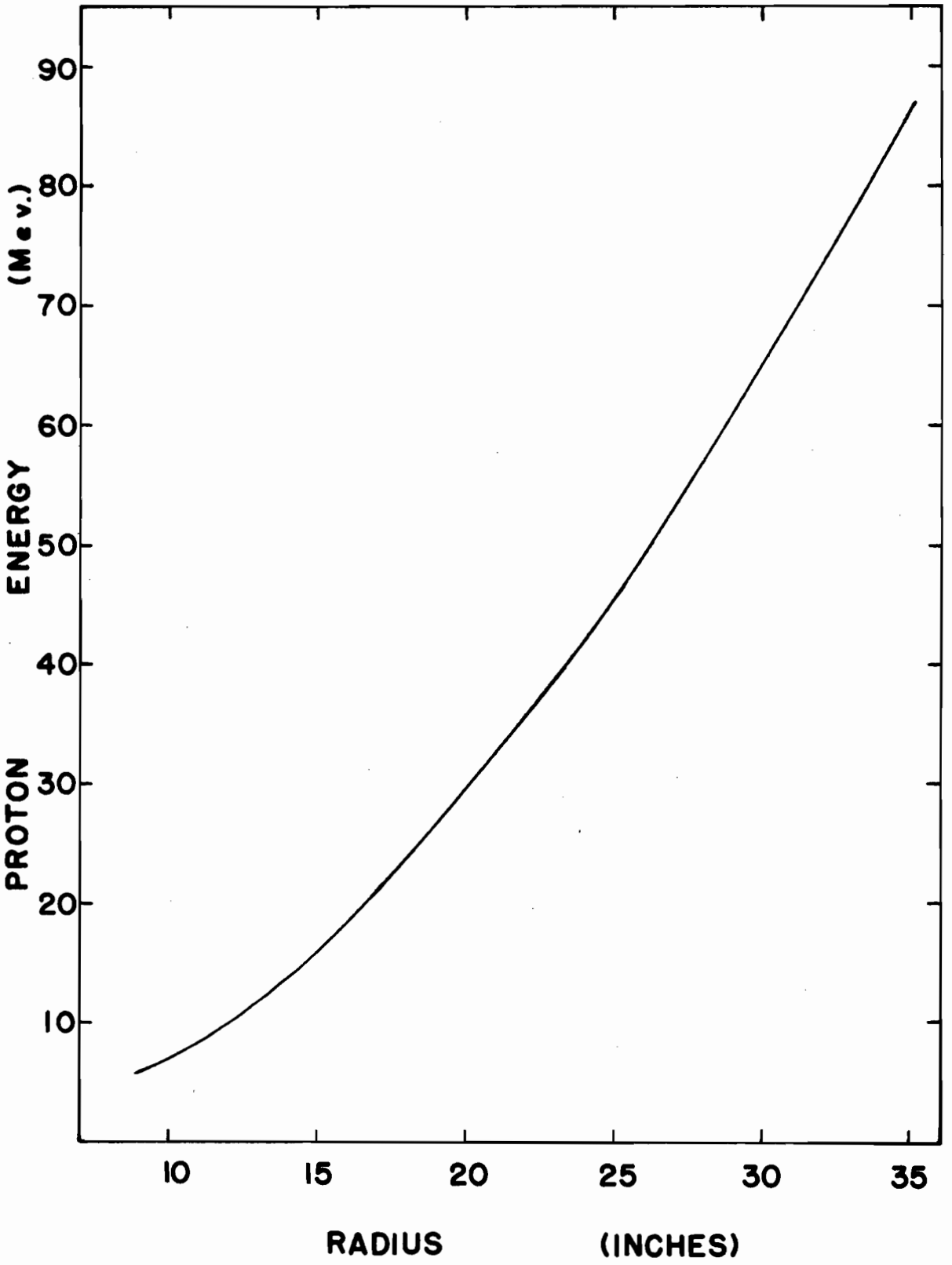
PROTON ENERGY (Mev.)
90
80
70
60
50
40
30
20
10
10
15
20
25
30
35
RADIUS (INCHES)

solvent extraction using CCl_4, after various oxidation and reduction cycles according to the method described by Glendenin and Metcalf[59] (Appendix I).

2.2 PREPARATION OF THE SAMPLES

2.2.1 General treatment

The purified iodine in the form of iodide was mixed with 20 ml of 0.1 M KI solution. The mixing was carried on for 30 minutes by mechanical means to ensure a uniform distribution of active and inactive iodine.

The iodides of Pb(II), Cu(I), Ag, Hg(II), and Tl(I) were precipitated from this mixture by classical methods using the following reactions:

$$Ag^+ + KI \longrightarrow AgI\downarrow + K^+$$

$$Pb^{++} + 2KI \longrightarrow PbI_2\downarrow + 2K^+$$

$$Tl^+ + KI \longrightarrow TlI\downarrow + K^+$$

$$Hg^{++} + 2KI \longrightarrow HgI_2\downarrow + 2K^+$$

$$Cu^+ + KI \longrightarrow CuI\downarrow + K^+$$

During the precipitation minimum volumes were used to get maximum specific activity in the samples. The iodides have low solubilities in water, as shown in Table II.

The iodide precipitates were subsequently transferred directly to the experimental sample holder which

Table II

SOLUBILITIES OF HALIDES OF THE METALS UNDER STUDY, IN AQUEOUS MEDIUM[60]

Compound	Solubility in water gm/100 ml
AgI	3×10^{-7} (20°C)
PbI_2	0.063 (20°C)
TlI	0.0064 (20°C)
CuI	0.0008 (18°C)
HgI_2	0.0061 (25°C)

Figures in parenthesis show the temperature of observation

was a sintered porcelain micro-crucible specially designed for this work. The dimensions of a typical crucible are shown in Fig. 9 (p. 34).

The precipitates were washed with 95% alcohol followed by ether. Finally, all the crucibles containing experimental samples were left for about 6 - 7 hours in a vacuum desiccator containing silica gel.

2.2.2 Identification of the experimental samples

Since the radiochemical procedures of preparing the samples were entirely based on classical chemical methods, it

was presumed that samples prepared are chemically pure. However, in one case, e.g. that of TlI, the structure was examined by the powder X-ray diffraction technique* by comparing the 'd' values with those described in the literature, since X-ray photographs are characteristic.

In the present study inactive thallous iodide was prepared radiochemically and the powder sample exposed for 8 hours to CuKα X-rays at 32 kv, 16 ma. The X-ray photograph thus obtained is shown in Fig. 8. The 'd' values are shown and compared in Table III[61,62,63]. It is clear from the table that results in the present work are in close agreement with those obtained by previous workers.

2.3 HEATING SYSTEM TEMPERATURE CONTROL AND MEASUREMENT

2.3.1 Heating system

The porcelain sintered crucible containing the experimental sample was heated in a specially designed furnace as shown in Fig. 9. Since the thermal behaviours of the proposed iodides were studied in the range 15°C to 200°C, the furnace could be made from pyrex glass. The heating coil was insulated with a 1 cm thick layer of plaster of paris and asbestos mixture to cut down temperature fluctuations.

---

*The author is very grateful to Professor A.J. Frueh of the Department of Geology, McGill University, for his kind assistance in the X-ray work.

Figure 8

DEBYE-SCHERRER X-RAY POWDER PATTERNS FOR TlI

Table III

'd' VALUES FOR THALLOUS IODIDE AT VARIOUS INTENSITIES[61,62,63]

S.N.	Relative intensity	1926	1953	Present work
1	14	-	-	4.2502
2	13	-	-	4.022
3	100	3.359	3.332	3.133
4	65	3.15	3.228	3.2549
5	1	-	2.749	2.7385
6	90	2.719	2.692	2.6749
7	40	2.647	2.624	2.6106
8	23	2.077	2.291	2.2813
9	22	2.264	2.248	2.2378
10	29	2.077	2.069	2.0623
11	45	2.051	2.036	2.0295
12	30	1.876	1.869	1.8625
13	4	-	1.7602	1.7549
14	20	1.718	1.7259	1.7202
15	2	1.690	1.7083	1.7053
16	60	-	1.6148	1.6195
17	3	-	1.5431	1.5395
18	55	1.527	1.5285	1.5189
19	8	1.463	1.5474	1.4557
20	5	1.431	1.4341	1.4347
21	15	-	-	1.3742

Figure 9

HEATING ARRANGEMENT

and

DIMENSIONS OF THE CRUCIBLE

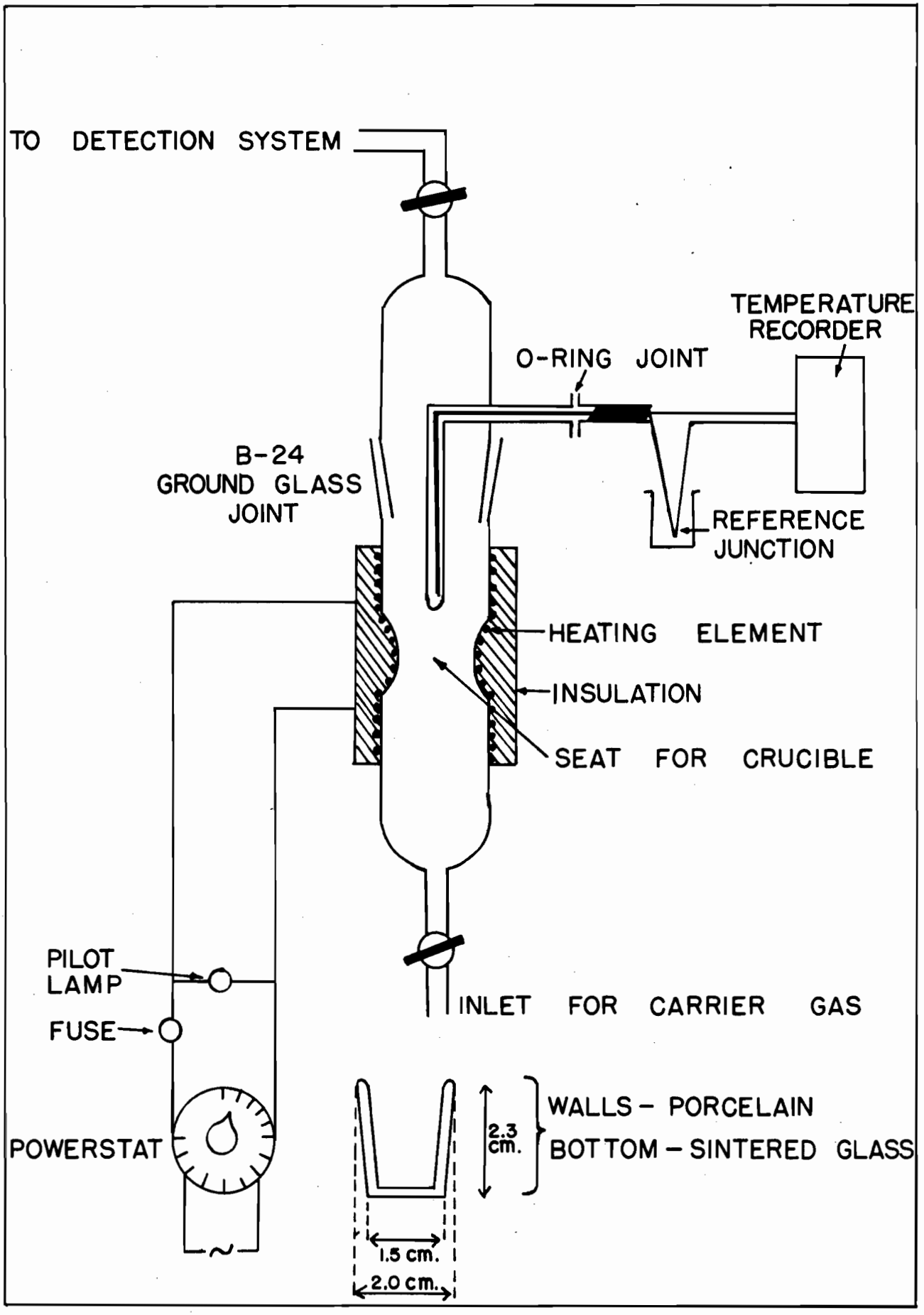
TO DETECTION SYSTEM
TEMPERATURE RECORDER
O-RING JOINT
B-24 GROUND GLASS JOINT
REFERENCE JUNCTION
HEATING ELEMENT
INSULATION
SEAT FOR CRUCIBLE
PILOT LAMP
FUSE
INLET FOR CARRIER GAS
POWERSTAT
2.3 cm.
WALLS - PORCELAIN
BOTTOM - SINTERED GLASS
1.5 cm.
2.0 cm.

2.3.2 Temperature control and measurement

The power was controlled and drawn through a commercially built, precision variable transformer. In the present work a Superior Elective type 20-2 Powerstat was used. It was calibrated in such a way that one arbitrary scale would raise the temperature 10°C per minute.

A copper-constantan thermocouple was employed to measure the temperature. The potential difference was recorded on a Leeds and Northrup Speedomax type G recorder. The reference junction was kept at melting-ice temperature. Standard conversion tables[64] for the thermocouples were used.

The systems for heating, temperature control, and temperature measurements are shown in Fig. 9.

2.4 RADIOACTIVITY MEASUREMENTS

Various techniques were used to measure the activity of radioactive xenon in this work.

2.4.1 $4\pi\beta^-$-Counting

Initially, the indirect method of Pate, Foster and Yaffe[65] by $4\pi\beta^-$-counting was employed. A very thick source of iodine in the form of AgI was mounted on a thin uniform film of VYNS[66] (a polyvinylchloride acetate copolymer). The source was measured by a $4\pi\beta^-$-counter[67-70] and then left for two hours to allow the xenon to grow. Subsequently it was heated under an infra-red lamp for

30 minutes and measured again. After making the necessary correction for the decay of iodine activity, it was found that there is a loss of 10 - 40% in activity, depending upon the specific activity and thickness of the source. This loss was due to the expulsion of xenon on heating. The results obtained in this work were in accordance with those of Kjelberg and Taniguchi[71] in similar experiments in this Laboratory.

This method was not suitable for the proposed work due to the following reasons:

(a) VYNS films cannot stand high temperatures.

(b) Heating inside the counter was itself a problem if VYNS is somehow replaced by metallic film.

However, this method indicates that the $I^{135} \longrightarrow Xe^{135}$ system could be employed in the study of solid state changes.

2.4.2 Scintillation counting (discontinuous method)

Kelly[72] has described a method for measuring inert gas activities by gamma-ray scintillation counting to determine the attachment of inert gases to powders following (n, γ) reaction.

In the present work the Xe^{135} emanating from the heated source in the furnace was swept by carrier gas helium at various ascending steps of temperature. A minimum amount of carrier gas was used. The helium along with Xe^{135} was

collected in an evacuated trap containing active charcoal kept at liquid-air temperature. The ACC type charcoal supplied by Union Carbide was used. Since xenon is adsorbed effectively on the charcoal[73,74,75], it was presumed that almost all of the xenon was trapped on the charcoal bed. It is also obvious that, if some xenon is left unadsorbed, it will solidify at this temperature ($\sim$ -190°C) since the freezing point of xenon is -111.6°C. This fact was utilized to separate xenon from the spallation products of iodine in the study of the problem described in Part II of this thesis.

A sodium iodide crystal of dimension 1½" diameter x 1" thick mounted on a Dumont type 6292 photomultiplier tube (Harshaw thallium activated sodium iodide integral line) was kept underneath the trap. In this work the S-12 type assembly was used. The output of the photomultiplier tube was fed to a preamplifier and subsequently to Atomic International model 204B, non-overloading linear amplifier. The output signal from the amplifier was fed to the previously calibrated, Baird Atomic model 510, single channel pulse height analyser (SCPHA). The calibration curve of the SCPHA is shown in Fig. 10. The window of the SCPHA was adjusted for the 250-kev gamma ray of Xe^{135}. The output of the SCPHA was fed to the scaler. The block diagram of the electronic system is illustrated in Fig. 11. The charcoal trap was shielded by a 1½" thick lead wall. This trap, the position of the NaI(Tl) crystal and shielding are shown in Fig. 12.

Figure 10

CALIBRATION CURVE FOR THE

SINGLE CHANNEL PULSE HEIGHT ANALYSER

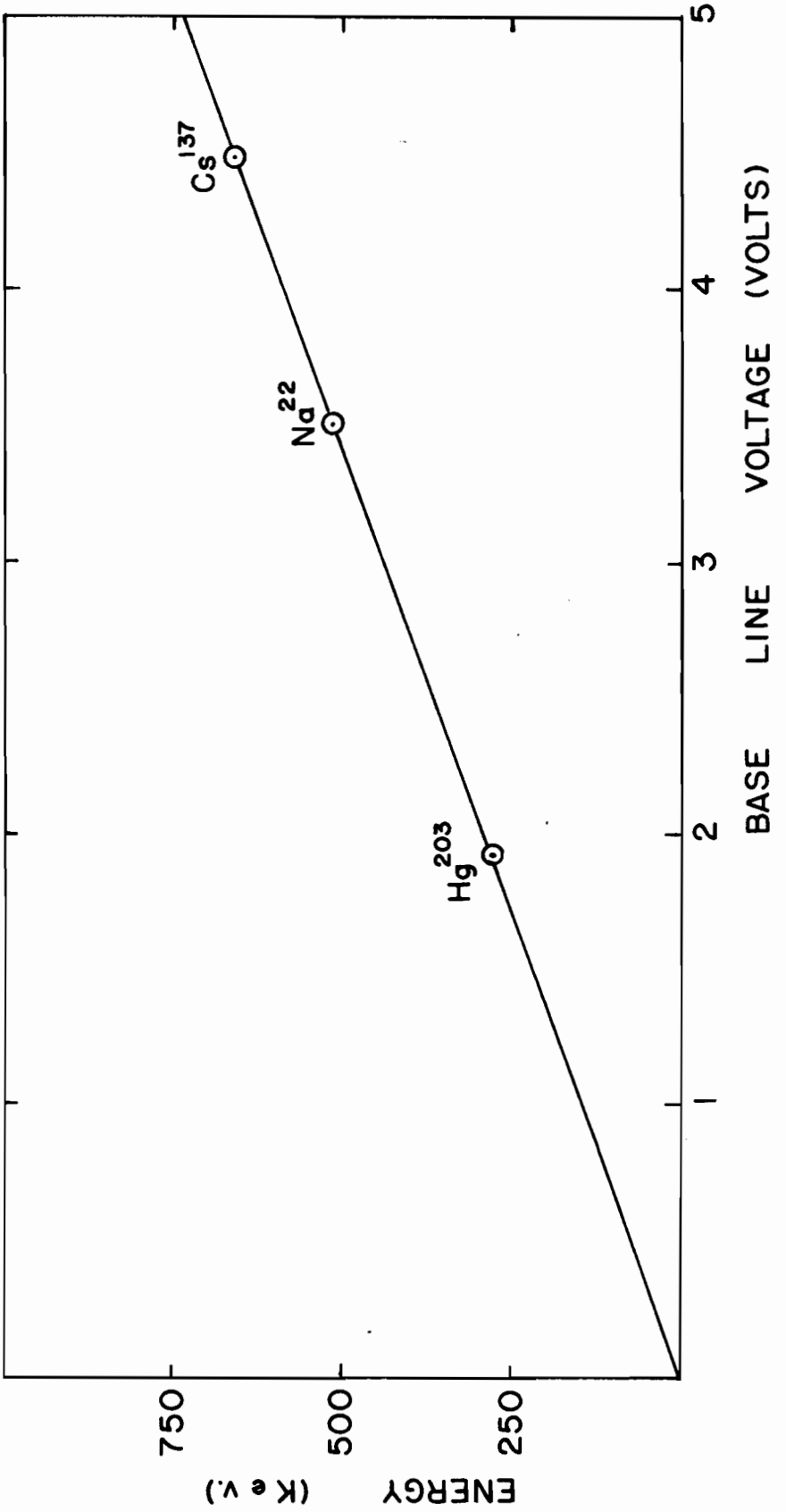
ENERGY (K e v.)
750
500
250
BASE LINE VOLTAGE (VOLTS)
1
2
3
4
5
Cs137
Na22
Hg203

Figure 11

BLOCK DIAGRAM OF ELECTRONIC ARRANGEMENT

FOR THE MEASUREMENT OF Xe^{135} ACTIVITY

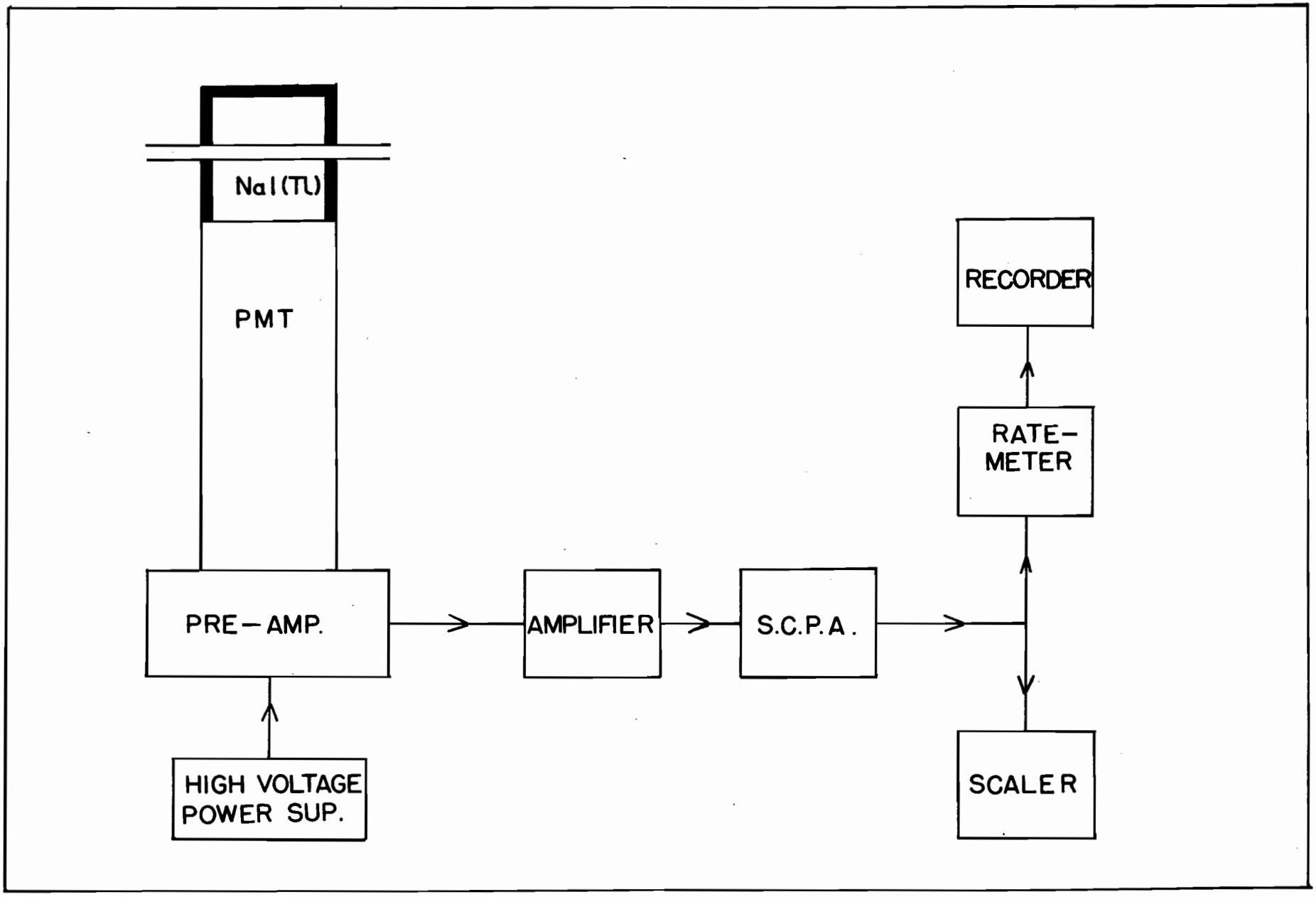
NaI(Tl)
PMT
PRE-AMP.
AMPLIFIER
S.C.P.A.
RECORDER
RATE-METER
SCALER
HIGH VOLTAGE POWER SUP.

Figure 12

ARRANGEMENT FOR COLLECTING XENON

IN THE DISCONTINUOUS METHOD

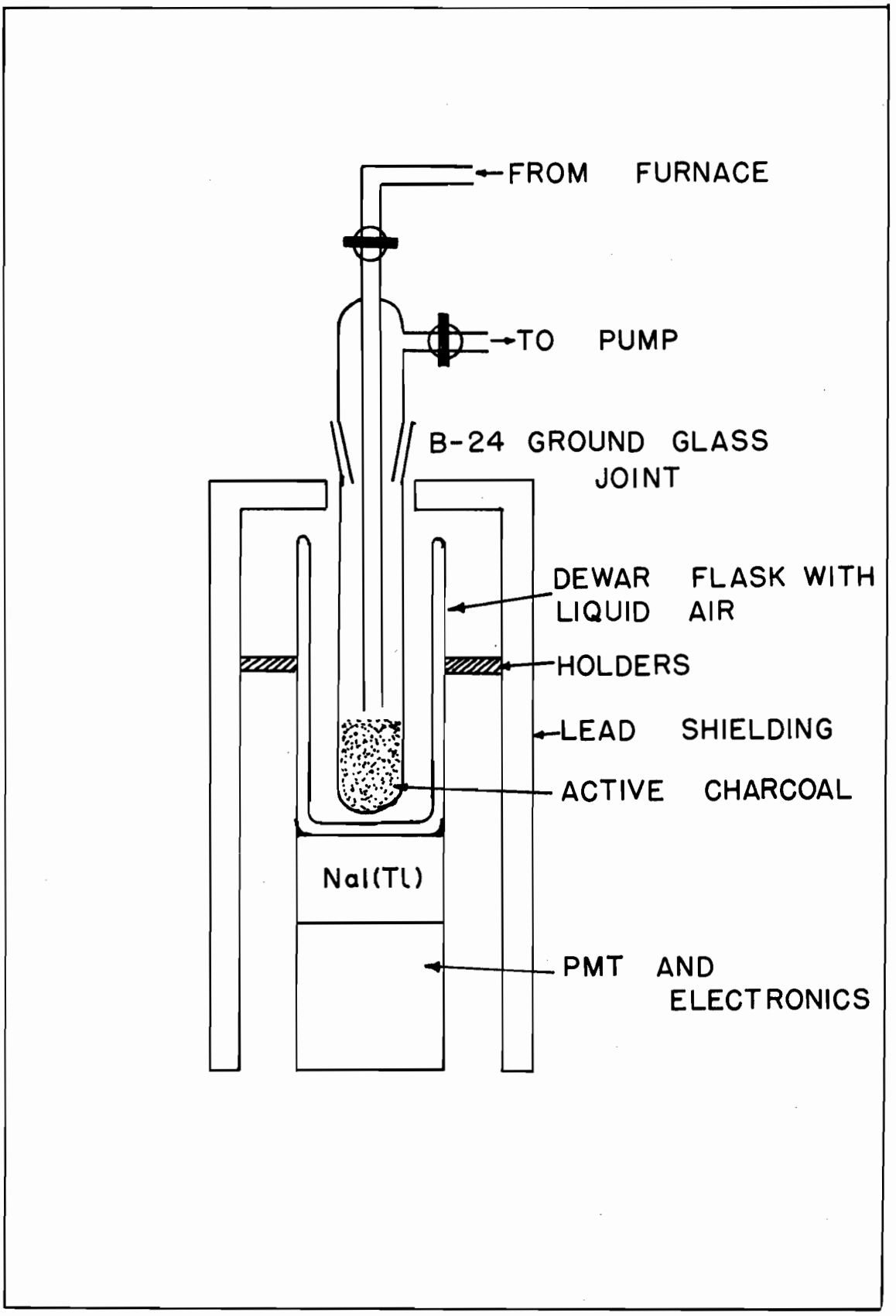
FROM FURNACE
TO PUMP
B-24 GROUND GLASS JOINT
DEWAR FLASK WITH LIQUID AIR
HOLDERS
LEAD SHIELDING
ACTIVE CHARCOAL
NaI(Tl)
PMT AND ELECTRONICS

The temperature was raised in steps of 3 - 4°C and xenon was collected and measured in the trap. At every temperature of observation the helium was pumped out to provide room for fresh helium containing xenon. AgI was studied by this method, and the results are discussed in the following chapter.

Since the phase transitions in most of the compounds occur within a very narrow temperature range, the method of Kelly[72] was not feasible for the present work. It was difficult to increase the temperature in steps of 1°C, therefore a flow or continuous system was devised.

2.4.3 Flow or continuous scintillation method

A hemispherical chamber, as shown in Fig. 13, with a very thin bottom was designed. The diameter of the base of this hemispherical chamber was equal to the diameter of the NaI(Tl) crystal. There was no change made in the electronic system except that an AEP-1902-A type counting rate meter coupled with a recorder was connected to the output stage of the SCPHA. The time constant[76] of the rate meter was kept at 14 seconds.

Thallous iodide has a known phase transition at 168°C. This was studied in this set-up, and a sample of the result obtained is shown in Fig. 14. From this figure it is clear that whenever there is a phase transition, a sharp peak in xenon activity occurs.

Figure 13

FLOW CHAMBER DETECTION SYSTEM

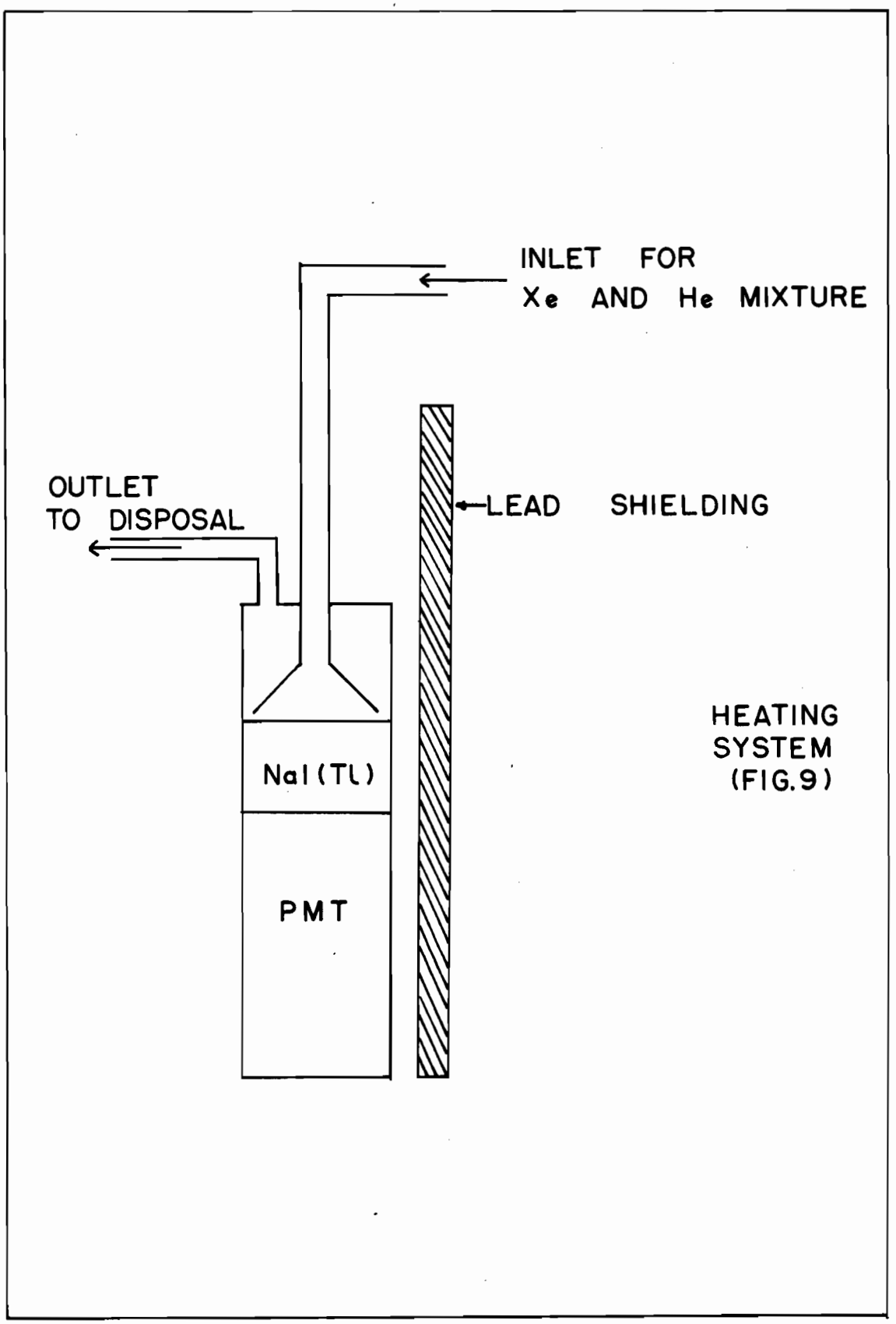
INLET FOR
Xe AND He MIXTURE
OUTLET
TO DISPOSAL
LEAD SHIELDING
HEATING
SYSTEM
(FIG.9)
NaI(Tl)
PMT

Figure 14

THALLOUS IODIDE PHASE-TRANSITION CURVE

SHOWING THE SHARP PEAK WHENEVER A

PHASE-TRANSITION OCCURS

IN U.S.A. THE ESTERLINE-ANGUS CO., INC., INDIAN

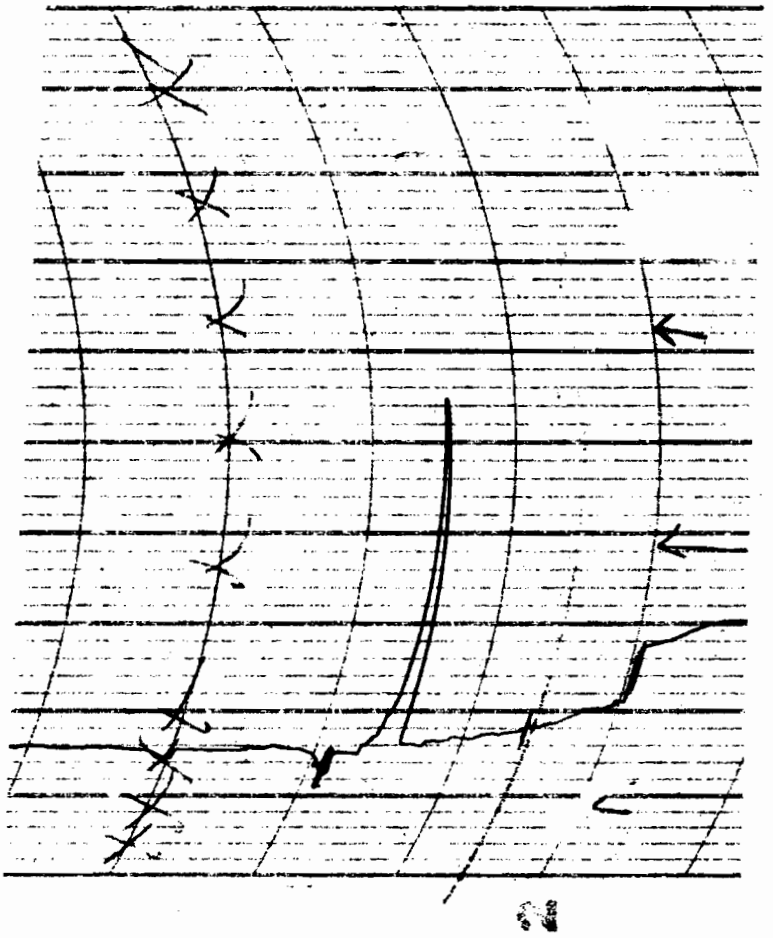

2.4.4. Improved flow scintillation method

Since the flow method gave encouraging results, this method was further improved.

The flow chamber and NaI(Tl) crystal were replaced by a single unit, i.e. NaI(Tl) Harshaw type AF crystal with through side hole. These crystals have a very high detection efficiency in the flow system for gamma rays. This type of assembly with technical details is shown in Fig. 15. To avoid the contamination of the hole, an auxiliary thin glass tube was introduced into the hole with ball and socket joints on either end. The crystal was mounted on a Dumont type 6292 photomultiplier tube, as described by Bell[77].

An additional improvement was effected by replacing helium with freon-12 (difluoro-dichloromethane) as carrier gas. Comparison of a few of the physical properties of freon-12, xenon, and helium are illustrated in Table IV[60,78,79].

The following arguments favour the selection of freon-12 against helium:

(1) The densities of freon-12 and xenon are quite close. Thus, according to Graham's Law of Diffusion, there will be a uniform inter-diffusion of these two, and hence more uniform mixing is expected. Consequently the statistical fluctuations in the count rate will be reduced, since xenon and freon will

Figure 15

CROSS SECTION OF THE NaI(Tl)

HARSHAW TYPE AF ASSEMBLY

CROSS SECTIONAL DIAGRAM THROUGH SIDE HOLE CRYSTAL ASSEMBLY

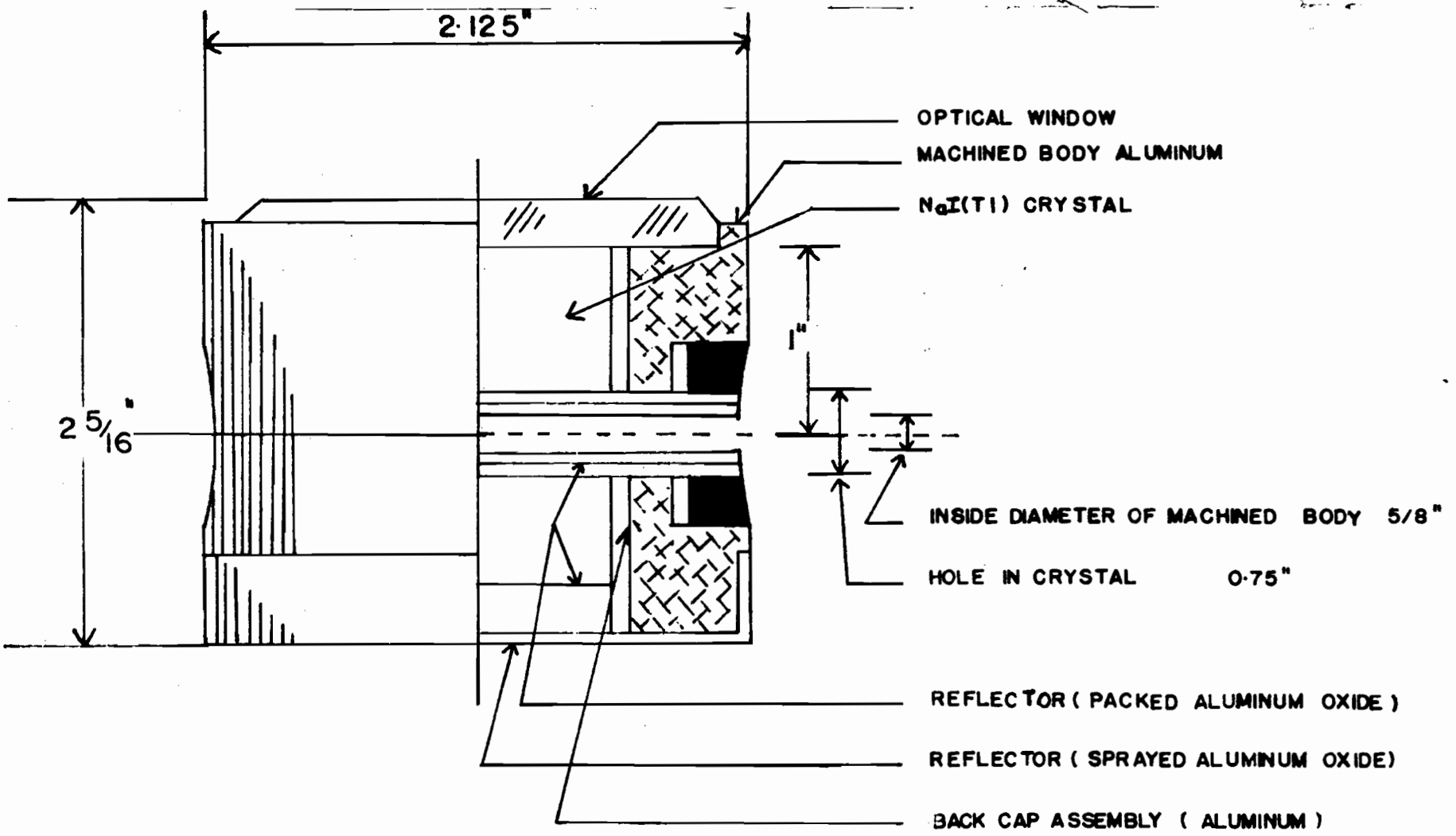

Table IV

PHYSICAL PROPERTIES OF XENON, FREON-12, AND HELIUM IN GASEOUS STATE AT ATMOSPHERIC PRESSURE[60,78,79]

Properties I	Xenon II	Freon-12 III	Helium IV
Mol. wt.	131.30	120.92	4.003
Density g/lit.	5.851 (0)	6.26 (23.7)	0.1785 (0)
Viscosity in centipoise	0.0231 (25)	0.0127 (30)	0.0198 (25)
Specific heat (cp)	4.968 (25)	17.533 (30)	4.968 (25)
Thermal conductivity	1.67×10^{-5} (100)	2.302×10^{-5} (30)	41.65×10^{-5} (100)

The figures in brackets in Columns II, III and IV represent temperatures in ^{o}C at which the observations were made.

arrive in the hole of the NaI(Tl) crystal almost at the same time.

(2) The viscosity of freon-12 is lower than that of helium.

(3) The thermal conductivity of freon-12 is very close to that of xenon.

Further improvement over the old apparatus was achieved by introducing a trap containing stainless steel balls kept at 0°C before the detection stage. This was necessary to hold back the iodine activity, since these halides have a finite vapour pressure at higher temperatures.

The count-rate recorder was changed to the same type as the temperature recorder, and both were synchronized.

The flow of the carrier gas was regulated by a flowmeter and a needle valve. The time taken by the carrier gas to reach the detection stage was about 3 to 4 seconds, which introduces an error in transition temperatures of $\pm$ 0.7°C. The entire assembly is shown in Figs. 9 and 11.

3. RESULTS AND DISCUSSION

3.1 CRYSTAL STRUCTURE CHANCE STUDIES

Preface:

The iodides of Ag, Tl(I), Cu(I), Hg(II), and Pb(II) labelled with I^{135} were heated. The Xe^{135} activity, resulting from the decay of I^{135}, was recorded as a function of temperature. In the case of AgI, both discontinuous and continuous methods of recording Xe^{135} activity were used. For the remaining iodides, only the continuous method was employed.

Any abrupt change in the Xe^{135} activity was found to be due to a change in crystal structure, as shown in Fig. 14, while a small change in Xe^{135} activity over an extended range of temperature could have been either due to diffusion of xenon or to some other surface mechanism.

Errors quoted in the case of HgI_2 and TlI are standard deviations, while those of the remainder are estimated.

3.1.1 AgI

(a) Discontinuous method:

In this experiment, the curve obtained for the first trial is shown in Fig. 16. We now subtract the Xe^{135} activity at any temperature of observation from that obtained at the immediately preceding temperature. When this procedure is performed over the entire range of temperatures under investigation and the results normalized for differences in temperature interval, we obtain a difference curve as shown in Fig.17. The

Figure 16

Xe^{135} ACTIVITY VERSUS TEMPERATURE RECORDING FOR AgI BY DISCONTINUOUS METHOD

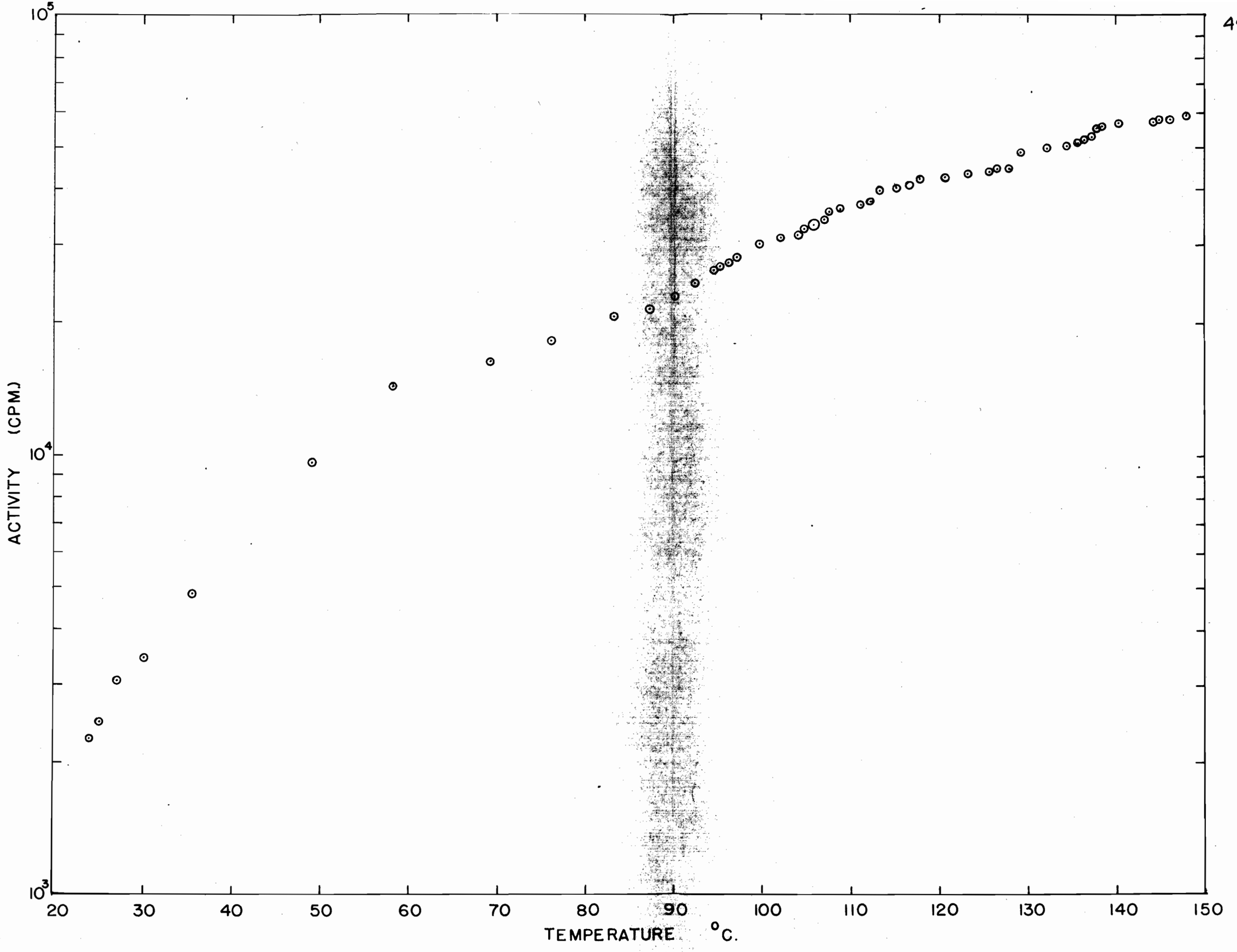
ACTIVITY (CPM.)
10^5
10^4
10^3
20
30
40
50
60
70
80
90
100
110
120
130
140
150
TEMPERATURE °C.

Figure 17

DIFFERENTIATED FORM OF THE CURVE (FIG. 16) AS OBTAINED BY DISCONTINUOUS METHOD FOR AgI

50(a)

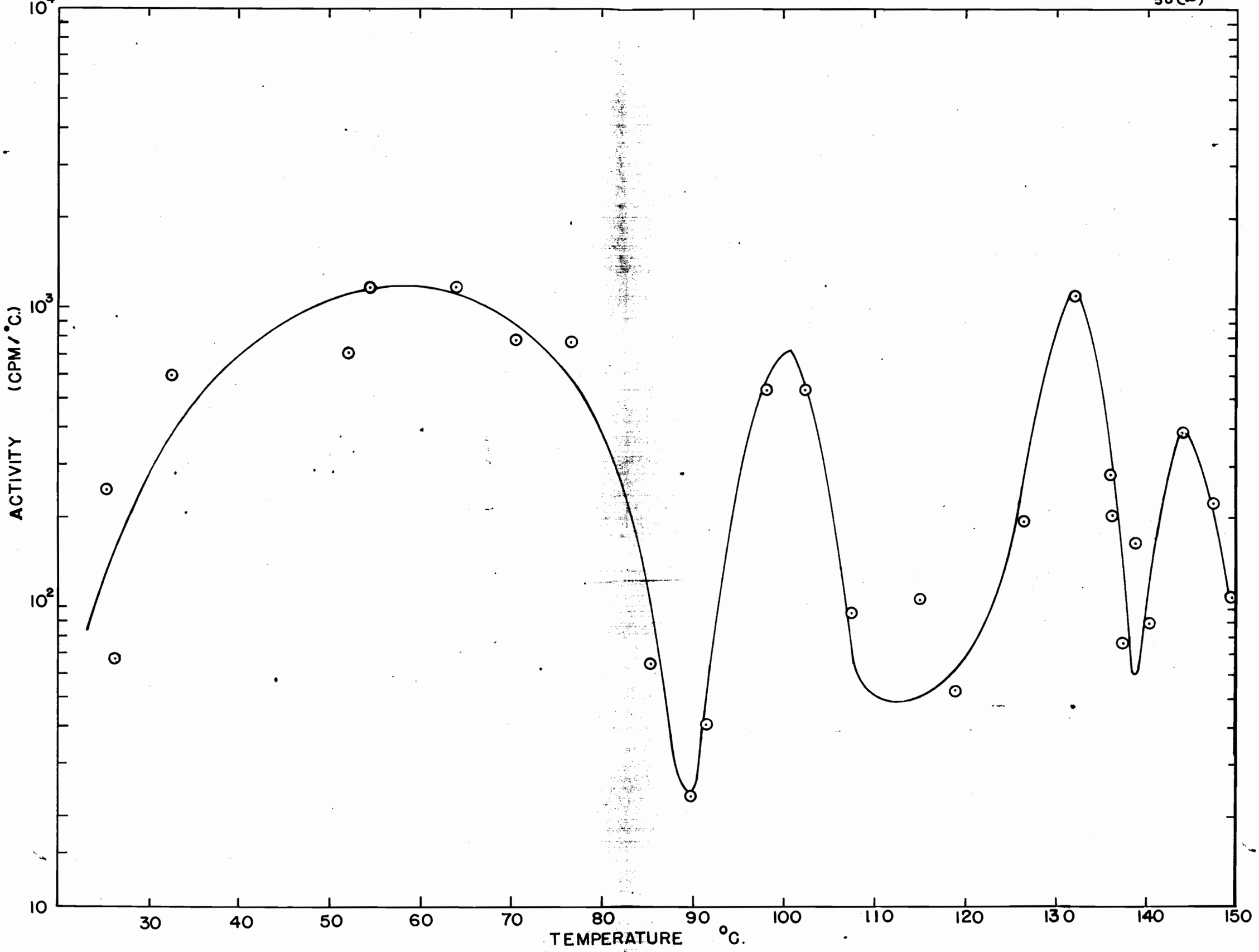
ACTIVITY (CPM/°C.)
10^4
10^3
10^2
10
30
40
50
60
70
80
90
100
110
120
130
140
150
TEMPERATURE °C.

curve is comprised of a large hump and three peaks. A similar curve was obtained when a second trial under identical conditions was performed.

A probable explanation of the hump:

Since xenon adsorbs on the surface of AgI[25,80], it is very probable that the large hump observed in the temperature range 40°C to 90°C might be due to the desorption of the xenon. The retention of radiaxenon in AgI, for weeks, has also been reported by Sullivan et al.[81].

It is a well-known fact that iodide ions are adsorbed on the surface of AgI[82,83,84]. One could therefore speculate that the desorption of iodide ions and hence xenon might give rise to the slow increase followed by a rapid decrease in activity as shown in the curve.

Peaks:

Three peaks were observed at 100 ± 2°C, 134 ± 2°C, and 144 ± 2°C respectively. In this region AgI does not decompose (the decomposition temperature is 555°C). The existence of the three peaks may be explained, however, if three modifications of AgI exist. According to Wells[85], 'There appears to be some confusion in the literature concerning the polymorphism of AgI. This compound occurs as a hexagonal mineral --- with wurzite structure ---. On being powdered the hexagonal crystals are converted into a cubic form. A mixture of two is obtained by precipitating $AgNO_3$ solution with KI. The form stable at ordinary temperatures

is apparently the cubic (γ) with zinc blende structure. At 137°C, this changes to the β form (wurzite structure) and, at 145.8°C, to the α AgI form.' Thus one can attribute the observed peaks at 134 ± 2°C and 144 ± 2°C to the transitions from the γ to the β form and the β to the α form respectively. No arguments can be given to explain the peak observed at 100 ± 2°C.

(b) The continuous recording method:

With this method a broad peak in the xenon activity vs. temperature curve at 143 ± 2°C was observed, as shown in Fig. 18. This peak might be a composite peak of 134 ± 2°C and 144 ± 2°C peaks which appeared in Fig. 17. Zimens[25] observed this peak at 145°C in the same compound in a similar investigation.

The existence of the peak in the xenon-activity vs. temperature curve is a confirmation of the polymorphism of AgI. Unfortunately, the limitation of the emanation method is that it does not yield details about crystal-structure type.

3.1.2 HgI_2

When the Xe^{135} activity was recorded as a function of temperature, the curve as shown in Fig. 19 was obtained.

A sharp peak occurred at 125.8 ± 0.1°C. This was observed in three different experiments performed under identical conditions. This peak represents a possible change in the crystal structure, and the idea is confirmed by the

Figure 18

CONTINUOUS RECORDING OF Xe^{135} ACTIVITY

AS A FUNCTION OF TEMPERATURE

IN AgI STUDIES

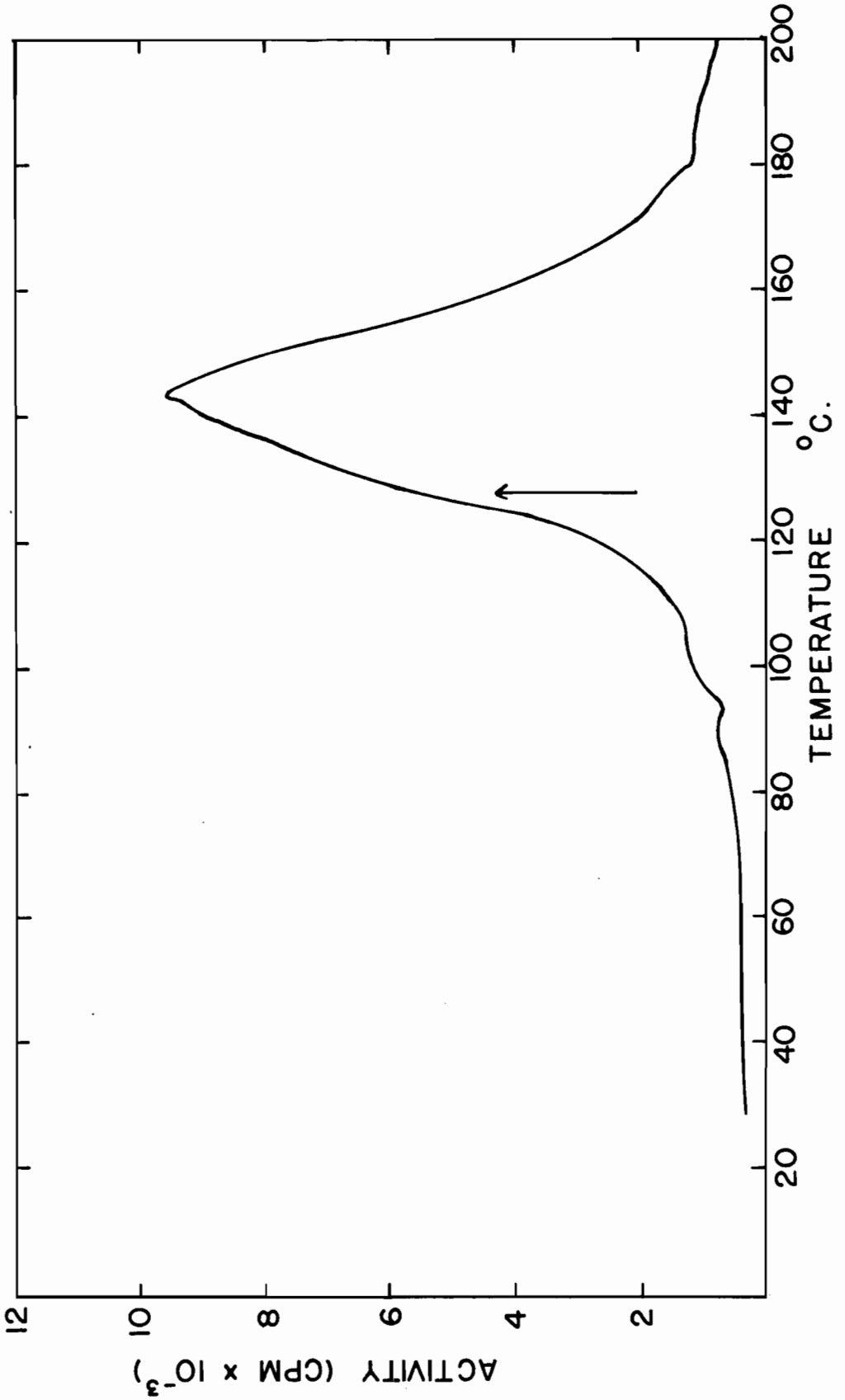
ACTIVITY (CPM x 10^{-3})
12
10
8
6
4
2
20
40
60
80
100
120
140
160
180
200
TEMPERATURE °C.

Figure 19

CONTINUOUS RECORDING OF Xe^{135} ACTIVITY

AS A FUNCTION OF TEMPERATURE

IN HgI_2 STUDIES

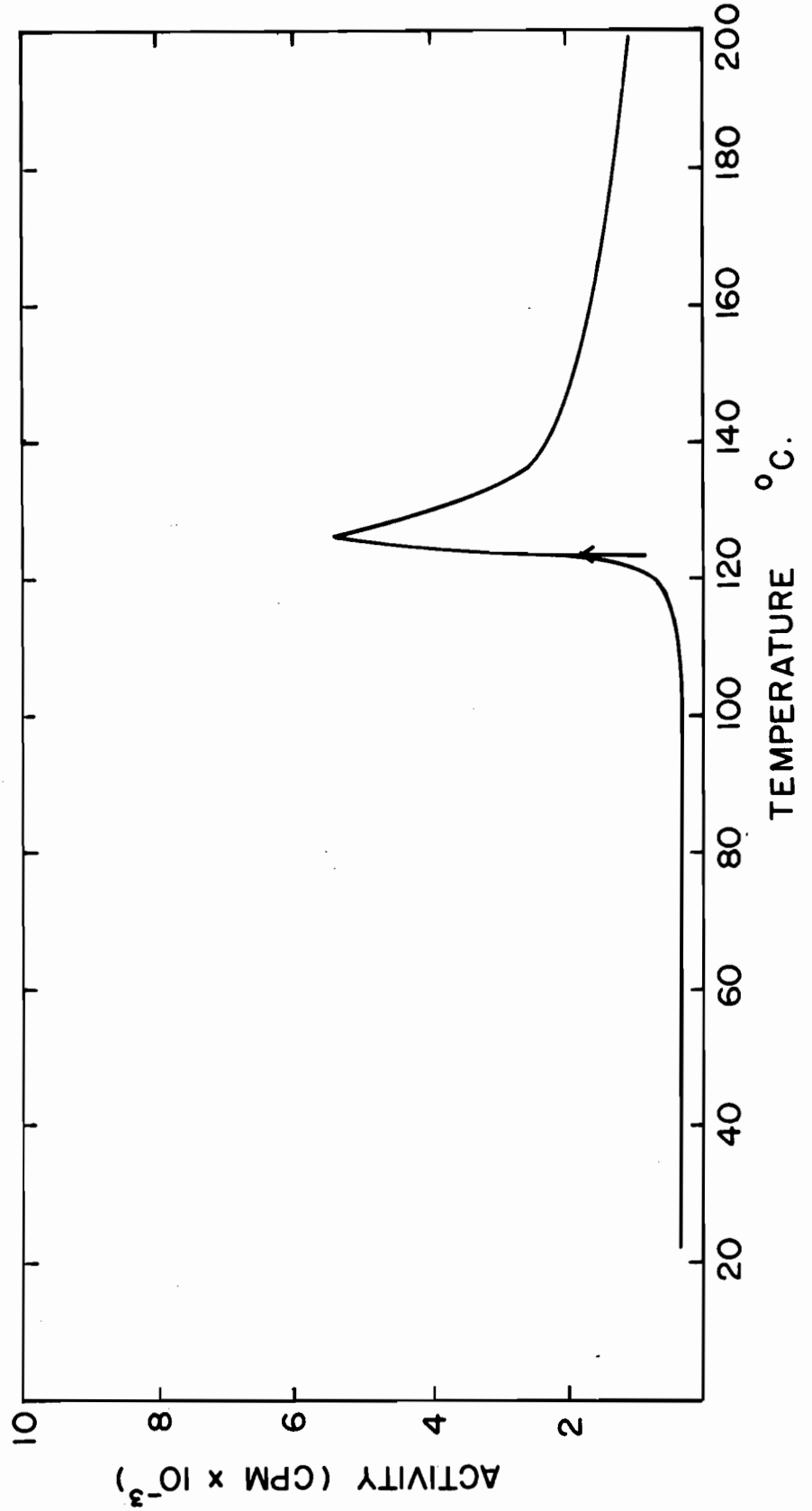
ACTIVITY (CPM x 10^{-3})
10
8
6
4
2
20
40
60
80
100
120
140
160
180
200
TEMPERATURE °C.

observed change in colour of the HgI_2 from red to yellow at 126°C. A similar observation is also reported by Gernez[86] as obtained from Ref. (87).

Thus, this method confirms the reported crystal-structure change in the HgI_2 in the temperature range 126°C - 127°C from a tetragonal to a rhombic form[60].

After the transition, the emanating power of the HgI_2 also increases, showing that the rhombic form has greater emanating power than the tetragonal form. This is illustrated in Fig. 19.

3.1.3 TlI

This method was also used for the study of TlI. Three trials were performed. A sharp peak occurred in the xenon activity vs. temperature curve at 166 ± 0.8°C as shown in Fig. 20. The peak again represents a possible change in the crystal structure at a certain temperature. This assumption is confirmed by the colour change of the TlI from yellow to red at 168°C. Sidgwick[87] has reported that the yellow layer lattice form of the TlI changes to red rhombic lattice form at 170°C. The extensive studies of Schulz[88,89] on the polymorphism of TlI further confirm the observation obtained with the present emanation method.

3.1.4 CuI

The xenon activity vs. temperature curve, as shown in Fig. 21, is slightly unusual. The Xe^{135} activity starts increasing at 80°C and reaches a maximum at 138.0 ± 2°C.

Figure 20

CONTINUOUS RECORDING OF Xe^{135} ACTIVITY

AS A FUNCTION OF TEMPERATURE

IN T1I STUDIES

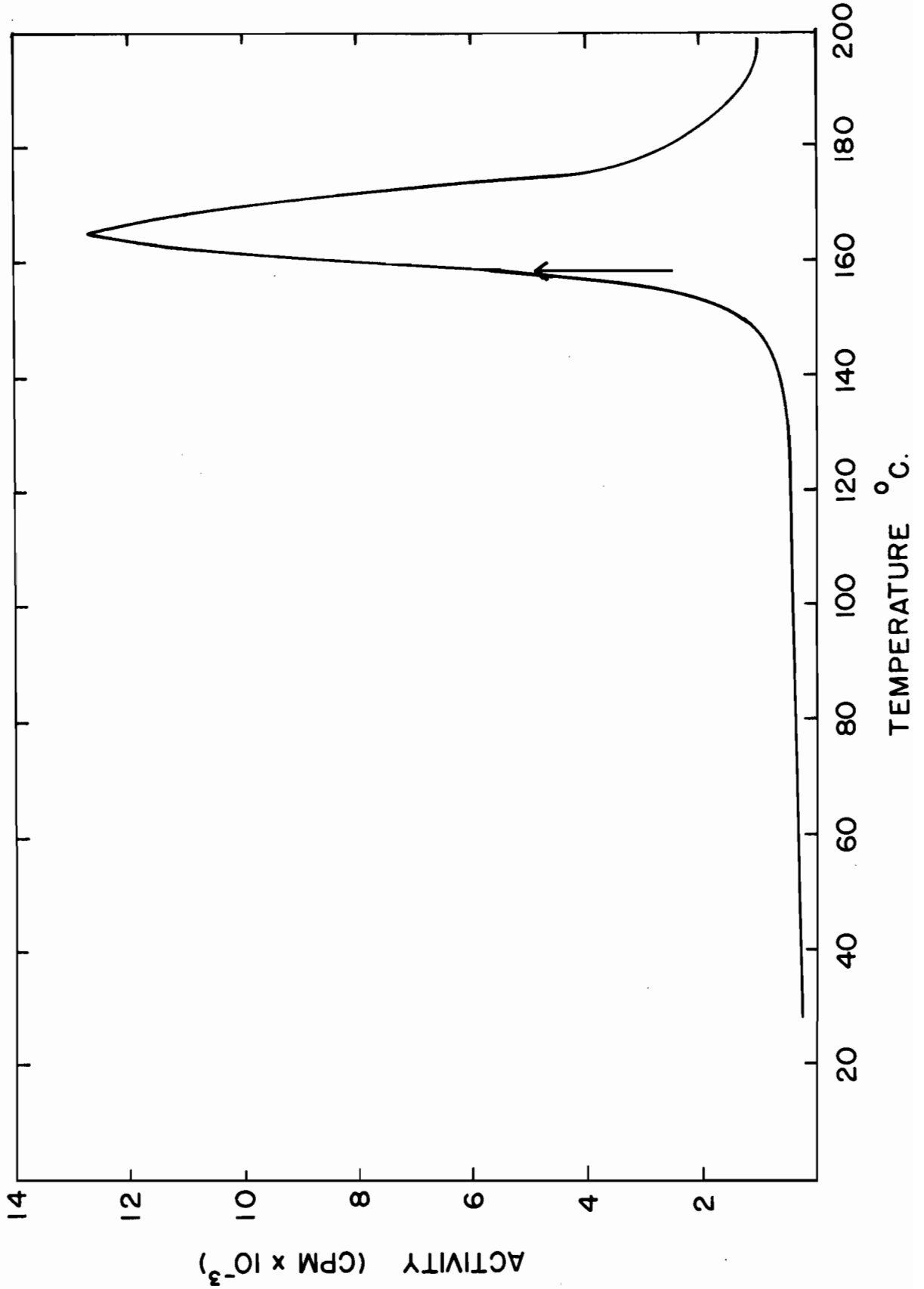
ACTIVITY (CPM x 10⁻³)
14
12
10
8
6
4
2
20
40
60
80
100
120
140
160
180
200
TEMPERATURE °C.

Figure 21

CONTINUOUS RECORDING OF Xe^{135} ACTIVITY

AS A FUNCTION OF TEMPERATURE

IN CuI STUDIES

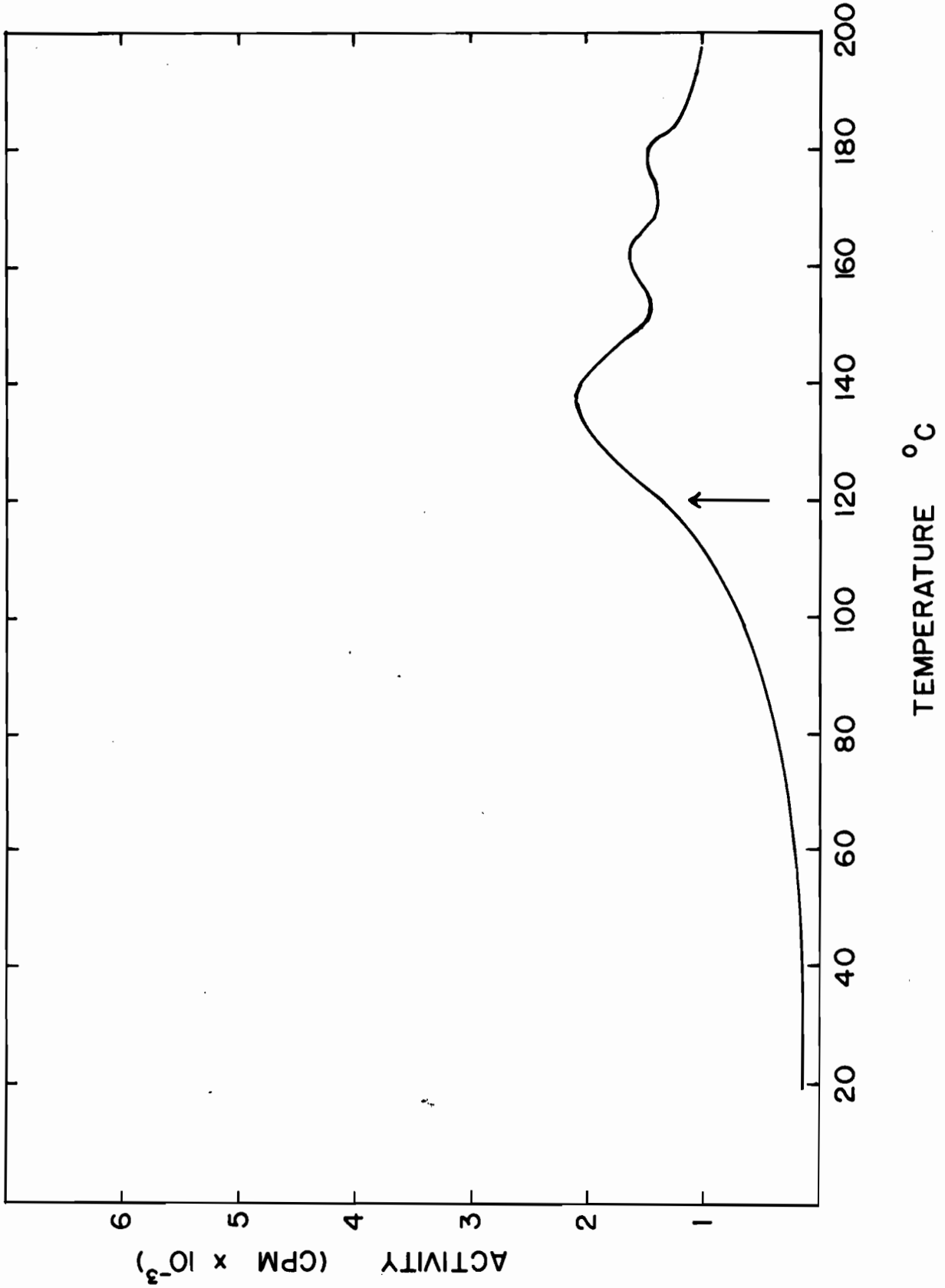
ACTIVITY (CPM x 10^{-3})
1
2
3
4
5
6
20
40
60
80
100
120
140
160
180
200
TEMPERATURE °C

There are two more maxima at 163.5 ± 2°C and 179.0 ± 2°C. It is difficult to offer any explanation for these maxima occurring at temperatures above 138°C.

Maurer[90] found that absorption of I in CuI does occur at 132°C. The probability that these maxima are due to occlusion of absorbed iodine (and hence xenon activity) is small since, during the preparation of CuI by precipitation, Cu^+ was in excess.

It is probable that the adsorption of xenon on CuI occurs, although there is no reference to this in the literature. If adsorption does occur, the xenon must be adsorbing very strongly on the CuI surface.

The most probable explanation is that there is some change taking place in the crystal structure of CuI in the temperature range above 138°C. Evidence of this comes from the studies of Miyake et al.[91]. They found by the usual methods of crystallography (X-ray diffraction method and high temperature camera, etc.) that CuI, which has normally the zinc blende type (γ) structure at room temperature, changes completely to the hexagonal wurzite (β) type at 369°C. However, anomalous change in the crystal structure begins at about 200°C. Since the emanation method of observing crystal-structure changes is a continuous one, the changes could be recorded accurately, and therefore one can state that anomalous behaviour of CuI observed by Miyake et al.[91] begins at 140°C instead of 200°C.

3.1.5 PbI_2

In the case of PbI_2, the increase in the Xe^{135} activity starts at 150°C. Two very closely placed small peaks at 172 ± 0.7°C and 176.1 ± 0.7°C, as shown in Fig. 22, are observed in the region of maximum activity. This is difficult to explain, since the cause cannot be statistical in nature.

Pinsker et al.[92] reported a hexagonal type structure for PbI_2 of which two modifications exist. When the PbI_2 is crystallized from water (as was done in the present work), the form that results depends on the velocity of crystallization. Thus both or either of the two forms may be prepared. One form is pale yellow and the other is yellow[60]. Thus the existence of the two peaks may be explained by temperature dependence of two modifications.

The 'lattice loosening effect' with the rise of temperature, as reported by Tammann[22], may be another possible explanation.

Yet another possibility could be the formation of $KPbI_3$ in the PbI_2 by the reaction:

$$2KI + Pb(NO_3)_2 \longrightarrow 2KNO_3 + PbI_2 .$$

If some KI is left adsorbed on or absorbed in the surface of PbI_2, then the reaction

$$PbI_2 + KI \longrightarrow KPbI_3$$

Figure 22

CONTINUOUS RECORDING OF Xe^{135} ACTIVITY

AS A FUNCTION OF TEMPERATURE

IN PbI_2 STUDIES

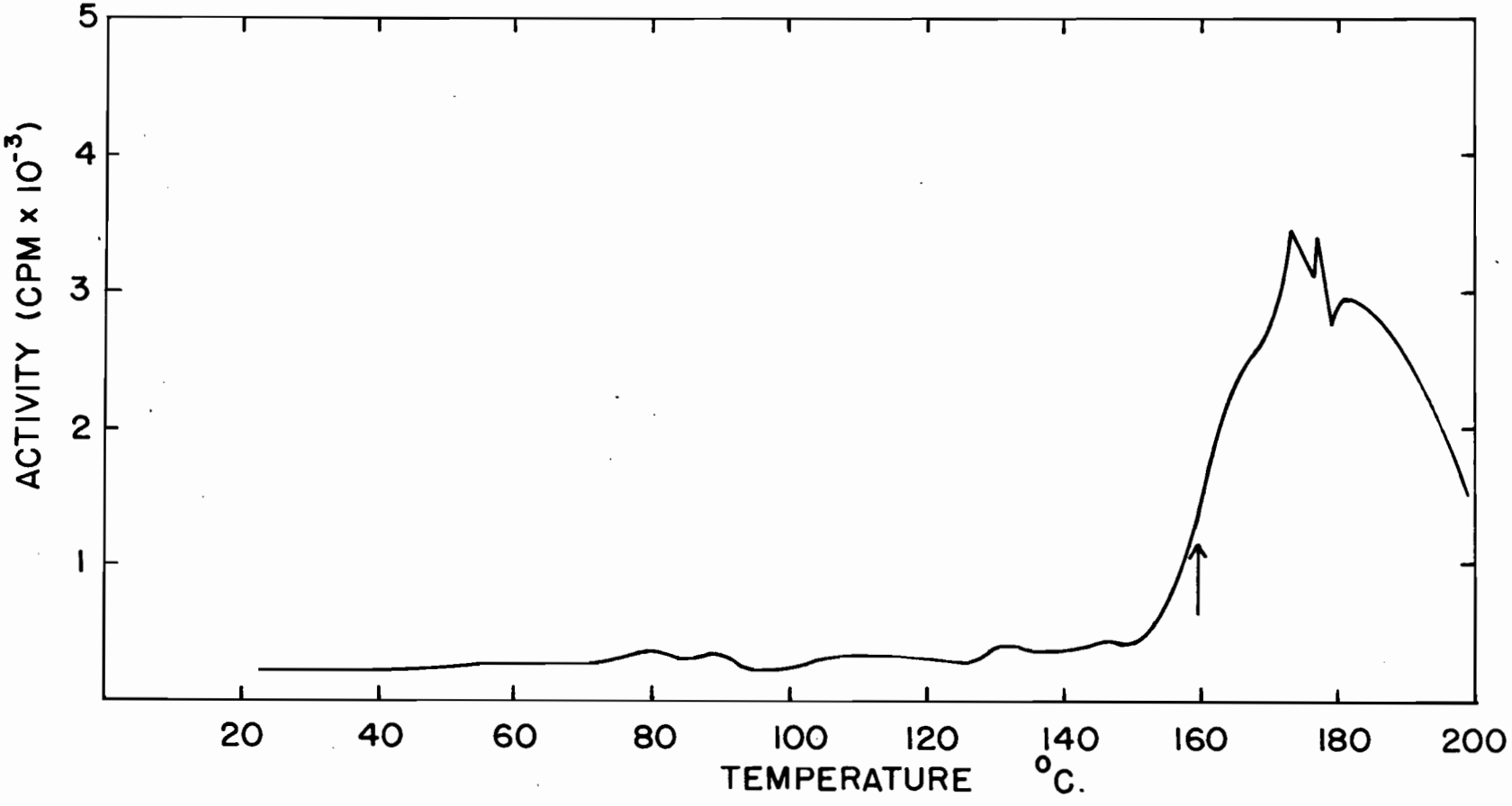
ACTIVITY (CPM x 10^{-3})
5
4
3
2
1
20
40
60
80
100
120
140
160
180
200
TEMPERATURE °C.

might have followed as a result of heating. The possibility of this reaction is reported by Hertz[93] as obtained from Ref. (94). One cannot make any definite statement about the change in emanating power.

3.2 TAMMANN LOOSENING TEMPERATURE STUDIES

The loosening temperatures[22] were computed from the Xe^{135} activity vs. temperature curve for all the compounds under investigation. Loosening temperatures are marked by arrows in Figs. 18, 19, 20, 21, and 22, and the values are listed in Table V. These values correspond to temperatures at which Xe^{135} activities have risen to one-half of the maximum.

Table V

SHOWING OBSERVED TAMMANN LOOSENING TEMPERATURES

Compound	Melting point (M.P.)	Observed loosening temp. (L.P.)	L.P./M.P.
AgI	828°K	401°K	0.484
PbI_2	685°K	433°K	0.632
TlI	713°K	431°K	0.604
HgI_2	532°K	396°K	0.744
CuI	861°K	393°K	0.456

It is seen from Table V that the ratios of the 'loosening points' to melting points are in the vicinity of 0.5 to 0.6 as predicted by Tammann.

3.3 CONCLUSIONS

The study of the crystal-structure changes of the iodides of Cu(I), Hg(II), Ag, Pb(II), and Tl(I) reveals that the results obtained by emanation method, using the $I^{135} \xrightarrow{\beta^-} Xe^{135}$ system, are in close agreement with those obtained by the conventional crystallographic techniques, as shown in Table VI.

Table VI

Compound	Transition Temperatures	
	Conventional methods	Present method
AgI	137(85)	134 ± 2°C
	145.8(85)	144 ± 2°C
HgI_2	126(86)	125.8 ± .1°C
TlI	170(87)	166 ± 0.8°C

With the use of suitable furnaces, the study could be extended to higher temperatures. Many types of heating arrangements have been reviewed by Felix and Schmeling(95) recently.

By this method the Xe^{135} in the iodine is more or less uniformly distributed. Hence the results are quite reliable.

The only limitation of this method is that the results are qualitative in a sense that they do not reveal the nature of the structural change. Cook and Prout[27] have also pointed out this fact.

PART B

4. INTRODUCTION

4.1 PREFACE

To understand the mechanism of nuclear reactions, much work has been done and more remains to be performed in order to explain various nuclear reactions, e.g. fission, spallation, fragmentation, etc.

Nuclear reactions, induced by high energy particles, are usually (and sometimes quite arbitrarily) classified[96] into four categories: spallation, in which a few or many nucleons or small clusters of nucleons are emitted from the struck nucleus; fragmentation, in which a few larger chunks of nuclear matter are split off from the struck nucleus in a fast process; fission, in which the target nucleus is divided into two or more roughly equal masses, and secondary reactions, whereby a particle that is emitted in spallation interacts with another nucleus in the target.

The various reactions which take place may involve several different kinds of mechanisms, each based on some picture of the nucleus, called a nuclear model. Various such nuclear models have been proposed, a few of which have recently been reviewed by Eden[97]. Unfortunately none of the nuclear models alone is able to explain all the observed nuclear reactions.

4.2 NUCLEAR MODELS AND THEORY OF NUCLEAR REACTIONS

4.2.1 Compound nucleus model

The detailed cross sections for nuclear reactions at low energies show very sharp resonances. In order to explain these resonances, Bohr[98] proposed a two-stage nuclear reaction mechanism.

(1) When an energetic particle is incident on a target nucleus, it first of all combines with the target nucleus and a highly excited state is formed, called a 'compound nucleus'. The kinetic energy of the projectile is immediately transferred to the nucleons of the target nucleus. The compound nucleus has a finite lifetime ($\sim 10^{-14}$ to 10^{-16} secs).

(2) The compound nucleus subsequently decays into the products of the nuclear reaction.

This model is essentially based on the assumption that these two stages are independent of each other. This then is Bohr's assumption - that the decay of the compound nucleus depends only on its energy, angular momentum and parity, but not on its particular mode of formation. The total energy, E, of the compound nucleus is the sum of the binding energies of the nucleons of the target nucleus and the kinetic energy of the incident particle.

The main feature of Bohr's compound nucleus

mechanism is the hypothesis that the lifetime of the excited state is much longer than the time required for a projectile to share its energy among the target nucleons. Consequently, the effect of many nucleon-nucleon collisions within the excited compound nucleus is that eventually sufficient energy is accumulated by one nucleon to cause its emission from the system. If this is not the case, de-excitation occurs by gamma emission.

Although the compound nucleus model provides a general mechanism for describing nuclear reactions at low and medium energies, where the projectile has sufficient time to interact strongly with the nucleons in a nucleus, it fails to explain the scattering of high energy particles from the target nucleus, where nuclear transparency is observed. This transparency is presumably due to short interacting time of the projectile with the target nucleons.

Wigner and Eisenbud[99] further developed the compound nucleus theory with the assumption that the wave function in the region where the projectile and target nucleus are close together is a linear combination of energy-independent wave functions, the combination itself having energy-dependent coefficients. A many-level formula for the reaction cross sections in terms of the derivative R-matrix and its relation to the collision matrix was suggested.

Bohr's original assumption that the mode of decay of a compound nucleus is independent of its mode of formation

was experimentally verified by Ghoshal[100]. It was established that

$$\frac{\sigma_{Ni^{60}(\alpha,n)Zn^{63}}}{\sigma_{Cu^{63}(p,n)Zn^{63}}} = \frac{\sigma_{Ni^{60}(\alpha,pn)Cu^{62}}}{\sigma_{Cu^{63}(p,pn)Cu^{62}}} = \frac{\sigma_{Ni^{60}(\alpha,2n)Zn^{62}}}{\sigma_{Cu^{63}(p,2n)Zn^{62}}} .$$

The compound nucleus, in general, explains the mechanism of nuclear reaction at low and medium energies, but not at higher energies. Consequently, in the region of overlapping energy levels, the theory was modified by Weisskopf and Ewing[101,102] by making further assumptions which are the basis of the statistical theory of nuclear reactions.

4.2.2 The Statistical model

The basic assumptions of the statistical model[101,102] are

(a) that each element of the scattering matrix has undetermined phases and the signs of these phases are random.

(b) that the partial widths are constant.

Besides these assumptions, the original assumption of Bohr remains: the statistically independent formation and decay of the compound nucleus with a high degree of interaction between target and projectile.

It is now possible to write the cross section for a nuclear reaction as

$$\sigma(a,b) = \sigma_c(a)G_c(b) \quad \ldots\ldots\ldots\ldots\ldots \quad (12)$$

where $\sigma_c(a)$ is the cross section for formation of the compound nucleus through channel a, and $G_c(b)$ is the probability that the compound nucleus will decay through channel b. The expression (12) is almost independent of the statistical assumptions[103] as quoted by Eden[97].

Thus we start with equation (12) and then assume a particular mechanism to permit calculation of the formation and decay probabilities. These probabilities, in accordance with statistical assumptions, are related by the principle of detailed balancing. In most of the cases the Fermi Gas model was used. Weisskopf and Feshbach[104] computed the probabilities of the projectile penetration into the nuclear surface and obtained the capture cross section. The decay probability is given by the expression

$$d\,\Gamma_b = \frac{m_b}{2\pi^2 \hbar^2 \rho_c(E_o)}\,\sigma_c(\varepsilon_b)\,\rho_B(E)\,\varepsilon_b\,d\,\varepsilon_b \qquad \ldots\ldots (13)$$

where m_b and ε_b are the mass and kinetic energy of the decay particle, b; E_o and E are the energies of the compound and residual nuclei respectively, Γ_b is the partial width for channel b, defined as

$$\Gamma_b = \lambda_b \hbar \qquad \ldots\ldots\ldots\ldots\ldots (14)$$

ρ_c and ρ_B are the level densities of the compound and residual nuclei respectively. If the Fermi Gas model is assumed, the form of the level densities will show a

Maxwellian distribution. Thus, when all levels are occupied, the probability of the emission of a particle is the same from all the levels.

Measurements of the energy spectra of emitted neutrons[105,106,107,108] and protons[109] showed them to be approximately Maxwellian as required by the statistical theory.

Shapiro[110] has applied the statistical theory[104] to calculate the cross sections for the formation of a compound nucleus by protons, deuterons, and alpha particles. The results were in close agreement with those obtained experimentally, although it was found that in many cases the cross sections of the different isotopes of the same element differed from each other, and hence from the calculated cross sections, by a factor of two.

Since the reactions of (p,pxn) type are inhibited by the coulomb barrier, both in the entrance and exit channels, statistical theory predicts that such reactions in heavy target elements will have negligibly small cross sections compared with the (p,xn) type reactions. Bell and Skarsgard[111] found that near the peak of a particular (p,xn) curve the (p,p(x - 1)n) cross sections were indeed small.

Several authors[112,113,114] reported qualitative agreement between experimentally determined cross sections with those predicted by the statistical theory.

4.2.3 Optical model

The compound nucleus theory of Bohr assumes that every nucleon that penetrates into the nucleus is at once captured to form a compound nucleus. On the other hand, the single particle model (shell model of Mayer and Jensen[115]) requires that the incident nucleons have long mean free paths. In spite of the fact that these two models are in direct conflict, there are remarkable experimental observations in favour of each of them. To overcome this difficulty, i.e. strong absorption and high energy nuclear scattering, Fernbach et al.[116] introduced the concept of a complex potential or 'cloudy crystal ball model'. This model assumes 'that the compound nucleus formation takes place neither at once nor with complete certainty but rather eventually and even then with a certain probability'[117].

Mathematically, it can be represented as

$$V = (V_o + iW_o) \quad \ldots\ldots\ldots\ldots\ldots\ldots \quad (15)$$

where V is the depth of the potential well, V_o is the transmission coefficient responsible for scattering of the particles, and the imaginary part (iW_o) responsible for absorption. A large value of W_o corresponds to a short mean free path and hence strong absorption. Both V_o and W_o vary with the kinetic energy of the projectile. To explain the neutron resonance reactions at low energies, the transmission coefficient, V_o, across the nuclear surface is very small.

Therefore, once a nucleon is inside a nucleus, it may be reflected several times by the inside of the nuclear surface until it is eventually captured to form the compound nucleus. At higher incident energies, the transmission coefficient V_o increases rapidly so that, even though the mean free path is shorter, nucleons are more likely to escape.

In this model an incident particle striking the nucleus is analogous to a 'light beam' incident on a 'cloudy crystal ball'. If the 'crystal ball' is clear, most of the incident light beam will be reflected and refracted, i.e. it corresponds to scattering of high energy particles. Thus cloudiness of the crystal ball, corresponding to the imaginary part of the expression (15), is responsible for the absorption of the incident particles.

With the advent of high energy particle accelerators, the experimental results at higher energies show deviations both from the compound nucleus theory and from the statistical theory. For example, the compound nucleus theory predicts that at energies of about 100 Mev the yields of nuclides with atomic number near that of the target nucleus would be low, while the yields of the nuclides far removed from the target would be high. The observations of Cunningham et al.[118] show exactly the opposite.

The excitation functions of reactions above 100 Mev exhibit broad maxima instead of sharp peaks with a tendency to have long low tails[119,120], as required by the continuum

theory and the statistical theory.

In order to explain high energy nuclear reactions, Serber[121] proposed a cascade evaporation model for nuclear reactions in general.

4.2.4 Serber model

According to Serber[121], a nuclear reaction proceeds in two stages, viz. (a) A projectile incident on a nuclear surface will penetrate into the nucleus to a certain depth and then collide with either a proton or a neutron. As a result of this collision, the two partners may escape from the nucleus or they may undergo further collisions leading to a prompt shower or cascade. This stage has a very short interaction time. It is apparent that the development of the nucleon cascade will be governed by the mean free path of the nucleons moving within the nuclear matter.
(b) Following the cascade stage, the residual nucleus has a certain amount of excitation energy left. The de-excitation of the residual nucleus may take place by particle emission (called evaporation process) only if the excitation energy exceeds the energy of the least tightly bound nucleon. This stage will be more or less similar to the mechanism of direct formation of the compound nucleus. In general, the evaporation stage is responsible for the low energy reactions[122].

The theory was further developed by Goldberger[123].

4.2.5 Validity of Serber model and Monte Carlo calculations

Soon after the Serber[121] theory, many workers[123,124,125,126,127,128,129] computed the theoretical cross sections in many hypothetical nuclear reactions, using Monte Carlo techniques.

Monte Carlo techniques make use of electronic computers. The history of each hypothetical collision is followed by considering the kinetic energy of the projectile, coulomb barrier, binding energy of the nucleons, collision parameter, the residual excitation energy after the cascade, etc. At each stage of the hypothetical cascade process, the new values for energy and direction of the nucleons are selected by the use of a set of random numbers weighted according to the kinematics of the elementary process. Each nucleon which becomes involved in the cascade is followed until it reaches the ground state or is lost from the nuclear surface.

In order to obtain sufficient statistical accuracy, the calculation is repeated for many cascades, each initiated by a new incident nucleon.

In one such calculation, Bernadini et al.[124] and Metropolis et al.[129] obtained the results for the expected energy spectra and angular distribution of protons in the bombardment of AgBr by 360 Mev protons. The results thus obtained were compared with those obtained by nuclear emulsion

techniques. It was found that the results were in agreement to some degree. The statistical accuracy of the experimental results is often not very high, but neither is that of the corresponding Monte Carlo calculations[122].

Rudstam[127] studied the spallation of As by 170 Mev protons, obtaining the results radiochemically. He compared these results with those he obtained by Monte Carlo calculations, based on the cascade-evaporation model, and found the agreement to be satisfactory.

Metropolis et al.[129] found that the results of Monte Carlo calculations, based on the cascade-evaporation model, gave a mass-yield distribution in close agreement with those of Seaborg et al.[130] for the spallation of Cu with 340 Mev protons.

Recently, Harvey[122] published an excellent review on the cascade-evaporation model for spallation reactions.

The cascade process merges into the evaporation process[96] as the energies of the involved nucleus become comparable with the nucleon energies in the compound nucleus.

4.3 SPALLATION REACTIONS AND THE SCOPE OF THE PRESENT WORK

A brief definition of the spallation reaction is given in Section 4.1. On the basis of this definition a spallation reaction induced by protons can be expressed[127] as:

$$Z^A + p = Z_1^{A_1} + \nu_1 p + \nu_2 n + \nu_3 d + \nu_4 H^3 + \nu_5 He^3 + \nu_6 \alpha + \text{heavy fragments} \quad \ldots\ldots\ldots (16)$$

where Z^A is the target nucleus and $Z_1^{A_1}$ is the residual nucleus. ν_1, ν_2, ν_3, etc. are numbers.

Thus the reactions of the type (p,xn) and (p,pxn) and other such simple reactions are usually classified as spallation reactions. As the bombardment energy increases, other reactions such as fragmentation and fission start competing, depending upon the mass number of the target nucleus.

Some of the spallation reactions at low energies (less than 30 Mev) can be explained in terms of the compound nucleus theory, and a few of them in terms of the statistical and cascade-evaporation theories. These theories have been discussed briefly in Section 4.2.

In the present work, the author proposes to study the (p,xn) and (p,pxn) reactions radiochemically, induced by protons of energies 7 to 100 Mev in a medium weight nucleus. The target nucleus selected was I^{127} which is monoisotopic. This simplifies the conclusions which can be reached.

(p,xn) reactions of iodine have been studied by Dropesky and Wiig[131], Hyde and Mathur[132], and several other workers[133,134]. The study was only confined to the identification of the products and their decay schemes.

(p,pxn) reactions of iodine were studied by various workers[135,136,137]. Ladenbauer[135], Kuznetsova et al.[137], and Dropesky[136] reported the cross sections for these reactions at energies higher than 100 Mev.

The identification and disintegration schemes of the products of (p,pxn) reactions have been worked out by several researchers[138,139,140,141].

Ladenbauer had also studied other reactions of iodine such as (p,2pxn), (p,p π^+), (p,2p π^+), and (p,2p π^-) radiochemically, with protons of energies 0.25 to 6.2 Bev. She also studied the reaction of iodine with 0.25 to 0.72 Bev alpha particles.

Winsberg[142] investigated the interaction of 120 Mev negative pions and negative muons with iodine. The radiochemical yields of various reactions have been reported.

Recently Silvester and Jack[143] studied the $I^{127}(d,p)I^{128}$ reaction radiochemically at moderate energies.

Very little information is available about (p,xn) and (p,pxn) reactions of iodine below the 100 Mev range.

Unfortunately, in the present work the author could not study I^{127}(p,xn) reactions beyond x = 1 for the following reasons:

(a) I^{127}(p,2n) and I^{127}(p,4n) reactions yield stable Xe^{126} and Xe^{124} respectively.

(b) The products of I^{127}(p,3n) and I^{127}(p,6n) reactions are Xe^{125} and Xe^{122} respectively. The half-lives are

very similar (18 hrs and 19 hrs respectively) and the decay curves are difficult to resolve since the gamma-ray energies are similar.

(c) The gamma-ray energies of Xe^{123} are again comparable with Xe^{125} and Xe^{122}.

These facts are illustrated in Fig. 23, which is part of the chart of the nuclides.

Attention was therefore focussed on the studies of $I^{127}(p,pxn)$ reactions. The range covered was x = 1 to x = 4. Reactions of this type, which involve inelastic scattering of incident protons, are inhibited by the coulomb barrier in both the entrance and exit channels, as pointed out in Section 4.2.2, and hence are rather important.

Figure 23

PART OF THE CHART OF THE NUCLIDES

IN THE REGION UNDER INVESTIGATION

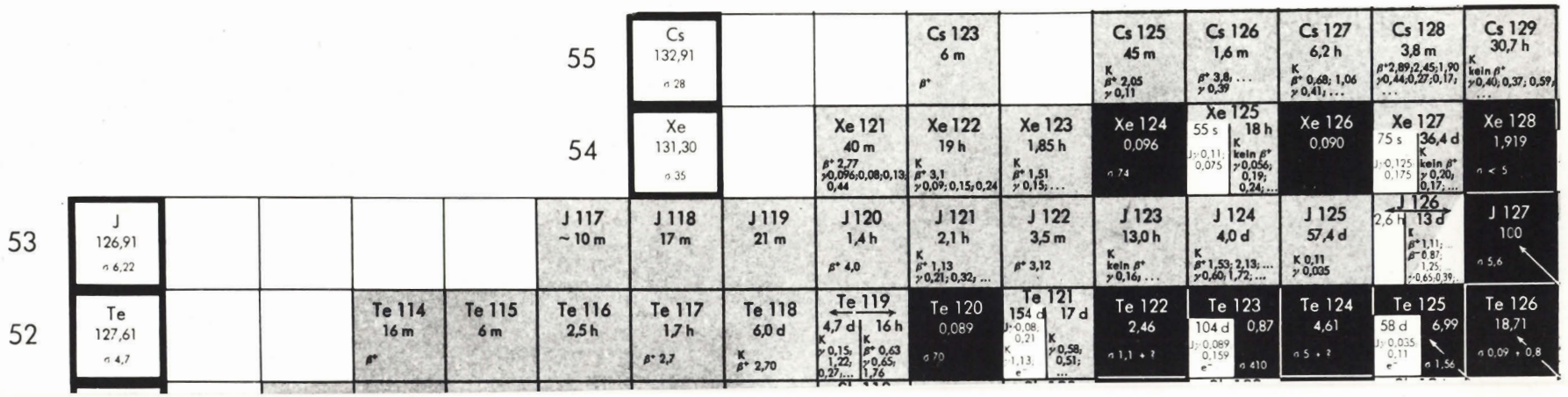
55
54
53
52
Cs 132,91 σ 28
Xe 131,30 σ 35
J 126,91 σ 6,22
Te 127,61 σ 4,7
Cs 123 6 m β+
Cs 125 45 m K β+ 2,05 γ 0,11
Cs 126 1,6 m β+ 3,8; ... γ 0,39
Cs 127 6,2 h K β+ 0,68; 1,06 γ 0,41; ...
Cs 128 3,8 m β+ 2,89; 2,45; 1,90 γ 0,44; 0,27; 0,17; ...
Cs 129 30,7 h K kein β+ γ 0,40; 0,37; 0,59; ...
Xe 121 40 m β+ 2,77 γ 0,096; 0,08; 0,13; 0,44
Xe 122 19 h K β+ 3,1 γ 0,09; 0,15; 0,24
Xe 123 1,85 h K β+ 1,51 γ 0,15; ...
Xe 124 0,096 σ 74
Xe 125 55 s J: 0,11; 0,075 | 18 h K kein β+ γ 0,056; 0,19; 0,24; ...
Xe 126 0,090
Xe 127 75 s J: 0,125 0,175 | 36,4 d K kein β+ γ 0,20; 0,17; ...
Xe 128 1,919 σ < 5
J 117 ~ 10 m
J 118 17 m
J 119 21 m
J 120 1,4 h β+ 4,0
J 121 2,1 h K β+ 1,13 γ 0,21; 0,32; ...
J 122 3,5 m β+ 3,12
J 123 13,0 h K kein β+ γ 0,16; ...
J 124 4,0 d K β+ 1,53; 2,13; ... γ 0,60; 1,72; ...
J 125 57,4 d K 0,11 γ 0,035
J 126 2,6 h | 13 d K β+ 1,11; β− 0,87; 1,25; γ 0,65; 0,39; ...
J 127 100 σ 5,6
Te 114 16 m β+
Te 115 6 m
Te 116 2,5 h
Te 117 1,7 h β+ 2,7
Te 118 6,0 d K β+ 2,70
Te 119 4,7 d K γ 0,15; 1,22; 0,27; ... | 16 h K β+ 0,63 γ 0,65; 1,76
Te 120 0,089 σ 70
Te 121 154 d K J: 0,08; 0,21 e− 1,13 | 17 d K γ 0,58; 0,51; ...
Te 122 2,46 σ 1,1 + ?
Te 123 104 d J: 0,089 0,159 e− | 0,87 σ 410
Te 124 4,61 σ 5 + ?
Te 125 58 d J: 0,035 0,11 e− | 6,99 σ 1,56
Te 126 18,71 σ 0,09 + 0,8

5. EXPERIMENTAL

5.1 TARGET

Cuprous iodide was selected from among the compounds of iodine for bombardments, for the following reasons:

(a) The monitor reactions employed in this work were $Cu^{63}(p,n)Zn^{63}$ and $Cu^{65}(p,pn)Cu^{64}$. Thus there is a stoichiometric distribution of the monitor inside the target.

(b) Cuprous iodide is quite stable at high temperatures, the decomposition temperature being $> 1200^{\circ}C$[60].

(c) It is commercially available with a high degree of purity.

The 'spec pure' grade of cuprous iodide was obtained from Johnson, Matthey and Co., Montreal. Spectrographic examination of CuI shows the following impurities[144]:

Element	Estimate of quantity present (parts per million)
Na	2
Ca, Mg, Si, Ag	each element less than 1

However, it is unlikely that the impurities quoted above would interfere to an appreciable extent in this work. A weighed amount of this compound was introduced into thin

aluminum tubing* of 2S purity, having an outside diameter of 0.0625" ± 0.005" with a wall thickness of 0.0015" ± 0.0005". One end of the aluminum tubing was previously sealed into an L shape by a mechanical press. The amount of CuI used was 10 to 15 mg. In order to inhibit the xenon losses, the aluminum tubing containing the target was pressed under the hydraulic press at both ends as shown in Fig. 6. The possibility of xenon escaping through the walls of the aluminum tubing at higher energies by diffusion has been ruled out by Adda et al.(145) and Neil(146). The possibility of escape of xenon through the mechanically-sealed ends of the aluminum was checked by studying the results of an auxiliary radiation of cuprous iodide in a sealed quartz capsule (see later). The target was then mounted on the target holder as illustrated in Fig. 6.

5.2 BOMBARDMENTS

5.2.1 Irradiation procedures

The entire target assembly was mounted on the water-cooled probe of the McGill Synchrocyclotron. The calibration curve for radial distances vs. proton beam energy, duly corrected for radial oscillation by Kirkaldy(57) as shown in Fig. 7, was used. In order to maximize the yields of product nuclides at desired energies, the 'Vertical Oscillation Maximum Yield Curve' was used (Fig. 24). The

*Precision Tube Co., Philadelphia, Pa.

Figure 24

VERTICAL POSITION OF THE PROTON BEAM

OF THE McGILL SYNCHROCYCLOTRON

AS A FUNCTION OF ENERGY

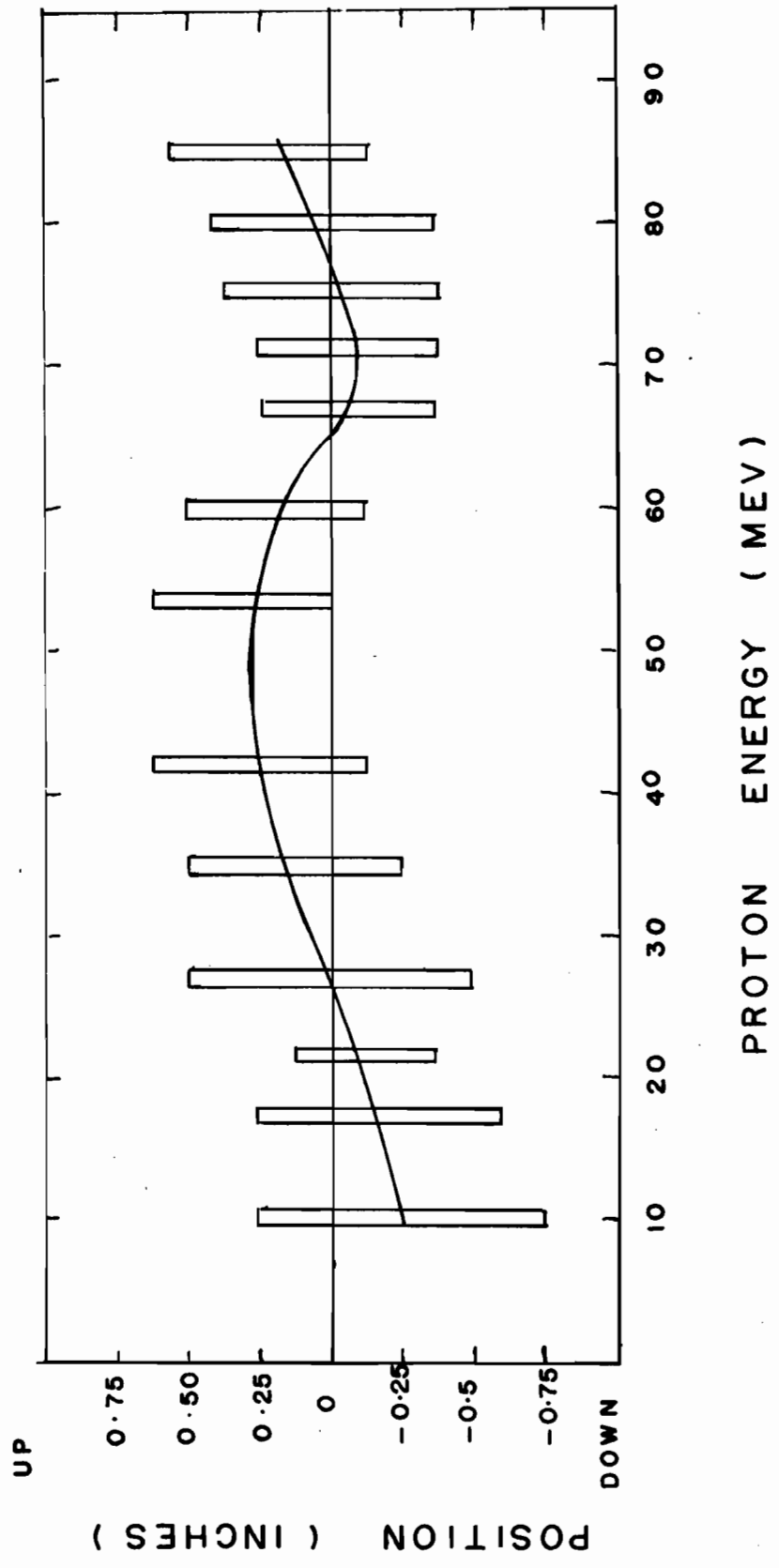
UP
0·75
0·50
0·25
0
-0·25
-0·5
-0·75
DOWN
POSITION (INCHES)
10
20
30
40
50
60
70
80
90
PROTON ENERGY (MEV)

irradiation time varied from 10 to 30 minutes, depending upon the half-lives of the product nuclides.

Energy degradation of the proton beam by the target container was calculated at various energies on the basis of range-energy values of Sternheimer[147]. The maximum degradation in these experiments was found to be 0.6 Mev. This correction was not considered significant, since the energy spread of the McGill Synchrocyclotron proton beam itself is $\pm$ 2 Mev.

5.2.2 Beam monitoring

In order to get the absolute values of the cross sections for the various reactions under observation, it was necessary to know the flux of protons hitting the target. This was achieved by using a beam monitor. As mentioned earlier, the copper in the target compound was used as a beam monitor. The monitor reaction $Cu^{63}(p,n)Zn^{63}$ was used below 12 Mev, and cross-section values obtained by Ghoshal[148] were employed for this reaction. The monitor reaction $Cu^{65}(p,pn)Cu^{64}$ was employed in the energy region above 12 Mev. The cross-section values, as obtained by Meghir[149], were used for this reaction. The excitation functions of the monitor reactions, as obtained by Ghoshal[148] and Meghir[149], are shown in Figs. 25 and 26 respectively, and the values used are given in Table VII (P.110).

Figure 25

GHOSHAL'S EXCITATION FUNCTION FOR THE

$Cu^{63}(p,n)Zn^{63}$ REACTION

(Reference 148)

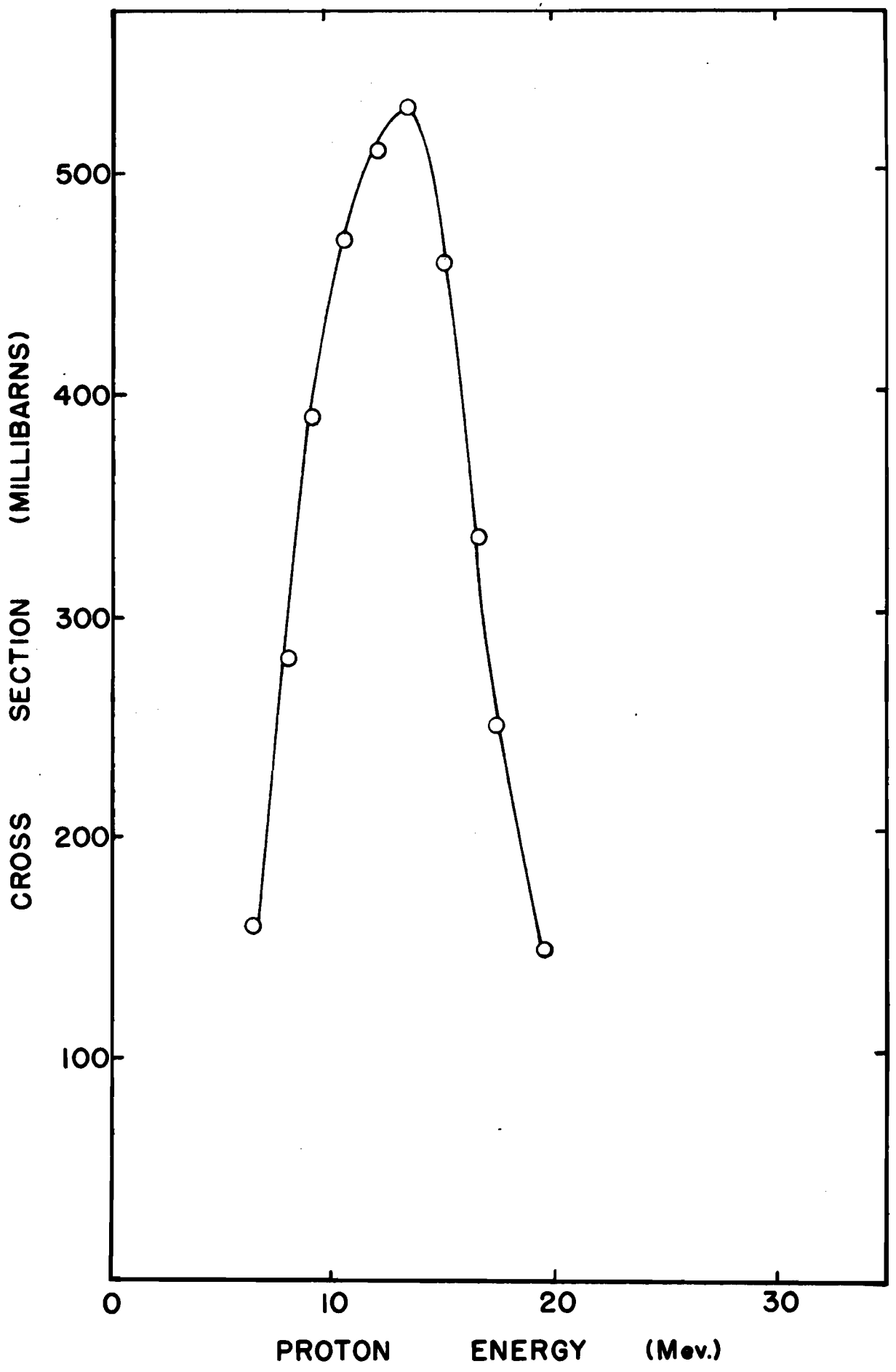
CROSS SECTION (MILLIBARNS)
500
400
300
200
100
0
10
20
30
PROTON ENERGY (Mev.)

Figure 26

MEGHIR'S EXCITATION FUNCTION FOR THE

$Cu^{65}(p,pn)Cu^{64}$ REACTION

(Reference 149)

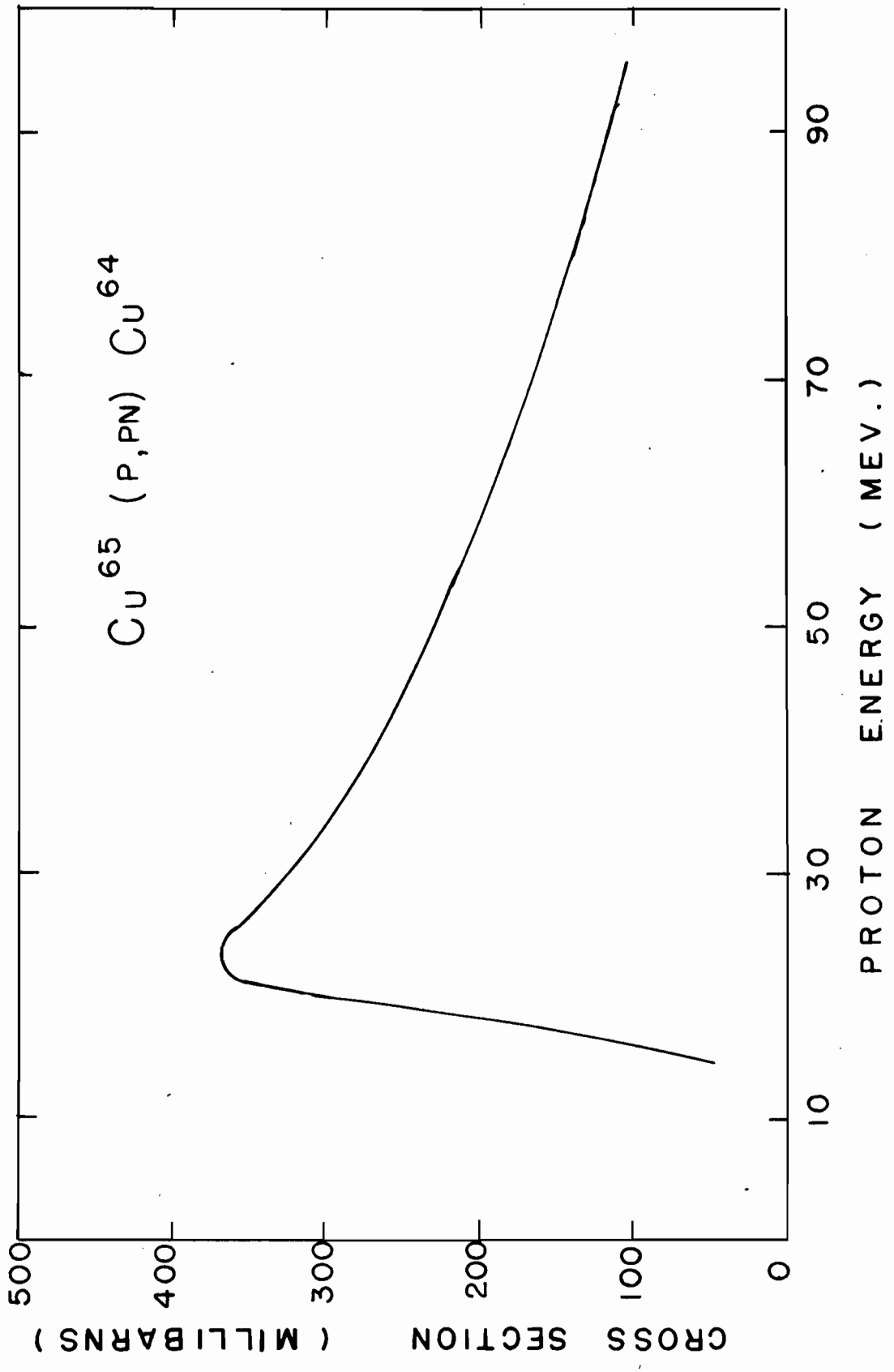
Cu^{65} (p,pn) Cu^{64}
CROSS SECTION (MILLIBARNS)
0
100
200
300
400
500
10
30
50
70
90
PROTON ENERGY (MEV.)

5.3 CHEMICAL SEPARATION PROCEDURES

5.3.1 Xenon

Xenon, formed by $I^{127}(p,xn)$ reactions, was separated first. Because of the inert nature of xenon, it was separated by freezing it at liquid nitrogen temperature in vacuum. The method used in the present work can best be explained with the help of Fig. 27.

The entire target was detached from the target holder and introduced into a 25 ml flask along with a few pellets of NaOH (about 5 gms) and a magnetic stirring bar. The flask was then evacuated by a DuoSeal vacuum pump coupled with an oil diffusion pump until the pressure inside the flask was reduced to less than 1 micron. A consolidated vacuum thermocouple gauge, type GTC-004, was used to measure the pressure.

The flask and the traps were isolated from each other by closing all the stopcocks. Approximately 2 ml (at room temperature and pressure) of inactive xenon was then introduced into the flask by means of stopcock S_1 and S_2. Water ($5 \sim 7$ ml) from the reservoir, R_2, was then introduced into the flask, and the magnetic stirrer switched on. The NaOH dissolved the aluminum and reacted with the $CuI^{(150)}$, giving NaI and Cu_2O. Radioxenon was thereby mixed with inactive xenon as a result of the stirring which was done for five minutes in each trial. The reaction is exothermic, and the hydrogen evolved (due to the reaction of NaOH on aluminum)

Figure 27

SYSTEM FOR THE SEPARATION OF XENON

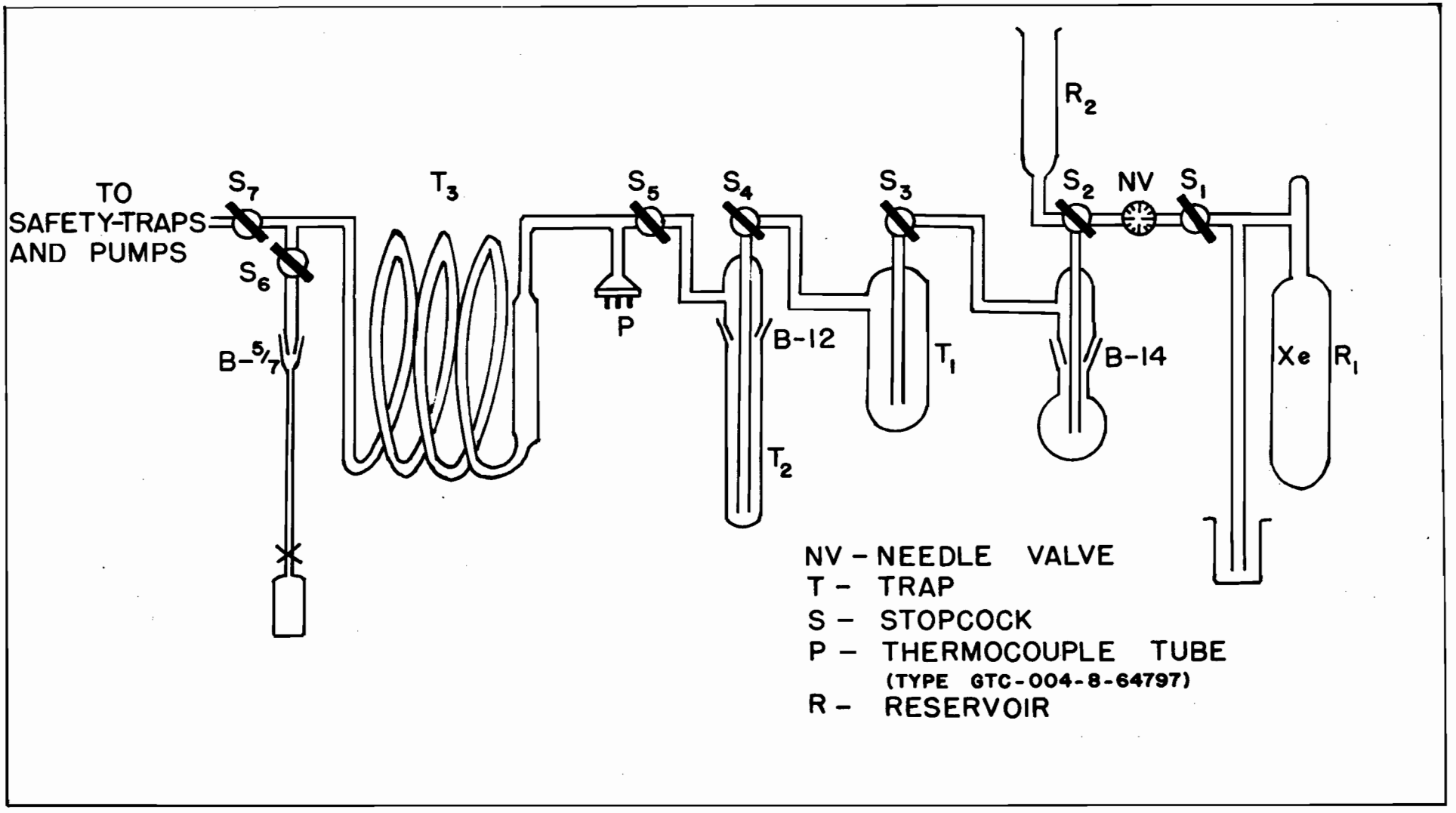
TO
SAFETY-TRAPS
AND PUMPS
S7
S6
B-5/7
T3
P
S5
S4
B-12
T2
S3
T1
R2
S2
NV
S1
B-14
Xe
R1
NV - NEEDLE VALVE
T - TRAP
S - STOPCOCK
P - THERMOCOUPLE TUBE
(TYPE GTC-004-8-64797)
R - RESERVOIR

started building up its pressure in the flask, so that the flask was occasionally cooled to 0°C.

The mixture of Xe and H_2, and inevitably of some water vapour, was transferred to trap T_1 by opening the stopcock S_3. T_1 contained stainless steel balls and was kept in a bath of dry ice and acetone ($\sim$ -85°C). The stainless steel balls were used to achieve better heat transfer. Thus most of the water vapour and free iodine (if unreacted) was held in the trap, T_1. The mixture of Xe and H_2 at this stage was transferred to the trap, T_2, by opening stopcock S_4. Trap T_2 held the remaining water vapour, since this was also kept at about -85°C.

The mixture (Xe + H_2) was finally transferred to the radiator trap, T_3, by opening stopcock S_5. This trap was specially designed from very thin-walled pyrex glass tubing in the form of a five-turn spiral. The trap, T_3, was kept in a fresh liquid nitrogen bath (-195.8°C). It was presumed that at this temperature (-195.8°C) all the xenon would freeze effectively (freezing point of xenon -112°C[60]). After the hydrogen was pumped out from trap T_3, containing frozen xenon, a pressure of less than a micron was observed. In each trial about five minutes were allowed for the completion of the freezing process of xenon in the trap, T_3. It was seen that most of the xenon was frozen in the first two spirals because it was possible to observe white snow-like condensation of xenon on the walls of the radiator trap, T_3.

The cycle of successive transfers of the (Xe + H_2) mixture from the flask to the radiator trap was continued until the pressure inside the system reached less than a micron. This took about 20 minutes.

Xenon was finally distilled into a pyrex glass ampoule specially designed for this work, as shown in Fig. 28. The dimensions were selected in accordance with the standard activity measurement procedures in this Laboratory. The ampoules were sealed and the activity measured by a 3" x 3" NaI(Tl) scintillator coupled to a CDC* 100 channel pulse height analyser.

5.3.2 Copper

After the xenon was separated, the contents of the flask were transferred into a 50-ml centrifuge tube along with 10 mg of Zn^{++} carrier. In order to separate Cu_2O, the entire bulk was centrifuged. Since products such as Zn, Ni, Co are also formed as spallation products of Cu, it was necessary to purify Cu_2O further. The ion exchange method of Nelson and Kraus[151] was adopted to separate Cu from its spallation products. The Cu_2O was dissolved in a minimum amount of concentrated HCl and the solution adsorbed on the top of a column of Dowex-1 (100 - 200 mesh) anion exchange resin. Ni was first eluted with 12 M HCl (two times the column volume) and then Co with 4.5 M HCl (three times column volume).

---

*Computing Devices of Canada Limited, Ottawa, Ontario.

Figure 28

SPECIALLY DESIGNED GLASS AMPOULE

FOR MEASURING XENON ACTIVITY

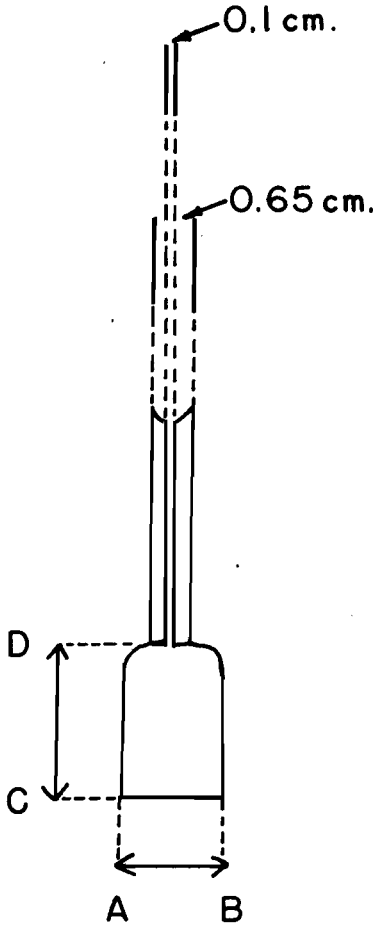

AB = 1.7 ± 0.1 cm.

CD = 1.45 ± 0.05 cm.

Finally, Cu was eluted with 1.5 M HCl and the solution made up to a known volume with distilled water.

5.3.3 Iodine

After Xe and Cu were separated, the remainder contained Zn, Al, I and Na. Due to the excess of NaOH, Zn and Al would probably form sodium zincate and sodium aluminate. The final solution was made acidic (pH 4 - 5) to free zinc and aluminum. Al was precipitated as $Al(OH)_3$ by the addition of NH_4Cl and NH_4OH. The suspension was centrifuged and the precipitate discarded.

The remaining solution contained iodine and zinc. Iodine was separated by solvent extraction[59]. Details of the method are given in Appendix I.

5.3.4 Zinc

After I, Cu and Xe were separated, it was presumed that only Zn was left, since it is unlikely that below 12 Mev any reaction other than $Cu^{63}(p,n)Zn^{63}$ would occur appreciably.

A summary of the chemical separations is given on the following page.

5.4 CHEMICAL YIELD DETERMINATIONS

5.4.1 Xenon

The extraction yield of xenon was believed to be very close to 100% for the following reasons:

(a) In an auxiliary experiment CuI was bombarded in a sealed quartz tube. After making corrections for

SUMMARY OF CHEMICAL SEPARATIONS

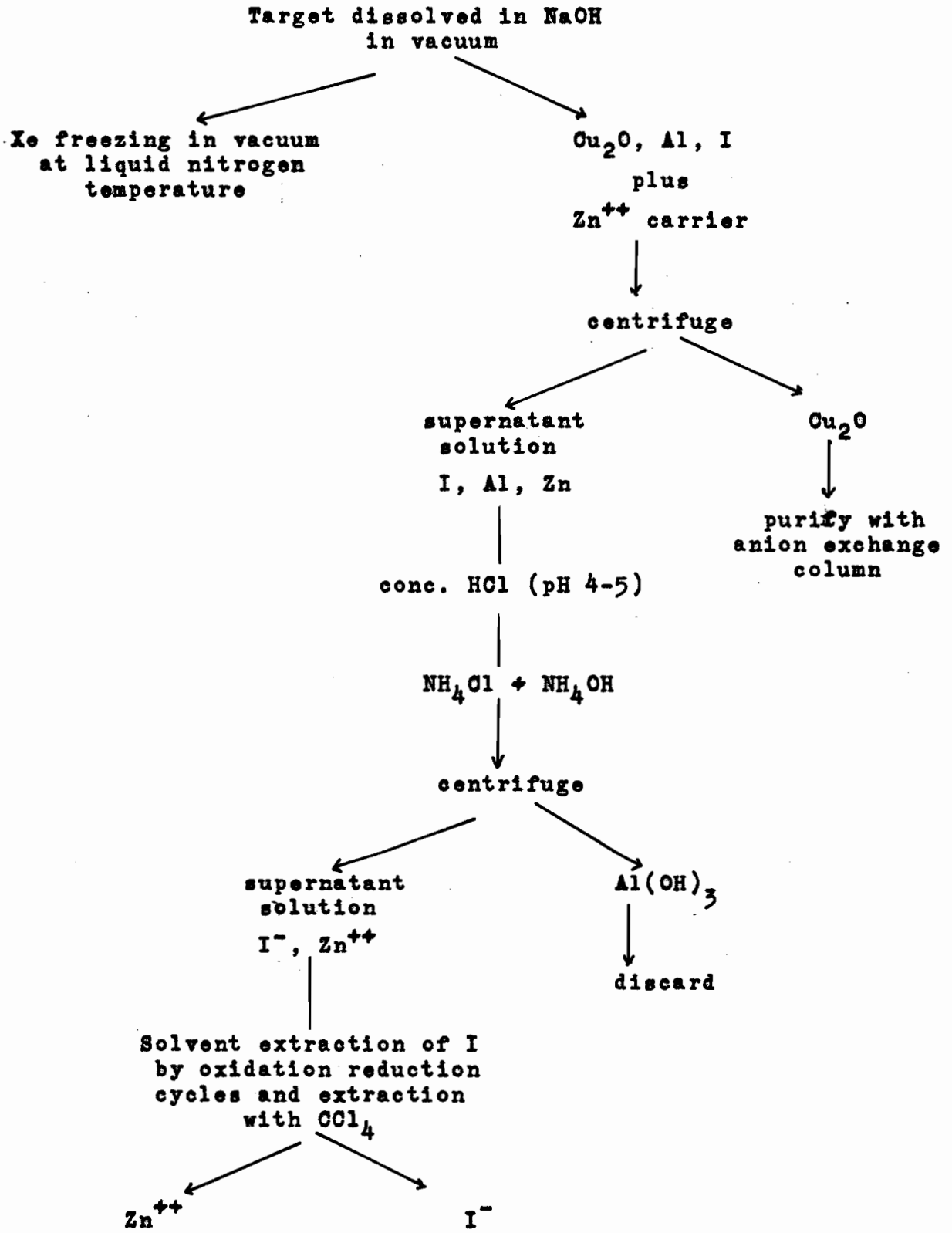

the attenuation of the proton beam, it was found that the cross sections for $I^{127}(p,n)Xe^{127}$ reaction obtained this way were in close agreement with those obtained by the method of CuI in the aluminum tubing. The results are shown in the next chapter.

(b) Most of the xenon formed in this way will remain inside the CuI crystal lattices. Xenon formed on the surface of CuI will not diffuse[145,146] through the aluminum tubing.

(c) The vapour pressure vs. temperature curve for xenon[152], as shown in Fig. 29, reveals that xenon will have a vapour pressure of only a few microns at liquid nitrogen temperature. Therefore the probability of losing xenon while pumping out hydrogen is very small.

5.4.2 Copper

The chemical yields of copper were determined colorimetrically with diethylthiocarbamate[153,154] using a Beckman model DU spectrophotometer. One cm pyrex cells were used. The standard curve used is shown in Fig. 30.

Chemical yields obtained were 40 to 70%, with an error of $\pm$ 2%.

5.4.3 Iodine

The chemical yields of iodine were also determined colorimetrically using the same instrument as described in Section 5.4.2.

Figure 29

VAPOUR PRESSURE OF XENON VS. TEMPERATURE

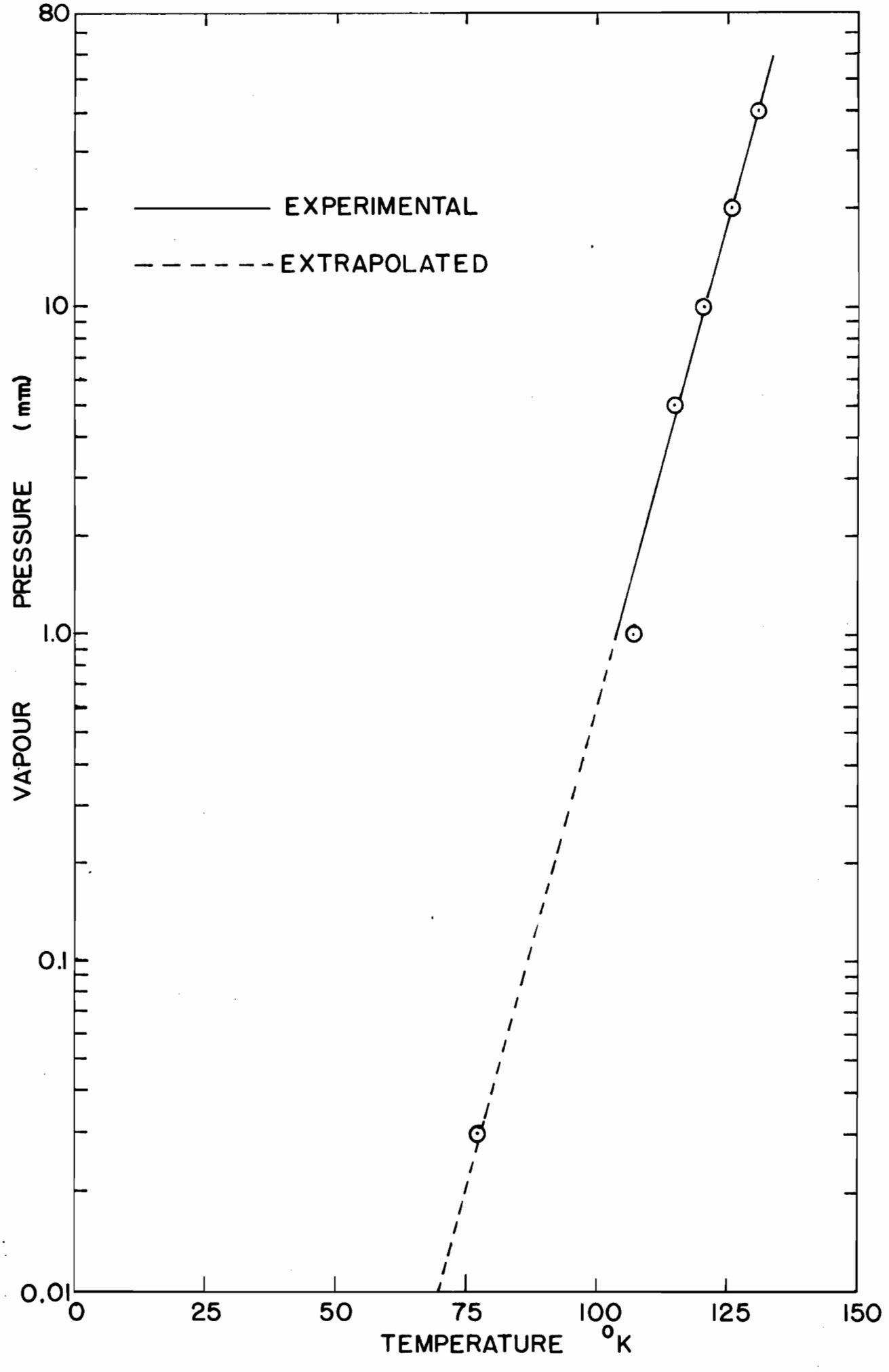
80
10
1.0
0.1
0.01
VAPOUR PRESSURE (mm)
EXPERIMENTAL
EXTRAPOLATED
0
25
50
75
100
125
150
TEMPERATURE °K

Figure 30

STANDARD ABSORBANCE CURVE FOR COPPER

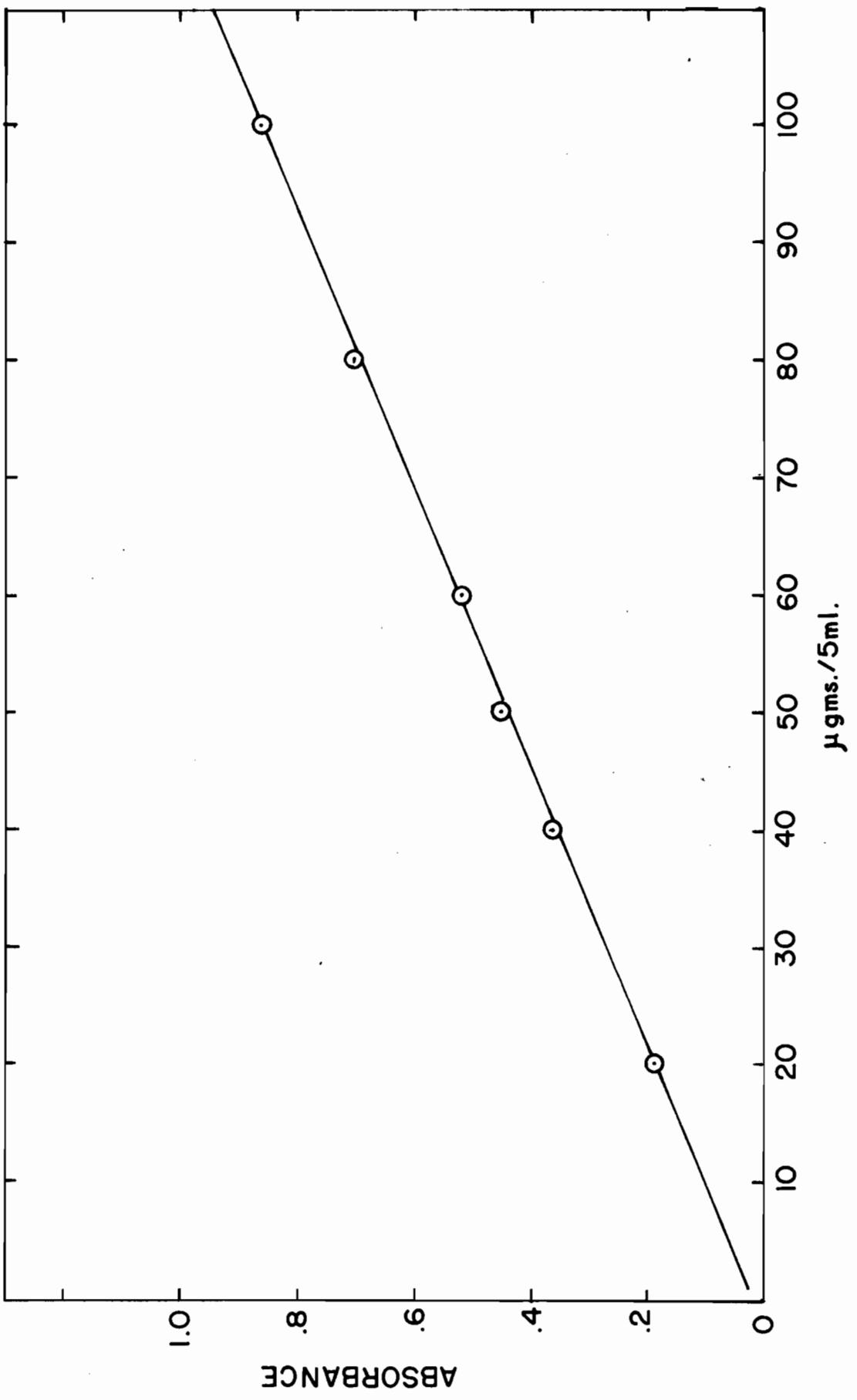
ABSORBANCE
0
.2
.4
.6
.8
1.0
10
20
30
40
50
60
70
80
90
100
µgms./5ml.

The method of Collins and Watkins[155] was used. It consisted in oxidizing the iodide ions to elementary iodine in aqueous medium and extracting it into the CCl_4 layer. The standard curve used is given in Fig. 31.

Chemical yields obtained were 53 - 93% with an error of ± 2%.

5.4.4 Zinc

The chemical yields of zinc were obtained by direct titration with EDTA, using Eriochrome black T indicator as described by Welcher[156].

Chemical yields obtained were 30 - 40% with an error of ± 3%.

5.5 MEASUREMENT TECHNIQUES

5.5.1 Radiation detection and measurement systems

A brief introduction to various radiation detection and measurement systems is presented in Section 1.4.

The product nuclides, formed by various (p,xn) and (p,pxn) reactions, decay primarily by orbital electron capture, and thus cross sections were determined by the absolute measurement of K X-rays and gamma rays. However, I^{126} is also a negatron emitter, therefore $4\pi\beta^-$ measurements[66,67,68,69,70] were also made in this case to get better statistics for the half-life of I^{126}.

Gamma-ray and X-ray measurements were done by scintillation spectrometry. The phosphor employed in this

Figure 31

STANDARD ABSORBANCE CURVE FOR IODINE

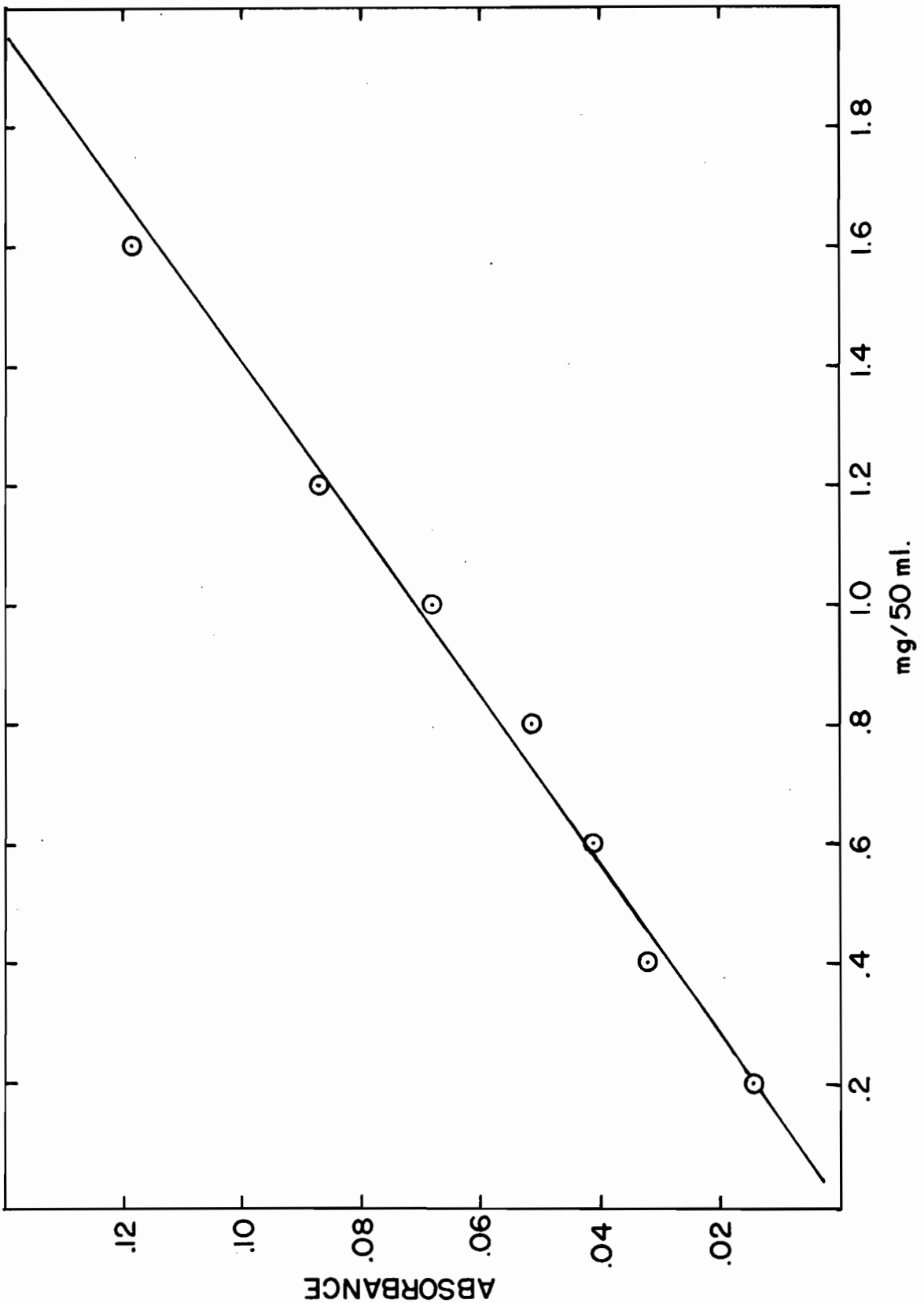
ABSORBANCE
.02
.04
.06
.08
.10
.12
.2
.4
.6
.8
1.0
1.2
1.4
1.6
1.8
mg/50 ml.

work was a commercially built (Harshaw Chemical Co., Cleveland, Ohio) type A, 3" x 3" hermetically sealed NaI(Tl) crystal. Details of the assembly are shown in Fig. 32.

The crystal was optically coupled[77] to a Dumont, type 6364, photomultiplier tube which was shielded by mu-metal from stray magnetic fields. In order to reduce the effect of background radiations, the entire assembly was shielded by a 1½" thick lead cylindrical wall. Fluorescent X-rays from the lead were attenuated by lining the lead shielding with ¼" of iron and 1/8" of lucite inside the iron. A stable high voltage was supplied to the photomultiplier tube by means of a commercially built (Baird-Atomic model 318) stabilized high voltage power supply.

The output of the photomultiplier tube was fed to a preamplifier (Hamner Electronics model N-351) and then to a non-overloading linear amplifier having variable gain (Baird-Atomic model 215). The output pulses from the linear amplifier, in turn, were fed into a commercially built 100-channel pulse height analyser (CDC model AEP 2230).

The 100 channel pulse height analyser had the following features:

(a) A magnetic core storage unit and oscilloscope for the visual representation of the data.

(b) An auxiliary external output for the recording of stored data by means of an analog signal from the pulse height analyser.

Figure 32

HARSHAW, TYPE A, 3" x 3" NaI(Tl)

CRYSTAL ASSEMBLY

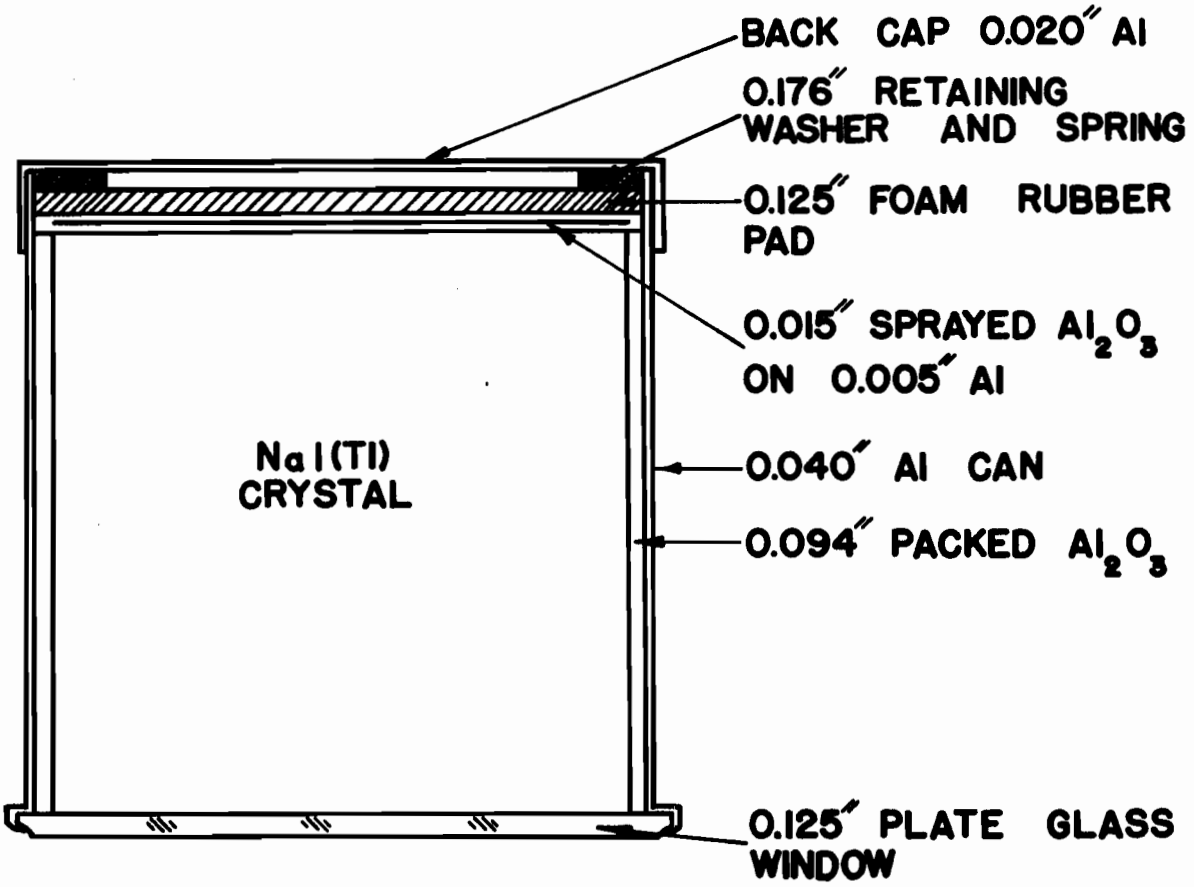
BACK CAP 0.020" Al
0.176" RETAINING WASHER AND SPRING
0.125" FOAM RUBBER PAD
0.015" SPRAYED Al_2O_3 ON 0.005" Al
NaI(Tl) CRYSTAL
0.040" Al CAN
0.094" PACKED Al_2O_3
0.125" PLATE GLASS WINDOW

(c) A digital print-out system comprising a decimal scaler, print control unit and printer.

(d) A microammeter, which indicated the percentage losses due to dead-time (35 μ secs to 135 μ secs) depending upon the pulse height.

(e) An arrangement to recover the stored information manually in case of failure of the recording and printing unit.

In general, the spectrum was not distorted by dead-time losses, but its overall amplitude was reduced. The sources could be measured at desired distances from the crystal, as shown in Fig. 33, so that the dead-time loss could be kept minimal to achieve a small dead-time correction. The dead-time loss was kept at less than 10% by adjusting the source height. A block diagram of the entire measuring system is shown in Fig. 34.

5.5.2 Analysis of spectra

When electromagnetic radiation (e.g. X-rays and gamma rays) of intensity 'I_o' is incident on a matter of thickness 'd', it emerges with the intensity 'I' as represented by the relation

$$\frac{I}{I_o} = \exp(-\mu d) \quad \ldots\ldots\ldots\ldots\ldots (17)$$

The parameter μ is known as the total linear absorption coefficient, and this in turn is given by the following

Figure 33

NaI(Tl) DETECTOR, PHOTOMULTIPLIER TUBE

AND SHIELDING

SHELF NUMBER	HEIGHT ABOVE Al CAN (CM.)
10	17.80
8	11.10
7	8.57
6	5.98
5	4.71
4	3.47
3	2.66
2	1.85
1	0.95

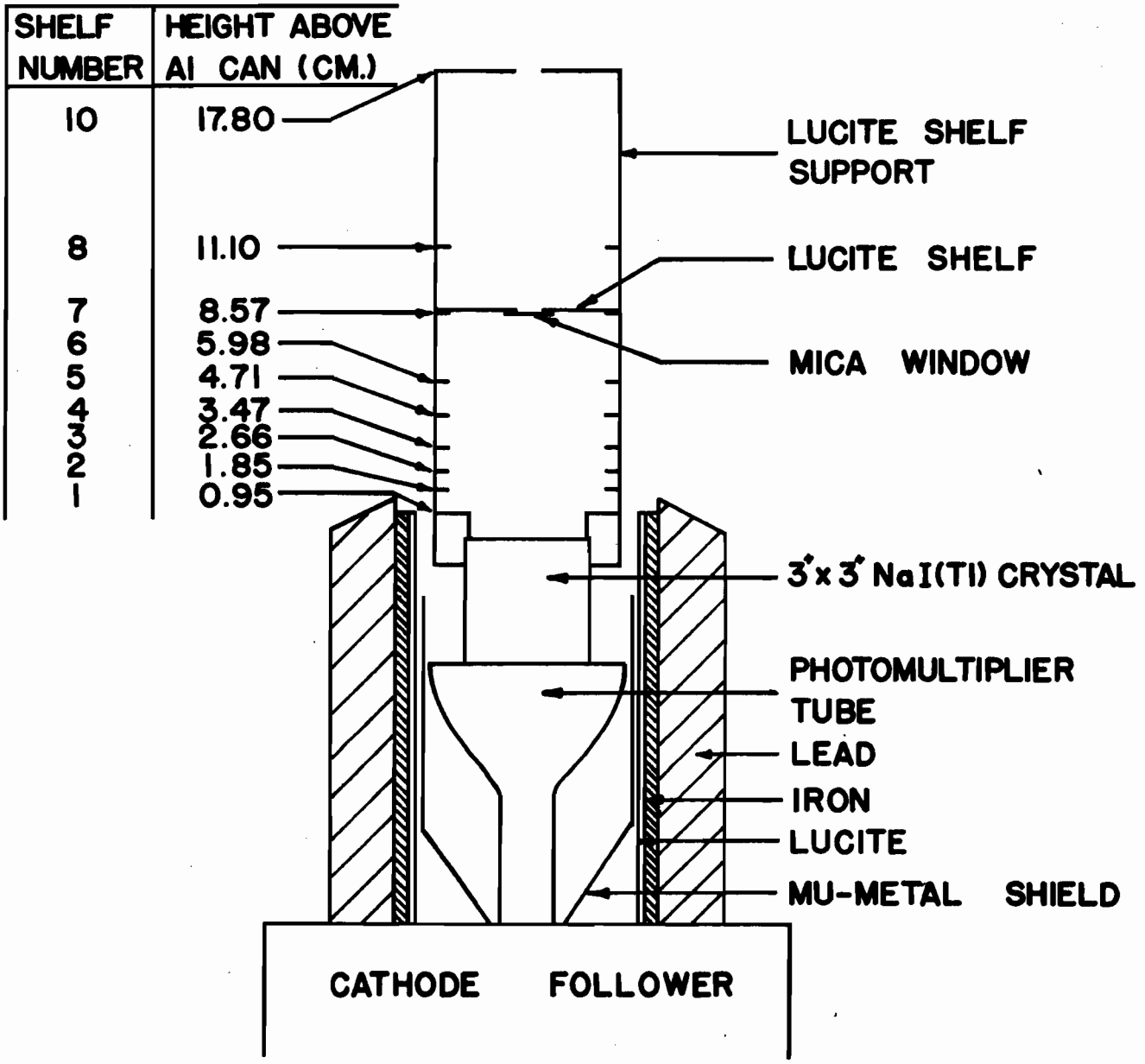

Figure 34

BLOCK DIAGRAM OF 100-CHANNEL PULSE HEIGHT ANALYSER AND AUXILIARY UNITS

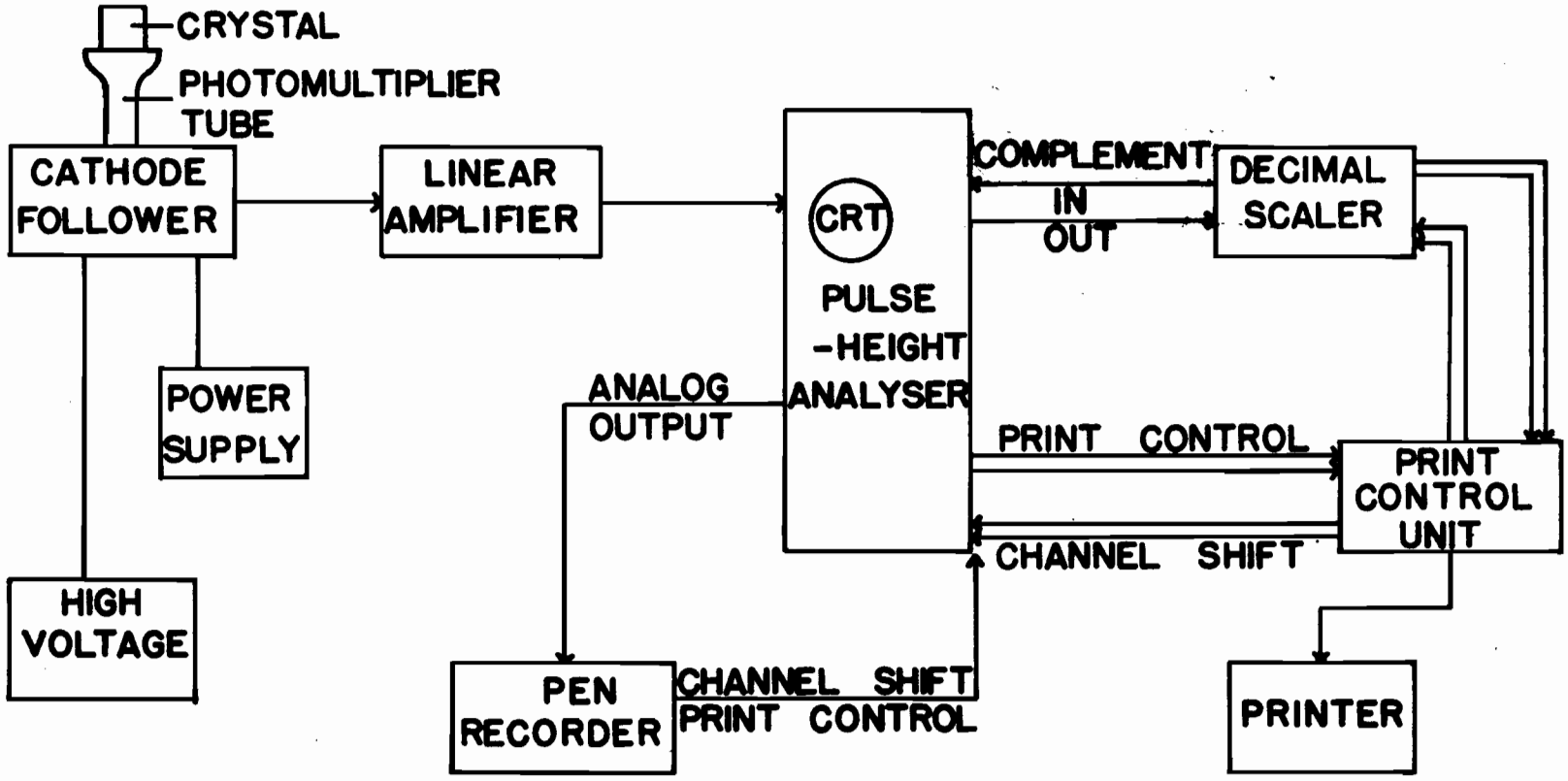
CRYSTAL
PHOTOMULTIPLIER TUBE
CATHODE FOLLOWER
LINEAR AMPLIFIER
CRT
PULSE -HEIGHT ANALYSER
COMPLEMENT
IN
OUT
DECIMAL SCALER
POWER SUPPLY
ANALOG OUTPUT
PRINT CONTROL
PRINT CONTROL UNIT
CHANNEL SHIFT
HIGH VOLTAGE
PEN RECORDER
CHANNEL SHIFT
PRINT CONTROL
PRINTER

expression

$$\mu = T + \sigma + k \quad \ldots\ldots\ldots\ldots\ldots\ldots (18)$$

where T, σ and k represent the partial absorption coefficients due to the photo-electric effect, Compton effect, and pair production respectively. The interaction of a gamma-ray or X-ray photon with a NaI crystal will be considered as a specific example.

When a gamma-ray photon with energy $h\nu$ passes through a NaI crystal, the energy loss of the photon can be accounted for in the following ways:

(a) Photoelectric effect:

When a photon with an energy $h\nu$ interacts with a bound electron in an atom, it may transfer all of its energy to the electron. This phenomenon is known as the photo-electric effect. The kinetic energy of the emitted electron will be $(h\nu - B)$ where B is the binding energy of the electron in the atom. The energy $(h\nu - B)$ is absorbed by phosphor (NaI in this case) and its re-emission as visible or in near visible radiation is known as luminescence and, if luminescence occurs during the excitation or within 10^{-8} secs after it, the material is said to be fluorescent[29].

In the NaI(Tl) crystal, the fluorescent light output is proportional to the energy absorbed by the crystal from the incident photon. If the photoelectron produced by the photo-electric absorption is stopped within the crystal, and the

X-rays resulting from the de-excitation of the atom in which the photoelectric event occurs are also stopped within the crystal, then the full energy of the incident photon contributes to the total light output of the crystal. Such a 'total energy' event will give rise to a narrow distribution of pulse heights corresponding to the incident photons. This peak in the pulse height distribution is called the 'photopeak'.

(b) Compton scattering:

When a gamma-ray photon interacts with an electron, its energy may only be shared by the electron, and the direction as well as the energy of the photon will be changed.

The essential difference between the photoelectric effect and Compton effect is that in the former case the photon is absorbed, while in the latter case only its energy is changed. The secondary photon may undergo a further Compton scattering, photoelectric absorption or pair production, or may even escape from the crystal. If it escapes, the result will be a pulse having a height less than that corresponding to 'total energy absorption' in the crystal.

There is an upper limit to the energy which can be transferred to an electron in the Compton process for a given incident photon energy. This corresponds to a 'head-on' collision with the free electron and the secondary photon scattered backwards. If this secondary photon escapes from the crystal, the resulting pulse has a height corresponding to

the 'Compton edge'. Photons scattered at other angles, and also escaping from the crystal, will give a continuous spread in pulse heights below the Compton edge.

(c) Pair production

When the energy of a gamma ray exceeds 1.02 Mev, i.e. greater than two electron masses (2 x 0.51 Mev), it may be totally converted into a positron and an electron, and the energy in excess of 1.02 Mev would be shared by an electron and a positron. The positron would have a greater share of the energy due to the repulsion from the nucleus. The positron in turn would get annihilated with another electron in the NaI crystal, giving rise to two 0.511 Mev photons, which may or may not escape from the crystal.

An ideal picture of a pulse height distribution for a mono-energetic gamma ray of energy 1.02 Mev is shown in Fig. 35(A), illustrating the different features of the pulse height spectrum which would be observed with a NaI crystal having 'ideal' resolution. The actual pulse height distribution is typified by Fig. 35(B), in which the effect of finite resolution of the crystal can be seen.

The photopeak is nearly Gaussian in shape and the resolution of the system is usually defined as the full width of the photopeak at half maximum. The resolution of the instrument [NaI(Tl) crystal assembly] used in the present work was found to be 12.5% at 662 kev.

Figure 35 (A and B)

PULSE HEIGHT DISTRIBUTION DUE TO PHOTOELECTRIC, COMPTON SCATTERING AND PAIR PRODUCTION

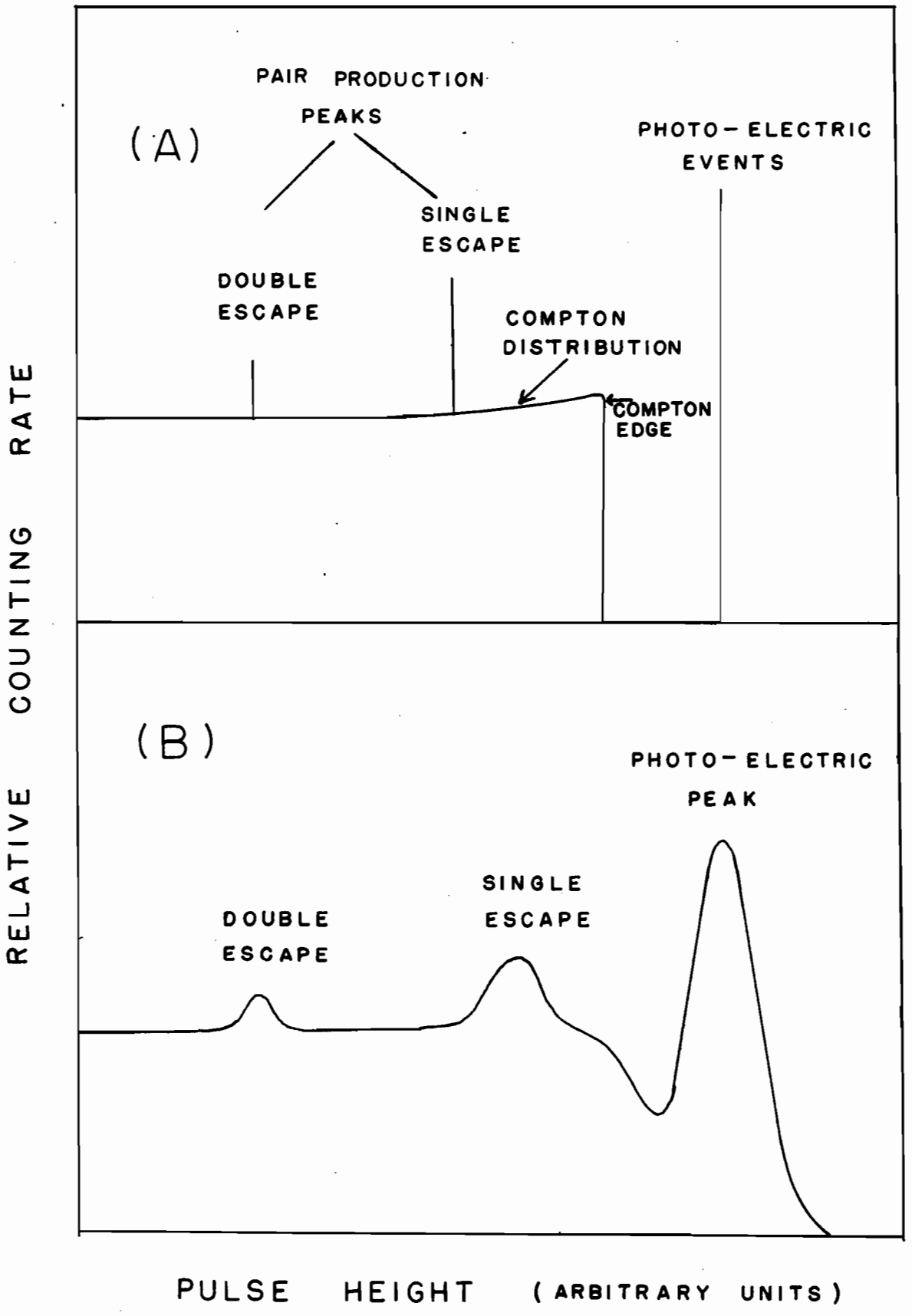
(A)
PAIR PRODUCTION PEAKS
PHOTO-ELECTRIC EVENTS
SINGLE ESCAPE
DOUBLE ESCAPE
COMPTON DISTRIBUTION
COMPTON EDGE
(B)
PHOTO-ELECTRIC PEAK
SINGLE ESCAPE
DOUBLE ESCAPE
RELATIVE COUNTING RATE
PULSE HEIGHT (ARBITRARY UNITS)

5.5.3 Conversion of peak areas into count rates

In order to convert the areas under the photopeaks to the gamma-ray or X-ray intensities, a knowledge of the photopeak efficiency is necessary. The photopeak efficiency is defined as the probability of the gamma-ray or X-ray causing a pulse to fall in the full energy peak for a particular geometrical arrangement of source and detector.

In this Laboratory, G.R. Grant, G.V.S. Rayudu, and M. May[157] experimentally determined the photopeak efficiencies, and these efficiency curves were used in the present calculations.

The area under the peak was obtained from the pulse height analyser by subtracting the average background counts from all the channels under the peak from the total number of counts in each channel and adding the resultant number of counts for all the channels in the photopeak. This procedure is justified because the plot of the background counts vs. energy under the photopeak is close to a straight line.

5.5.4 Conversion of gamma-ray emission rate to absolute disintegration rate

The absolute disintegration rates from the observed gamma-ray photon count rates were calculated from the following expression:

$$D_x^o = \frac{C.R\gamma \times y \times (1 + \alpha_T)}{\text{eff.} \times \text{B.R.}} \quad \ldots\ldots\ldots\ldots (19)$$

where D_x^o = the absolute disintegration rate of the nuclide under observation at the end of bombardment.

C.Rγ = the observed count rate at the end of bombardment.

y = the chemical yield correction, including the dilution factor.

α_T = the internal conversion coefficient.

B.R. = the branching ratio.

eff. = the photopeak efficiency of the gamma ray under consideration.

The values of the branching ratio (B.R.) and internal conversion coefficient (α_T) were taken from the Nuclear Data Sheets[54] and Tables of Isotopes[158].

5.5.5 Conversion of K X-ray emission rates to absolute disintegration rates

The absolute disintegration rates were calculated from the observed K X-ray count rates (it was presumed that all the observed X-rays originated from the K-shell) by using the following expression:

$$D_x^o = C.R_k \times y \times (eff)^{-1}\left[(f.\omega_k)\left(1-\frac{\alpha_k \omega_k}{1+\alpha_T}\right)+\left(\frac{\alpha_k \omega_k}{1+\alpha_T}\right)(1-f.\omega_k.eff)\right]^{-1} \quad (20)$$

where $C.R_k$ is the observed K X-ray count rate at the end of the bombardment. y and 'eff' are as defined in Section 5.5.4. ω_k is the K fluorescence yield, defined as the number of K X-ray quanta emitted per vacancy in the K-shell. f is the ratio of K-electron capture to the total electron capture

$$\text{i.e. } f = \frac{\epsilon_k}{\epsilon_k + \epsilon_L + \epsilon_M \text{ ---}}$$

where α_k is the K-electron conversion coefficient and α_T the total internal conversion coefficient.

Expression (20) can also be written as

$$D_x^o = \frac{C.R_k \times y \times I.C.}{\text{eff} \times \omega_k \times f} \quad \text{..... (20a)}$$

where I.C. is the internal conversion X-ray correction. This correction arises from the fact that an emitted gamma ray, during electron capture decay, may get internally converted, resulting in the emission of a characteristic K X-ray which will also contribute to K X-ray photopeak.

The values of the constant parameters used in expression (20) were taken from standard sources[54,158,159]. The value of ω_k for iodine was taken from Broyles et al.[160].

5.6 CROSS-SECTION DETERMINATIONS

The absolute values of cross sections of the product nuclides were calculated from the following expression:

$$\sigma_x = \sigma_m \frac{N.A_m}{N.A_\tau} \cdot \frac{A.W_\tau}{A.W_m} \cdot \frac{W_m}{W_\tau} \cdot \frac{D_x^o}{D_m^o} \cdot \frac{(1 - e^{-\lambda_m t})}{(1 - e^{-\lambda_x t})} \quad \text{..... (21)}$$

where $N.A_m$ = natural abundance of the monitor.

$N.A_\tau$ = natural abundance of the target.

$A.W_\tau$ = atomic weight of the target.

$A.W_m$ = atomic weight of the monitor

W_m = weight of the monitor.

W_τ = weight of the target

D_x° = absolute disintegration rate of the product nuclide at end of bombardment.

D_m° = absolute disintegration rate of the monitor nuclide at end of bombardment.

λ_m = the decay constant of monitor nuclide.

λ_x = the decay constant of the product nuclide, x.

$\bar{\sigma}_x$ = the absolute cross section of the product nuclide, x.

$\bar{\sigma}_m$ = the absolute cross section of the chosen monitor reaction.

t = the irradiation time.

All the factors on the right-hand side of expression (21) were known. The values for D_x°, D_m°, λ_m, λ_x, t, W_m, and W_τ were obtained experimentally, and the values for $N.A_m$, $N.A_\tau$, $A.W_m$, and $A.W_\tau$ were taken from Nuclear Data Sheets[54]. The values for $\bar{\sigma}_m$, as obtained by Ghoshal[148] and Meghir[149], were used, and these values are listed in Table VII.

Table VII

CROSS-SECTION VALUES USED FOR MONITOR REACTIONS

Proton Beam Energy (Mev)	$\sigma\ Cu^{63}(p,n)Zn^{63}$ (148) (mb)	$\sigma\ Cu^{65}(p,pn)Cu^{64}$ (149) (mb)
7	197.5	-
11	487.5	-
16	-	100
21	-	356
27	-	344
35	-	294
42	-	260
49	-	232
56	-	208
63	-	186
70	-	161
80	-	140
86	-	128

5.7 STATISTICAL ACCURACY OF THE OBSERVED CROSS SECTIONS

The principal sources of errors in determining the absolute cross sections for $I^{127}(p,xn)$ and $I^{127}(p,pxn)$ reactions were the following:

(a) As the target and the monitor form a stable chemical compound (CuI) their masses always will be in the ratio of their atomic masses. Consequently there would be no substantial error in weighing.

(b) An error resulting from incomplete exchange between the radioiodine and carrier atoms (inactive iodine atoms) will be negligibly small, since three oxidation and reduction cycles were performed for purification, as well as complete exchange.

(c) An error of 2 - 3% was estimated in the determination of chemical yields of various products.

(d) In the analysis of decay curves, an error of 10% was estimated. This value included the best values for the half-lives.

(e) An error of 5% was estimated in the case of calculating the photopeak efficiencies.

(f) In the case of monitor cross sections, $\bar{\sigma}_m$, an error of 5% was estimated while reading the absolute values from excitation functions.

$$\text{If} \quad \sigma_x = k\,\sigma_m \frac{D_x^\circ}{D_m^\circ} \cdot \frac{(1 - e^{-\lambda_m t})}{(1 - e^{-\lambda_x t})} \qquad \ldots\ldots\ldots\ldots (22)$$

$$\text{where} \quad k = \frac{N.A_m}{N.A_\tau} \cdot \frac{A.W_\tau}{A.W_m} \cdot \frac{W_m}{W_\tau} = \text{constant},$$

then the relative error in σ_x, in terms of the relative errors in σ_m, D_x°, D_m°, λ_m, λ_x, is given by

$$\frac{\Delta\sigma_x}{\sigma_x} = \frac{\Delta\sigma_m}{\sigma_m} + \frac{\Delta D_x^\circ}{D_x^\circ} - \frac{\Delta D_m^\circ}{D_m^\circ} + \frac{\Delta\lambda_m t.e^{-\lambda_m t}}{(1 - e^{-\lambda_m t})(1 - e^{-\lambda_x t})} - \frac{t.e^{-\lambda_x t}}{(1 - e^{-\lambda_x t})} \cdot \Delta\lambda_x \quad \ldots\ldots(23)$$

For $\lambda_m t \ll 1$ and $\lambda_x t \ll 1$, the expression (23) reduces to

$$\frac{\Delta\sigma_x}{\sigma_x} = \frac{\Delta\sigma_m}{\sigma_m} + \frac{\Delta D_x^\circ}{D_x^\circ} - \frac{\Delta D_m^\circ}{D_m^\circ} + \frac{\Delta\lambda_m}{\lambda_m} - \frac{\Delta\lambda_x}{\lambda_x} \qquad \ldots\ldots\ldots (24)$$

Thus, by inserting the estimated errors in equation (24), it was found that the present results are good to $\pm$ 20%.

6. RESULTS AND DISCUSSION

6.1 IDENTIFICATION OF THE PRODUCT NUCLIDES AND DETERMINATION OF CROSS SECTIONS OF NUCLEAR REACTIONS

The product nuclides formed by the various (p,xn) and (p,pxn) reactions decay primarily by orbital electron capture. Cross sections were determined by absolute measurements of K X-rays and gamma rays that follow the decay events. Each radioactive nuclide measured was identified by its characteristic half-life, gamma energies, and relative abundance. Gamma rays and X-rays observed and identified in the present work are illustrated in Table VIII. All the individual cases are discussed in Sections 6.1.1 to 6.1.6.

The half-lives found in this work are shown in Table VIII. The error quoted is the standard deviation.

The nuclear data used in the calculations of cross sections and disintegration rates are illustrated in Table VIII(A).

6.1.1 Monitor reactions

$[Cu^{63}(p,n)Zn^{63}, Cu^{65}(p,pn)Cu^{64}]$

The product nucleus Zn^{63} decays to Cu^{63} (stable) by electron capture and positron emission, while Cu^{64} decays to Zn^{64} by an additional mode of decay, i.e. negatron emission.

The Zn^{63} and Cu^{64} were identified from the total

Table VIII

Nuclide	Gamma rays and K X-rays observed	Duration of measurement (in half-lives)	Half-life	
			Present work	Literature values
Xe^{127}	(170 + 204) kev 377 kev	3 to 4	36.8 ± 1.4 d.	36.406 d.[161]
I^{126}	K X-rays 386 kev, 480 kev, 650 kev	4	13.3 ± 0.3 d.	13.1 d.[140] 13.3 d.[162]
I^{125}	K X-rays	3	59.0 ± 2.1 d.	60.0 d.[141]
I^{124}	K X-rays	4 to 6	4.34 ± 0.03 d.	4.2 d.[163] 3.4 d.[140]
I^{123}	K X-rays 159 kev	4 to 5	13.7 ± 0.3 h.	13 h.[139]

Table VIII(A)

Nuclide	Half-life	Gamma-ray Energy kev	K X-ray energy kev	B.R.	α_T	ω_k
Xe^{127}	36.8 d.*	377	-	0.21(54)	0.014**	-
I^{126}	13.3 d.*	386	-	0.34(54)	0.018**	-
I^{125}	59.0 d.*	-	28	-	13.2**	0.88(160)
I^{124}	4.34 d.*	-	28	-	0.18**	0.88(160)
I^{123}	13.7 h.*	159	-	0.99(54)	0.329**	-
Zn^{63}	38.5 m.*	511	-	0.93(54)	-	-
Cu^{64}	12.8 h.*	511	-	0.19(54)	-	-

*Experimentally observed values

**Computed from references (54,158,159)

photopeak counting rates of the 511 kev gamma ray resulting from the annihilation of the positrons. Typical decay curves of Zn^{63} and Cu^{64} are shown in Figs. 36 and 36(A) respectively. The values of the half-lives obtained in this work were 38.5 minutes and 12.8 hours for Zn^{63} and Cu^{64} respectively. These values are in close agreement with those reported recently in the literature[157,154]. In the case of Cu^{64} activity measurements, these were made about 12 hours after the bombardment to allow sufficient time for the 3.3 hr. Cu^{61} activity to decay.

6.1.2 $I^{127}(p,n)Xe^{127}$

The half-life, as well as the cross section for formation of the product nucleus Xe^{127}, was determined from the decay of the 377 kev gamma ray that follows the electron capture events. Thirteen samples collected at different energies were followed for half-life determination. The value thus obtained was 36.8 $\pm$ 1.4 days. This value is in close agreement with the recently reported value of 36.406 days by Balestrini[161]. Figure 37 gives the decay curve of Xe^{127}.

The cross sections of the product nucleus, Xe^{127}, were calculated as described in Section 5.6. An example of such calculation is illustrated below.

Figure 36

DECAY CURVE OF THE 511 KEV

PEAK HEIGHT OF Zn^{63}

(Bombarding energy 11 Mev)

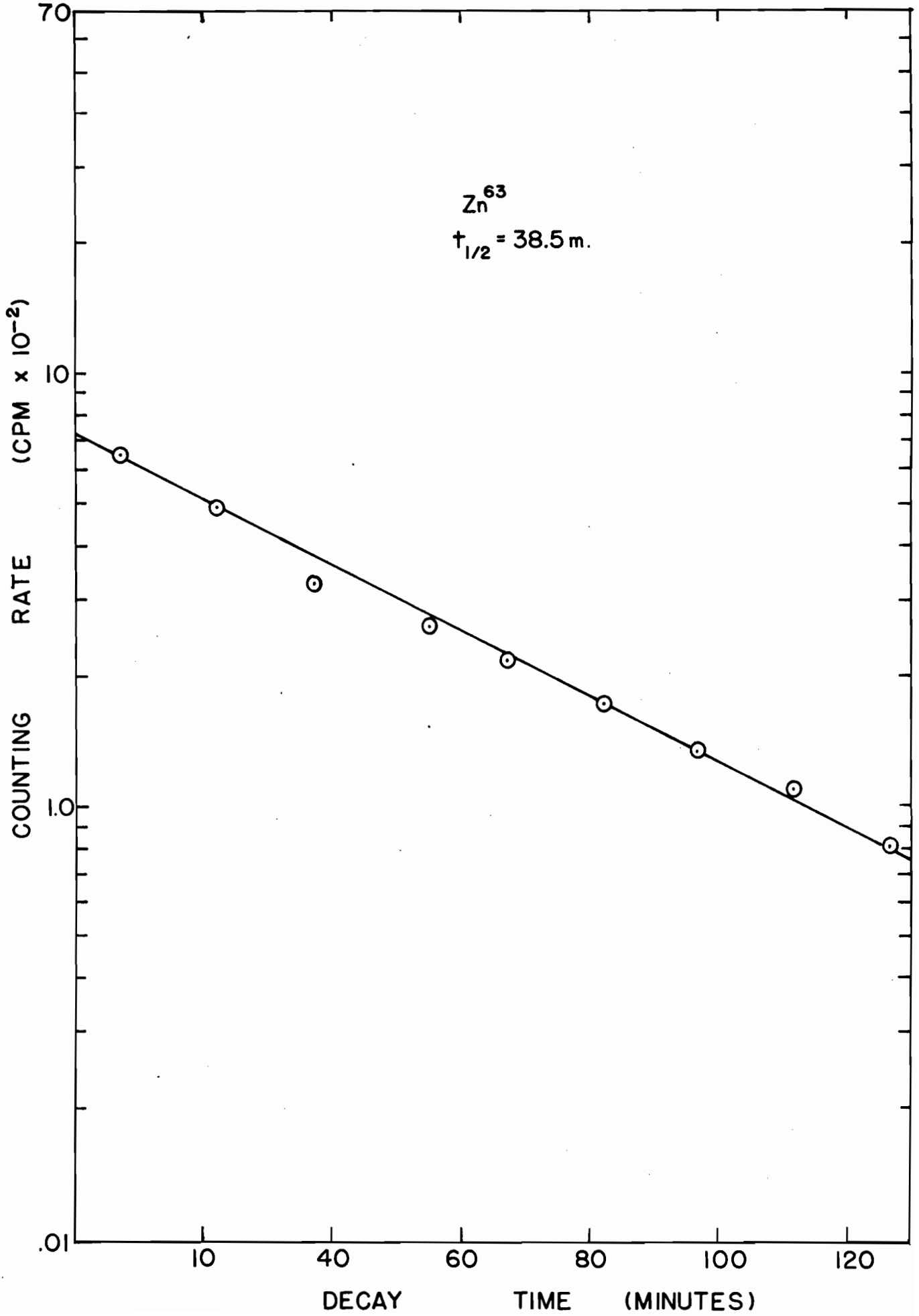
70
10
1.0
.01
COUNTING RATE (CPM x 10^{-2})
Zn^{63}
$t_{1/2}$ = 38.5 m.
10
40
60
80
100
120
DECAY TIME (MINUTES)

Figure 36(A)

DECAY CURVE OF THE 511 KEV

PEAK HEIGHT OF Cu^{64}

(Bombarding energy 21 Mev)

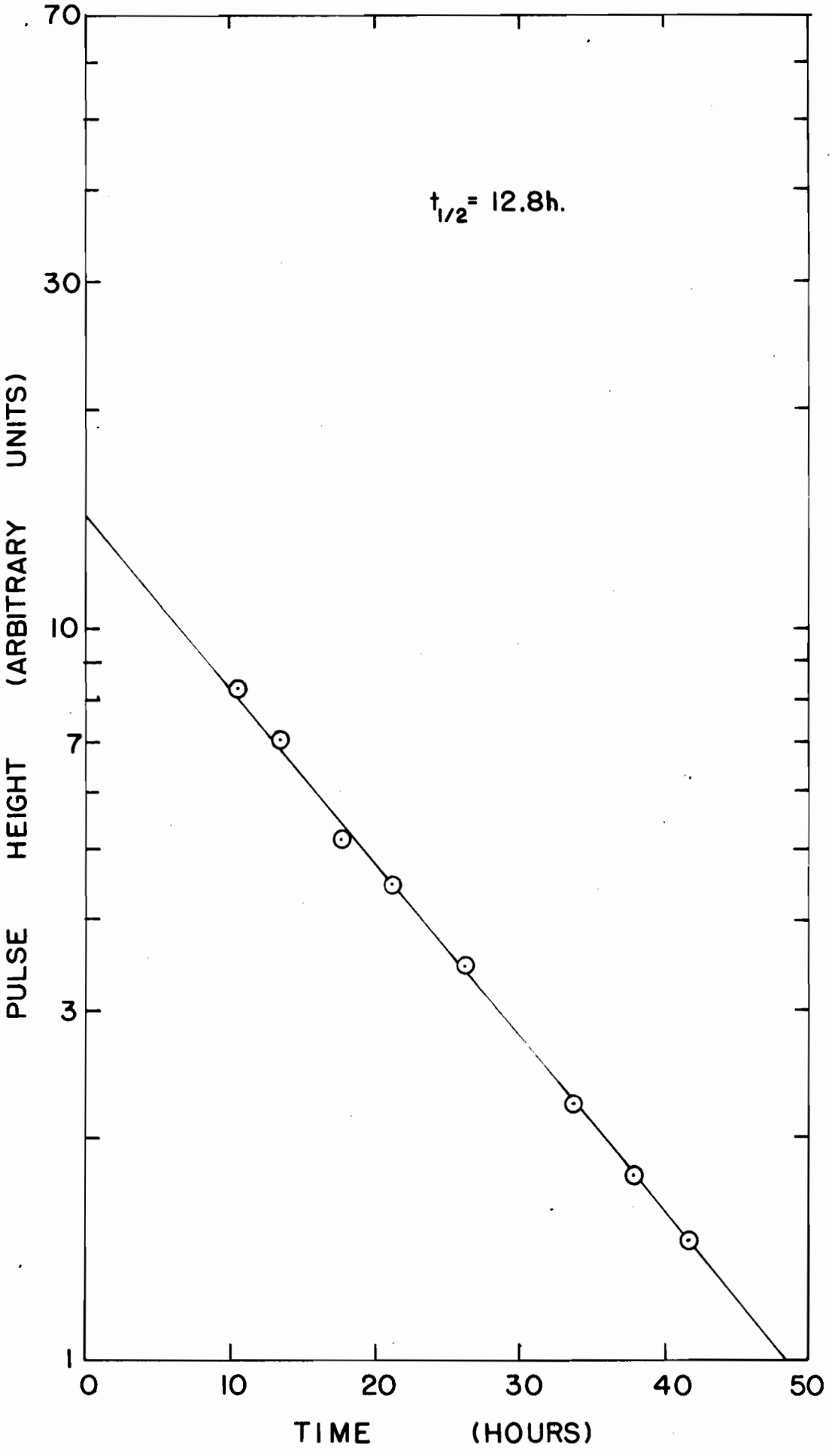
70
30
10
7
3
1
$t_{1/2}$= 12.8h.
PULSE HEIGHT (ARBITRARY UNITS)
0
10
20
30
40
50
TIME (HOURS)

Figure 37

DECAY CURVE OF THE 377 KEV

PEAK HEIGHT OF Xe^{127}

(Bombarding energy 45 Mev)

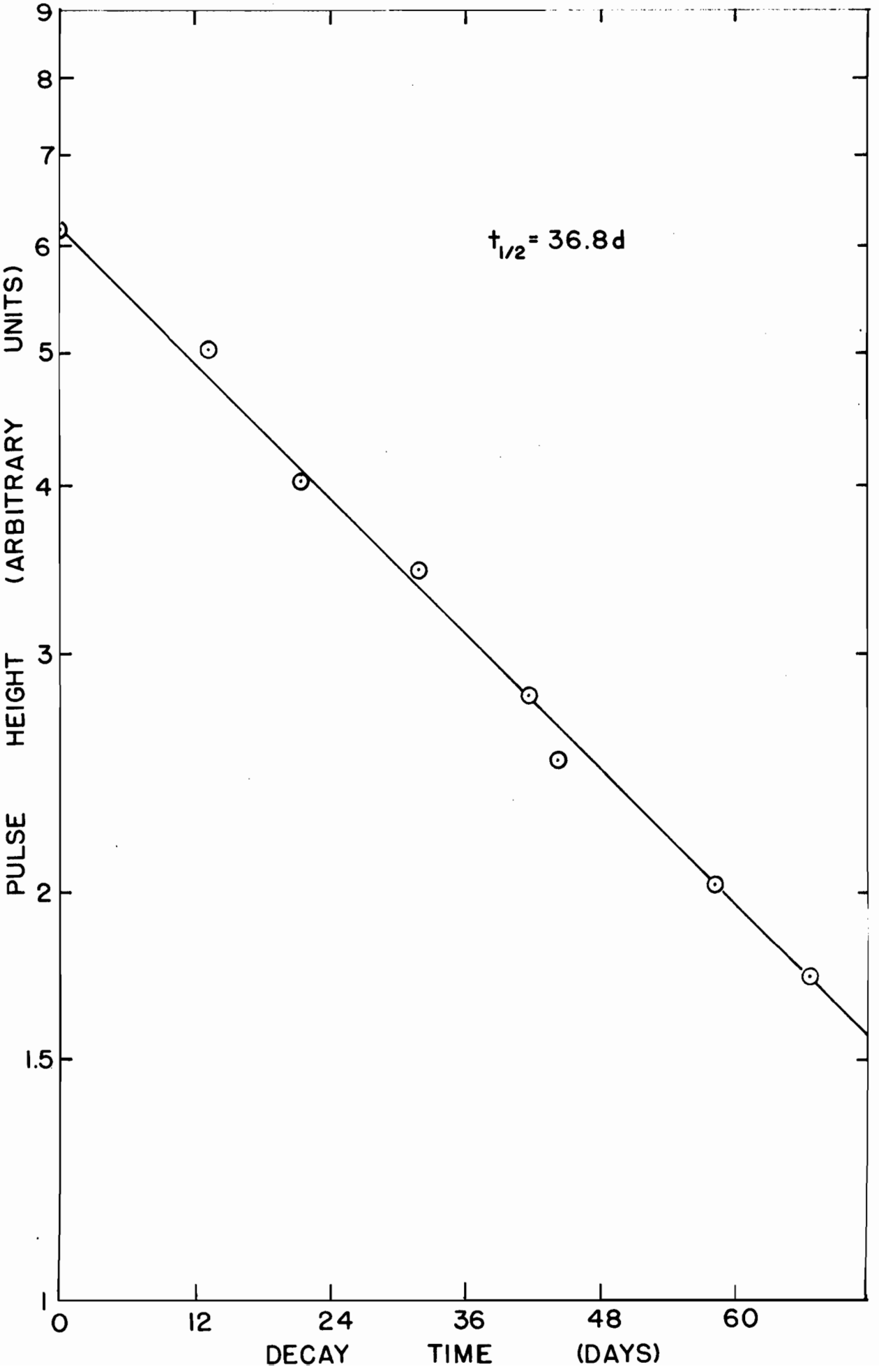
9
8
7
6
5
4
3
2
1.5
1
PULSE HEIGHT (ARBITRARY UNITS)
$t_{1/2}$ = 36.8d
0
12
24
36
48
60
DECAY TIME (DAYS)

To calculate the cross section of the $I^{127}(p,n)Xe^{127}$ reaction for 7 Mev protons:

Step 1 : Absolute disintegration rate of Zn^{63} (monitor)

The absolute disintegration rate of the monitor reaction at the end of bombardment is given by the expression

$$D_m^o = C.R \times y \times \frac{1}{2\ B.R_{\beta+}} \quad \ldots\ldots\ldots\ldots\ldots\ldots (25)$$

$C.R = 6.895 \times 10^6$ cpm (found experimentally)

$B.R_{\beta+} = 93\%$ (54)

$y = \frac{\text{dilution}}{\text{yield}} = \frac{12.5}{0.569}$ (found experimentally)

These values were substituted in the above expression (25) and the absolute disintegration rate was found to be 8.143×10^7 dpm.

Step 2 : Absolute disintegration rate of Xe^{127} (product)

The absolute disintegration rate of Xe^{127} at the end of bombardment is given by the following expression. (For explanation, see Section 5.5.4.)

$$D^{\circ}_{Xe^{127}} = C.R \times y \times \frac{1 + \alpha_T}{B.R} \quad \ldots\ldots\ldots\ldots\ldots\ldots (26)$$

$C.R = 2.014 \times 10^3$ (found experimentally)

$y = 1$ (presumed)

$\alpha_T = 0.014$ (54)

$B.R = 21\%$

These values were substituted in the above expression (26) and the absolute disintegration rate of Xe^{127} at the end of bombardment was found to be 9.075×10^3 dpm.

Step 3 : Calculation of saturation factors

(For explanation of symbols see Section 5.6)

$\frac{1 - e^{-\lambda_m t}}{}$

$t = 2.4 \times 10^3$ secs.

$\lambda_m = 3.0399 \times 10^{-4}$ sec^{-1}

Therefore $1 - e^{-\lambda_m t} = 0.5179$.

$\frac{1 - e^{-\lambda_x t}}{}$

$t = 2.4 \times 10^3$ secs.

$\lambda_{Xe^{127}} = 2.178 \times 10^{-7}$ sec^{-1}

Therefore $1 - e^{-\lambda_x t} = 0.0005$.

Step 4 : Cross-section calculation

The expression for the cross-section determination as explained in Section 5.6 is:

$$\frac{\sigma_x}{\sigma_m} = \frac{D_x^o}{D_m^o} \cdot \frac{W_m}{W_\tau} \cdot \frac{N.A_m}{N.A_\tau} \cdot \frac{A.W_\tau}{A.W_m} \cdot \frac{(1 - e^{-\lambda_m t})}{(1 - e^{-\lambda_x t})} \quad \ldots\ldots (27)$$

In the case of CuI, the term W_m/W_τ will always be proportional to $A.W_m/A.W_\tau$ i.e. it will be independent of the weight of CuI taken. Thus for CuI, expression (27) reduces to

$$\frac{\sigma_x}{\sigma_m} = \frac{D_x^o}{D_m^o} \cdot \frac{N.A_m}{N.A_\tau} \cdot \frac{(1 - e^{-\lambda_m t})}{(1 - e^{-\lambda_x t})} \quad \ldots\ldots\ldots\ldots (28)$$

Now

$\sigma_m = 197.5$ (Table VII)

$N.A_{Cu^{63}} = 69.09\%$ (54)

$N.A_{I^{127}} = 100\%$ (54)

When these values were substituted in (28) the cross section of $I^{127}(p,n)Xe^{127}$ reaction came out

$= 16.8$ mb.

≈ 17 mb.

The statistical accuracy of this value is $\pm$ 20% (Section 5.7).

Therefore $\sigma_{I^{127}(p,n)Xe^{127}}$ for 7 Mev protons = 17 ± 3 mb.

The cross sections of (p,n) reactions reported in this work are the total cross section of Xe^{127m} (75 sec) and Xe^{127} (36.8 d). The absolute values of the cross sections are listed in Table IX and the excitation function of the $I^{127}(p,n)Xe^{127}$ reaction is illustrated in Fig. 38. The outlines of the calculation are shown in Table X.

Table IX

ABSOLUTE CROSS SECTIONS FOR $I^{127}(p,n)Xe^{127}$ AND $I^{127}(p,pxn)$ REACTIONS OBTAINED IN THIS WORK

Bomb. No.	Energy of Proton Beam Mev.	σ $I^{127}(p,n)Xe^{127}$ mb	σ $I^{127}(p,pn)I^{126}$ mb	σ $I^{127}(p,p2n)I^{125}$ mb	σ $I^{127}(p,p3n)I^{124}$ mb	σ $I^{127}(p,p4n)I^{123}$ mb
1	7	16.8 ± 3.4				
2	11	245 ± 49				
4	16	425 ± 85				
5	21	23.9 ± 4.8	41 ± 8.2			
6	27	6.1 ± 1.2	41.9 ± 8.4	8.2 ± 1.6		
7	35	4.7 ± 1	59.8 ± 11.9	23.8 ± 4.8		
8	42	8.7 ± 1.7	90.9 ± 18.2	66.6 ± 13.3	6.3 ± 1.3	
9	49	8.1 ± 1.6	95.8 ± 19.2	72.2 ± 14.4	27.3 ± 5.5	14.4 ± 2.9*
10	56	9.6 ± 1.9	83.5 ± 16.6	96.8 ± 19.4		182 ± 36.5*
11	63	5 ± 1	109 ± 21.8	87.5 ± 17.5	49.1 ± 9.8	235 ± 46.9*
13	70			66.2 ± 13.2	42.1 ± 8.4	188 ± 37.6*
14	80		52 ± 10.4	47.5 ± 9.6	24.1 ± 4.8	130 ± 26*
20**	45	7.7 ± 1.5				

*These are not absolute values.

**This bombardment was done with the target in a quartz tube (Section 6.1.2) to check possible xenon losses.

Figure 38

EXCITATION FUNCTION OF THE

$I^{127}(p,n)Xe^{127}$ REACTION

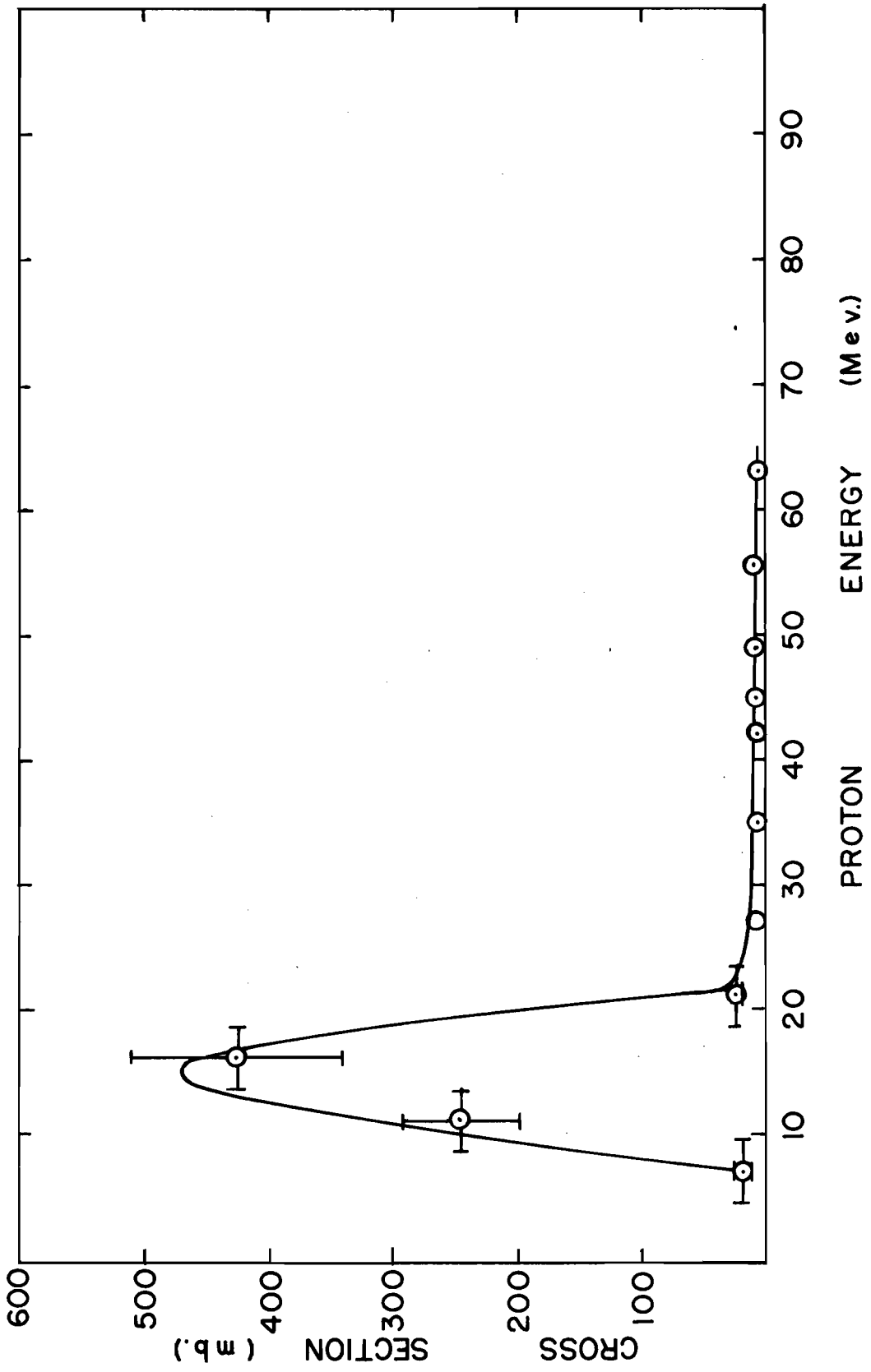
CROSS SECTION (mb.)
100
200
300
400
500
600
10
20
30
40
50
60
70
80
90
PROTON ENERGY (Mev.)

Table X

INDEPENDENT CROSS-SECTIONS FOR THE FORMATION OF Xe^{127}, I^{126}, I^{125}, I^{124} AND I^{123}

Nuclide	Proton Energy Mev	Monitor σ mb	D_x^o dpm	D_m^o dpm	D_x^o/D_m^o	$\frac{N.A_m}{N.A_\tau}$	Ratio of saturation factors	Nuclide σ mb
Xe^{127}								
$t_{\frac{1}{2}}$ = 36.8 d.	7	197.5	9.705×10^3	8.143×10^7	1.192×10^{-4}	0.6909	1035.8	16.8
E_γ = 377 kev	11	487.5	2.993×10^6	4.269×10^9	7.011×10^{-4}	0.6909	1035.8	245
B.R. = 21%	16	100	3.033×10^6	1.565×10^7	1.938×10^{-1}	0.3091	70.92	425
α_T = 0.014	21	356	3.026×10^6	9.86×10^7	3.069×10^{-2}	0.3091	70.92	23.9
	27	344	2.911×10^5	3.392×10^8	8.582×10^{-4}	0.3091	66.85	6.1
	35	294	1.415×10^5	1.828×10^8	7.741×10^{-4}	0.3091	66.85	4.7
	42	260	8.086×10^4	5.003×10^7	1.616×10^{-3}	0.3091	66.85	6.7
	49	232	1.798×10^5	1.065×10^8	4.222×10^{-4}	0.3091	66.85	8.1
	56	208	1.213×10^5	5.45×10^7	5.563×10^{-4}	0.3091	66.85	9.6
	63	186	2.593×10^4	2.077×10^7	1.248×10^{-3}	0.3091	67.05	4.9
	45*	248	2.507×10^4	1.665×10^7	1.505×10^{-3}	0.3091	67.05	7.7

*Bombardment was done with target in a quartz tube.

Table X (Contd.)

Nuclide	Proton Energy Mev	Monitor σ mb	D_x^o dpm	D_m^o dpm	D_x^o/D_m^o	$\frac{N.A_m}{N.A_\tau}$	Ratio of saturation factors	Nuclide σ mb
I^{126}								
$t_{\frac{1}{2}}$ = 13.34 d.	21	356	1.483×10^6	9.86×10^7	1.504×10^{-2}	0.3091	25.328	41
E_γ = 386 kev	27	344	5.498×10^6	3.392×10^8	1.621×10^{-2}	0.3091	24.309	41.9
B.R = 34%	35	294	4.95×10^6	1.828×10^8	2.708×10^{-2}	0.3091	24.309	59.8
α_T = 0.017	42	260	2.327×10^6	5.063×10^7	4.651×10^{-2}	0.3091	24.309	90.9
	49	232	5.848×10^6	1.065×10^8	5.491×10^{-2}	0.3091	24.309	95.8
	56	208	2.911×10^6	5.45×10^7	5.341×10^{-2}	0.3091	24.309	83.5
	63	186	1.474×10^6	2.077×10^7	7.097×10^{-2}	0.3091	26.82	109
	80	140	9.798×10^4	1.828×10^6	5.36×10^{-2}	0.3091	22.4	52

Table X (Contd.)

Nuclide	Proton Energy Mev	Monitor σ mb	D_x^o dpm	D_m^o dpm	D_x^o/D_m^o	$\frac{N.A_m}{N.A_\tau}$	Ratio of saturation factors	Nuclide σ mb
I^{125}								
$t_{\frac{1}{2}}$ = 59 d.	27	344	1.958×10^5	3.392×10^8	5.77×10^{-4}	0.3091	133.7	8.2
E_K X-ray = 28 kev	35	294	3.572×10^5	1.828×10^8	19.546×10^{-4}	0.3091	133.7	23.8
	42	260	3.099×10^5	5.003×10^7	6.194×10^{-3}	0.3091	133.7	66.6
$\frac{\alpha_K}{1+\alpha_T} = 0.8$	49	232	8.016×10^5	1.065×10^8	7.53×10^{-3}	0.3091	133.7	72.2
f = 0.81	56	208	6.137×10^5	5.45×10^7	1.126×10^{-3}	0.3091	133.7	96.8
ω_k = 0.88	63	186	2.356×10^5	2.077×10^7	1.134×10^{-3}	0.3091	134.1	87.5
	70	161	3.91×10^5	3.291×10^7	1.188×10^{-3}	0.3091	112	66.2
	80	140	1.793×10^4	1.828×10^6	9.808×10^{-3}	0.3091	112	47.5

Table X (Contd.)

Nuclide	Proton Energy Mev	Monitor σ mb	D_x^o dpm	D_m^o dpm	D_x^o/D_m^o	$\frac{N.A_m}{N.A_\tau}$	Ratio of saturation factors	Nuclide σ mb
I^{124}								
$t_{\frac{1}{2}}$ = 4.34 d.	42	260	4.822×10^5	5.003×10^7	9.637×10^{-3}	0.3091	8.103	6.3
E_K X-ray = 28 kev	49	232	4.999×10^6	1.065×10^8	4.696×10^{-2}	0.3091	8.103	27.3
f = 0.85	63	186	2.25×10^6	2.077×10^7	1.083×10^{-1}	0.3091	7.888	49.1
ω_k = 0.88	70	161	3.413×10^6	3.291×10^7	1.037×10^{-1}	0.3091	8.145	42.1
$\frac{\alpha_k}{1 + \alpha_T} \simeq 0$	80	140	1.247×10^5	1.828×10^6	6.825×10^{-2}	0.3091	8.145	24.1

Table X (Contd.)

Nuclide	Proton Energy Mev	Monitor σ mb	D^o_x dpm	D^o_m dpm	D^o_x/D^o_m	$\frac{N.A_m}{N.A_\tau}$	Ratio of saturation factors	Nuclide σ mb
I^{123}								
$t_{\frac{1}{2}}$ = 13.68 h.	49	232	1.991×10^7	1.065×10^8	1.87×10^{-1}	0.3091	1.07	14.4
E_γ = 159 kev.	56	208	1.444×10^8	5.45×10^7	2.65	0.3091	1.07	182
B.R = 99%	63	186	7.931×10^7	2.077×10^7	3.819	0.3091	1.07	235
α_T = 0.329	70	161	1.163×10^8	3.291×10^7	3.534	0.3091	1.07	188
	80	140	5.131×10^6	1.828×10^6	2.807	0.3091	1.07	130

The gamma-ray spectrum of Xe^{127} is shown in Fig. 39(A). At higher energies, not only Xe^{127}, but also Xe^{125}, Xe^{123}, Xe^{122}, and Xe^{121} are formed. The gamma energies of these nuclides are very closely spaced, as indicated in Table XI.

Table XI[54]

GAMMA-RAY* ENERGIES IN MEV OF NEUTRON-DEFICIENT ISOTOPES OF XENON

Xe^{127}	0.058, (.12%)	0.146,	0.173, (25%)	0.204,	0.377 (21%)
Xe^{125}	0.054,	0.074,	0.113,	0.187,	0.242
Xe^{123}	0.148				
Xe^{122}	0.182,	0.235			
Xe^{121}	0.096				

*Known branching ratios are shown in brackets.

It became difficult to resolve the photopeaks. If one considers the average counter efficiency for these gamma rays, the error involved in absolute disintegration rates alone is as high as 28%. A typical gamma spectrum at 42 Mev is shown in Fig. 39(B).

The cross-bombardment of the target nucleus in a sealed quartz tube shows that, at most, only small losses of xenon occur if the iodine is bombarded in a mechanically

Figure 39

(A) GAMMA-RAY SPECTRUM OF Xe^{127} AT 22 MEV.

(B) GAMMA-RAY SPECTRUM OF THE XENON SAMPLE AT 49 MEV.

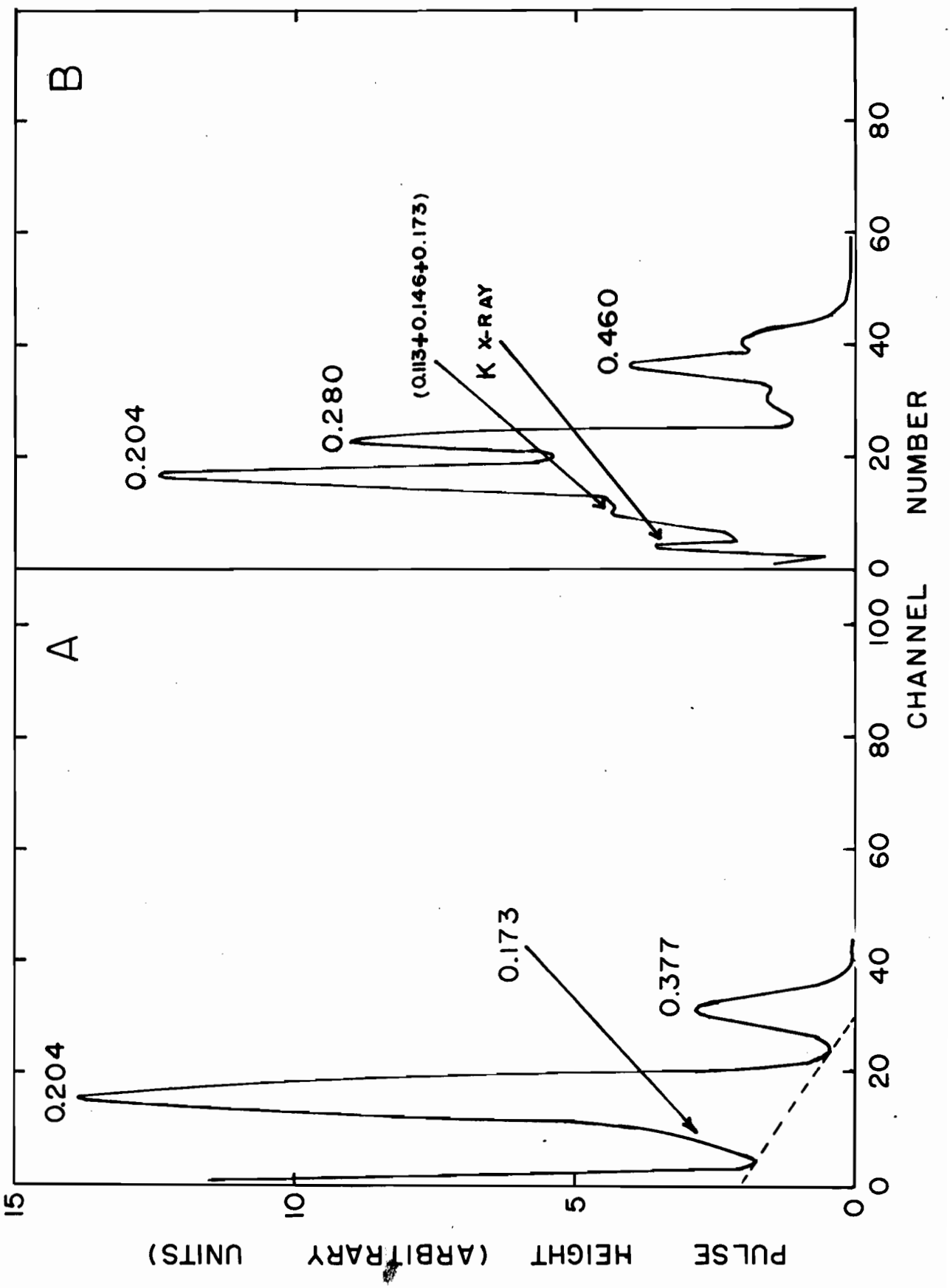
A
B
0.204
0.173
0.377
0.204
0.280
(0.113+0.146+0.173)
K X-RAY
0.460
PULSE HEIGHT (ARBITRARY UNITS)
CHANNEL NUMBER
0
5
10
15
0
20
40
60
80
100

sealed aluminum tube. The results are shown in Table IX.

6.1.3 $I^{127}(p,pn)I^{126}$

The half-life, as well as the cross section of the product nucleus, I^{126}, was determined by following the decay of the total photopeak of the 386 kev gamma ray that follows negatron emission. This gamma ray has a branching ratio of 34% (54).

Seven samples, separated radiochemically at various energies, were studied for half-life determination. The value of the half-life obtained in this work was 13.3 $\pm$ 0.3 days. A typical decay curve of I^{126} is shown in Fig. 40. This value is in close agreement with the value of 13.1 days obtained by Aagaard et al.(140).

The absolute cross-section values determined in this work are listed in Table IX, and the outlines of the calculations are illustrated in Table X. The excitation function of this reaction is given in Fig. 41.

The gamma-ray spectrum observed at 27 Mev is shown in Fig. 42(A).

6.1.4 $I^{127}(p,p2n)I^{125}$

The product nucleus, I^{125}, decays to Te^{125} (stable) entirely by electron capture(54). Thus the half-life, as well as the cross section, was determined by following the decay of the total K X-ray photopeak. In addition to I^{125}, I^{126}, I^{124}, and I^{123} give K X-rays. Therefore the decay of the iodine sample was followed for about 150 days. Nine

Figure 40

DECAY CURVE OF THE 386 KEV

PEAK HEIGHT OF I^{126}

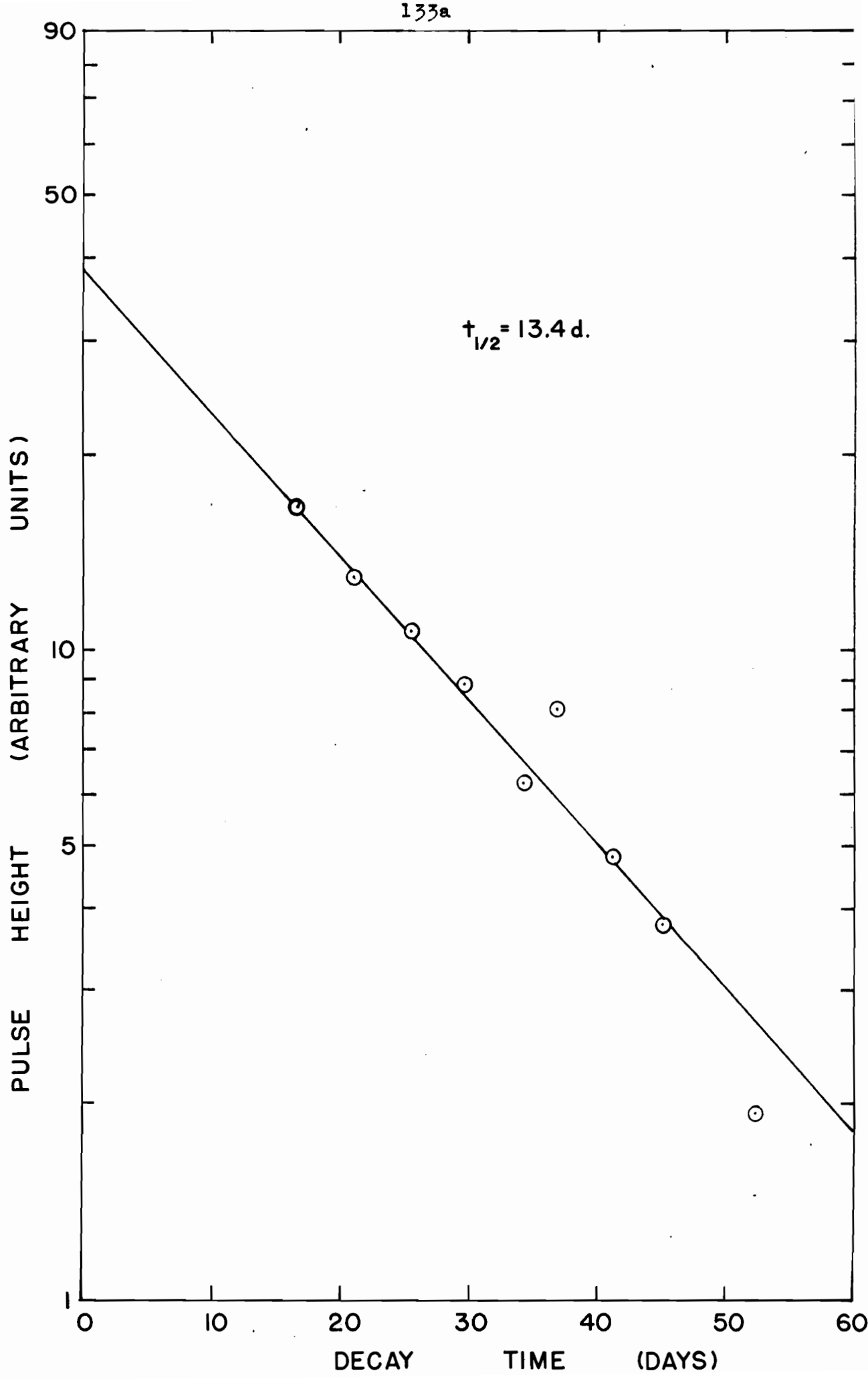
90
50
10
5
1
PULSE HEIGHT (ARBITRARY UNITS)
$t_{1/2}$ = 13.4 d.
0
10
20
30
40
50
60
DECAY TIME (DAYS)

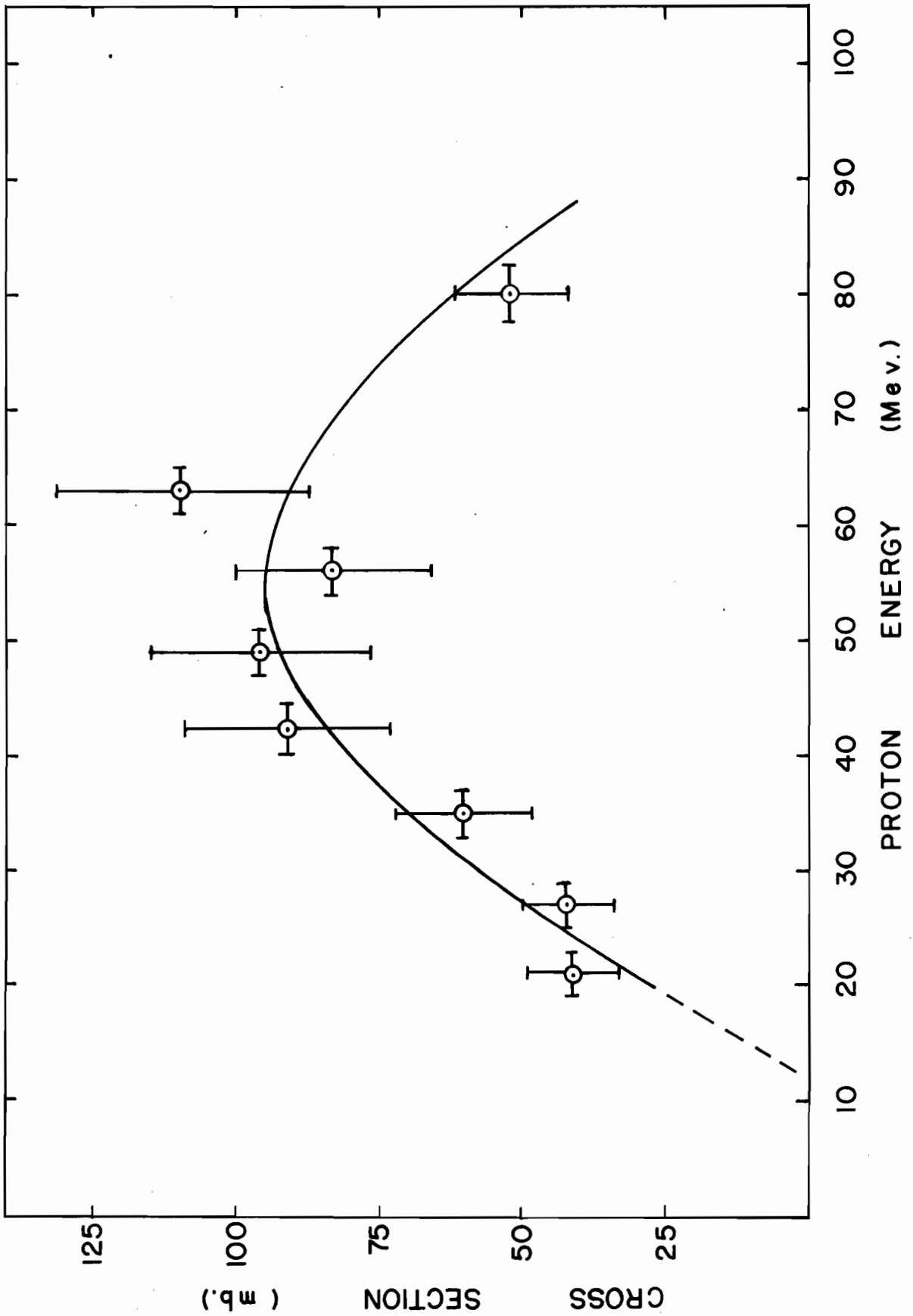
CROSS SECTION (mb.)
125
100
75
50
25
10
20
30
40
50
60
70
80
90
100
PROTON ENERGY (Mev.)

Figure 42

(A) GAMMA-RAY SPECTRUM OF A SEPARATED IODINE SAMPLE AT 27 MEV.

(B) GAMMA-RAY SPECTRUM OF A SEPARATED IODINE SAMPLE AT 49 MEV.

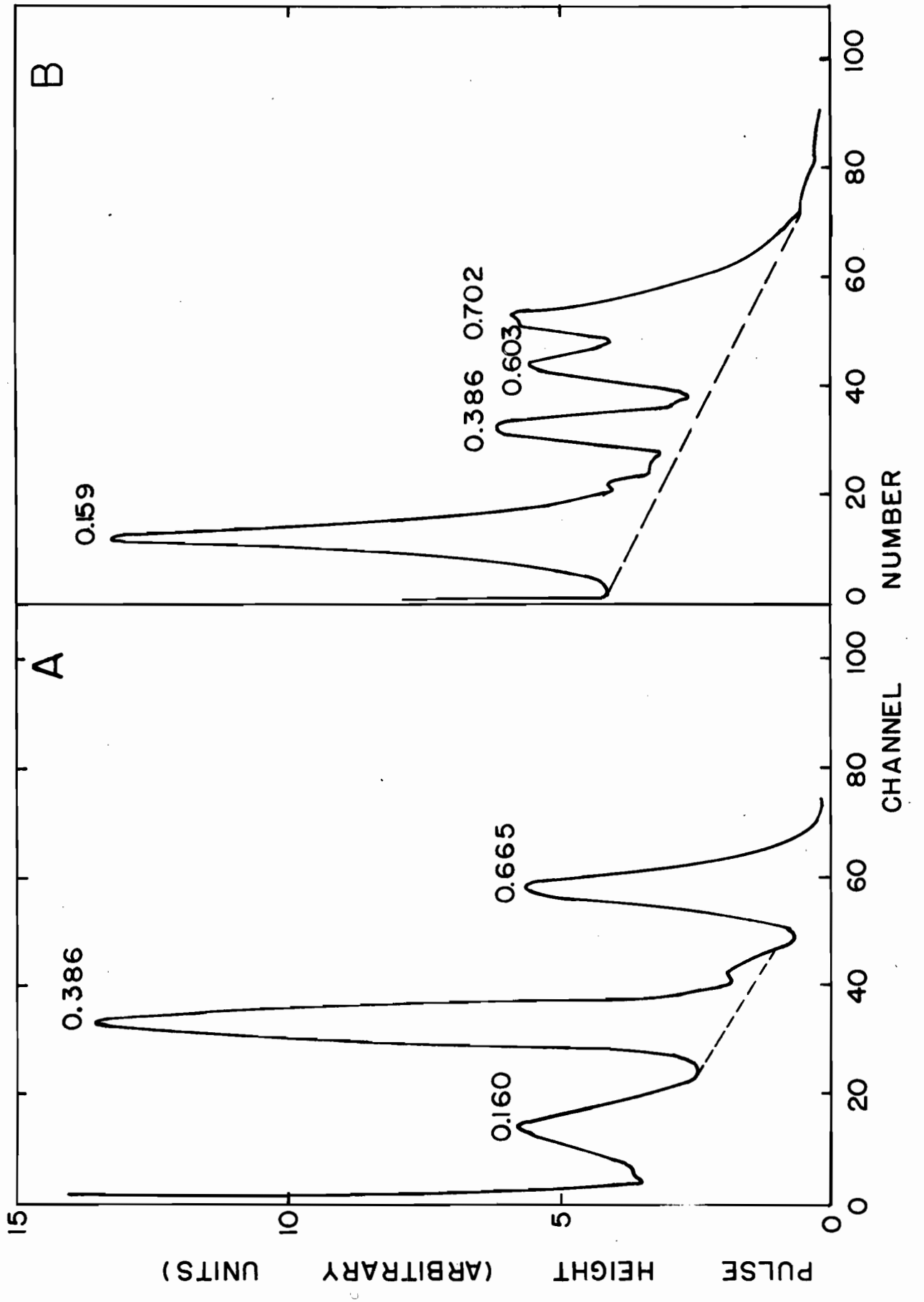
A
B
0.386
0.160
0.665
0.159
0.386
0.603
0.702
PULSE HEIGHT (ARBITRARY UNITS)
CHANNEL NUMBER
0
5
10
15
0
20
40
60
80
100

samples were studied, and the half-life obtained in this work was 59.0 ± 2.1 days. A typical decay curve of the iodine sample obtained at 49 Mev is shown in Fig. 43.

Absolute disintegration rates at the end of bombardment were determined from expression (20) (Section 5.5.5) and cross sections were determined from expression (21) (Section 5.6). The outlines of the calculations are illustrated in Table X, and the absolute values of the cross section are given in Table IX. The excitation function of this reaction is shown in Fig. 44.

The contribution due to the decay of Xe^{125} was considered insignificant, since the time for separating xenon from the other spallation products was very small ($\sim$ 20 minutes) from the end of bombardment in comparison with the half-life of Xe^{125} (18 hours).

6.1.5 $\underline{I^{127}(p,p3n)I^{124}}$

The product nucleus I^{124} decays to Te^{124} (stable) by electron capture and positron emission. The gamma rays which follow the electron capture events are closely spaced in energies, and so it was difficult to resolve the resulting photopeaks. Therefore, in this case, absolute disintegration rates were determined by following the decay of the total K X-ray photopeak. Background activities due to the K X-ray of I^{126} (13.8 d) and I^{125} (59.0 d) were subtracted. The resolution of such a composite decay curve is shown in Fig. 43.

Figure 43

DECAY CURVE OF THE TOTAL K X-RAY PEAK OF I^{126}, I^{125}, AND I^{124}

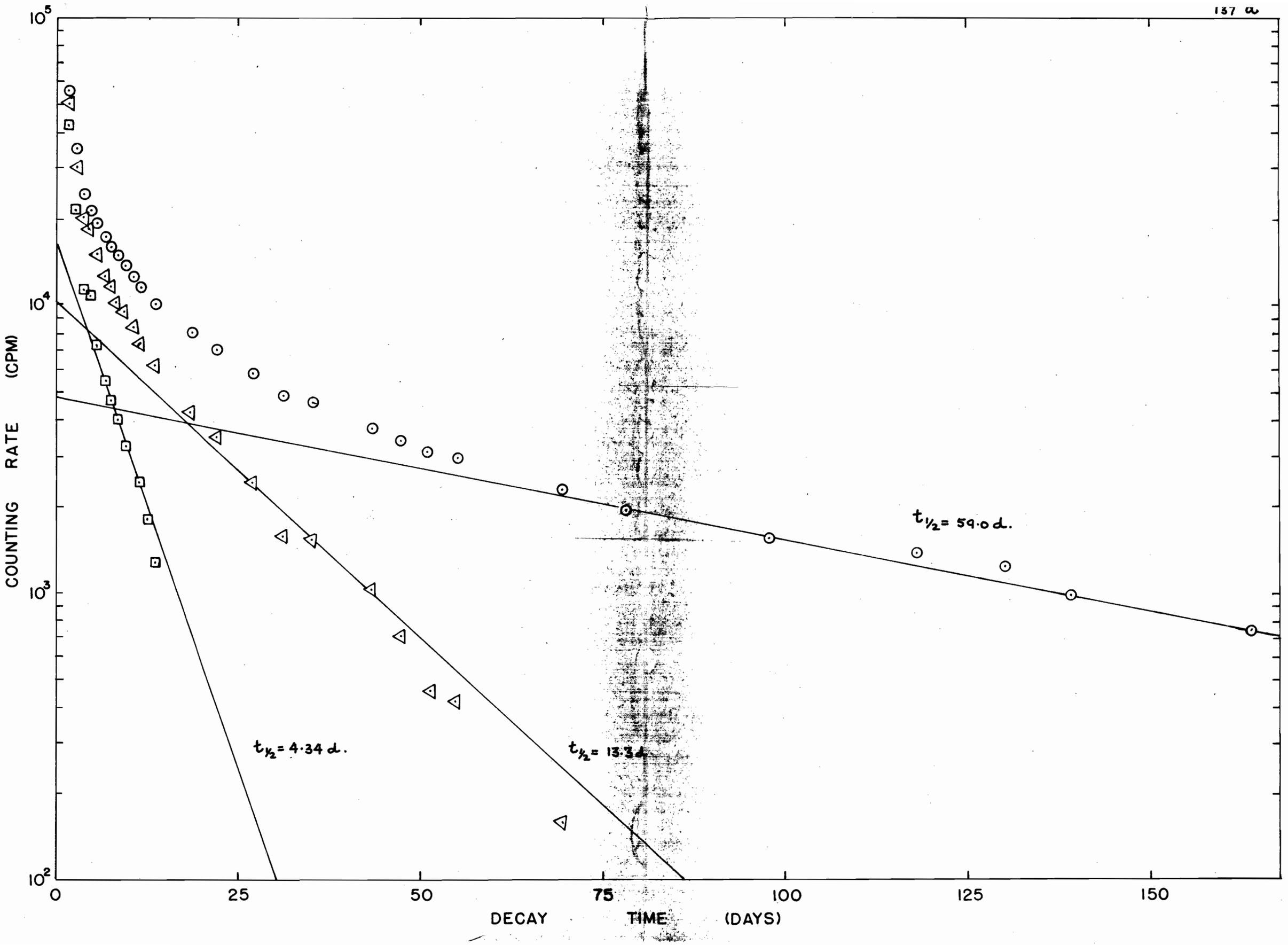
COUNTING RATE (CPM)
10^5
10^4
10^3
10^2
0
25
50
75
100
125
150
DECAY TIME (DAYS)
$t_{1/2}$ = 4·34 d.
$t_{1/2}$ = 13·3 d.
$t_{1/2}$ = 59·0 d.

Figure 44

EXCITATION FUNCTION OF THE

$I^{127}(p,p2n)I^{125}$ REACTION

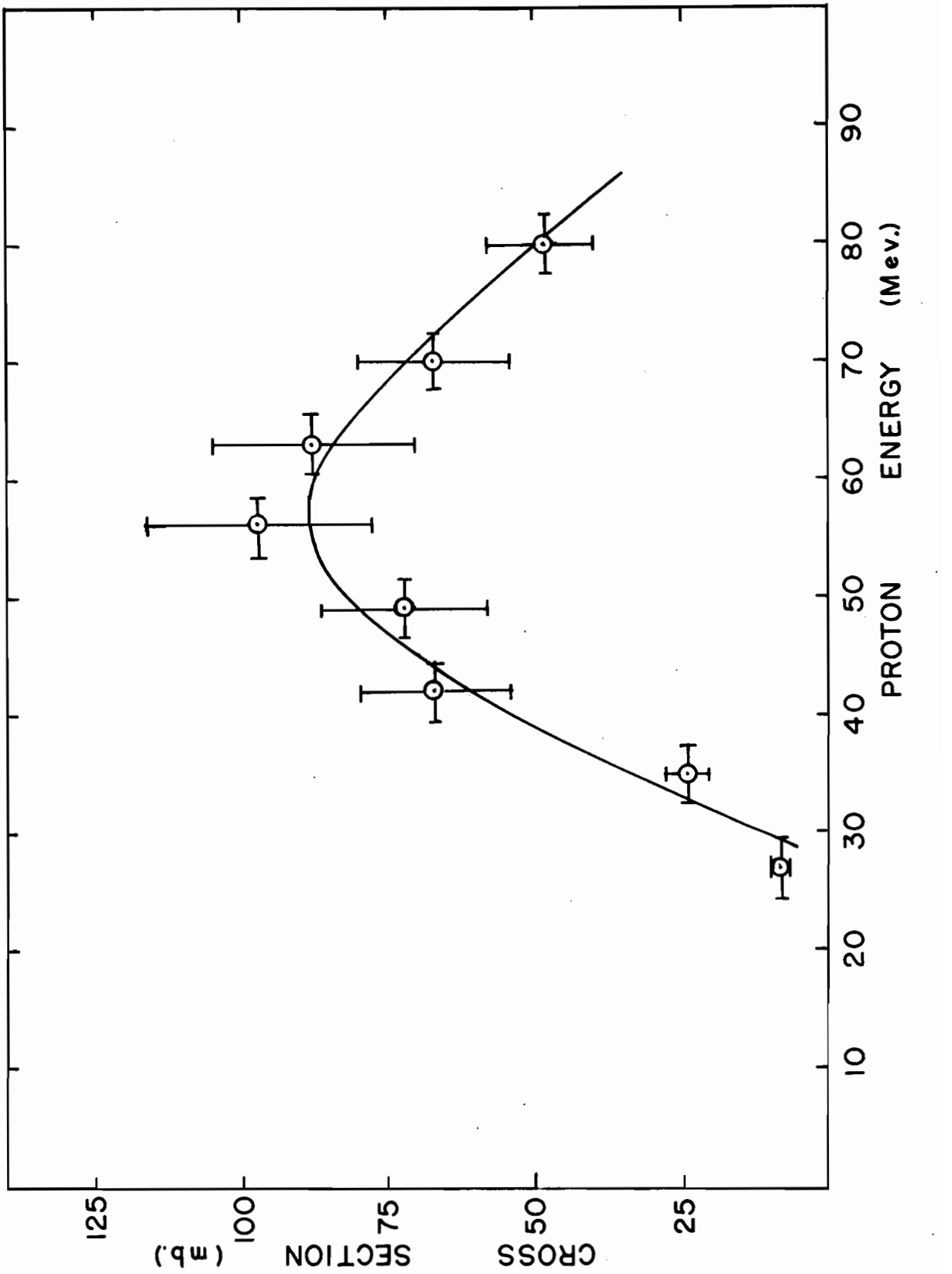
CROSS SECTION (mb.)
25
50
75
100
125
PROTON ENERGY (Mev.)
10
20
30
40
50
60
70
80
90

Seven samples were followed for half-life determination. The value obtained in this work was 4.34 ± 0.03 days. The present value for the half-life of I^{124} is in close agreement with the value of 4.2 days as obtained by Mitchell et al.[163].

Cross sections were determined from expression (21) (Section 5.6). The internal conversion correction due to gamma rays that follow electron capture events is generally small, except when low-energy M1 transitions are involved, which are highly converted[111]. In the case of I^{124}, all the gamma energies involved were above 600 kev, and the internal conversion correction was found to be less than one percent. The outlines of the calculation are illustrated in Table X, and the absolute values of the cross sections are shown in Table IX. The excitation function for this reaction is given in Fig. 45.

6.1.6 $I^{127}(p,p4n)I^{123}$

The half-life, as well as the cross sections of the product nucleus I^{123}, was determined by following the decay of the 159 kev gamma ray (branching ratio 99%) that follows the electron capture events. A typical gamma spectrum of I^{123} at 49 Mev is shown in Fig. 42(B).

The outlines of the cross-section calculations are shown in Table X, and the values of the cross sections at various energies are given in Table IX. The excitation function for this reaction is illustrated in Fig. 46.

Figure 45

EXCITATION FUNCTION OF

$I^{127}(p,p3n)I^{124}$ REACTION

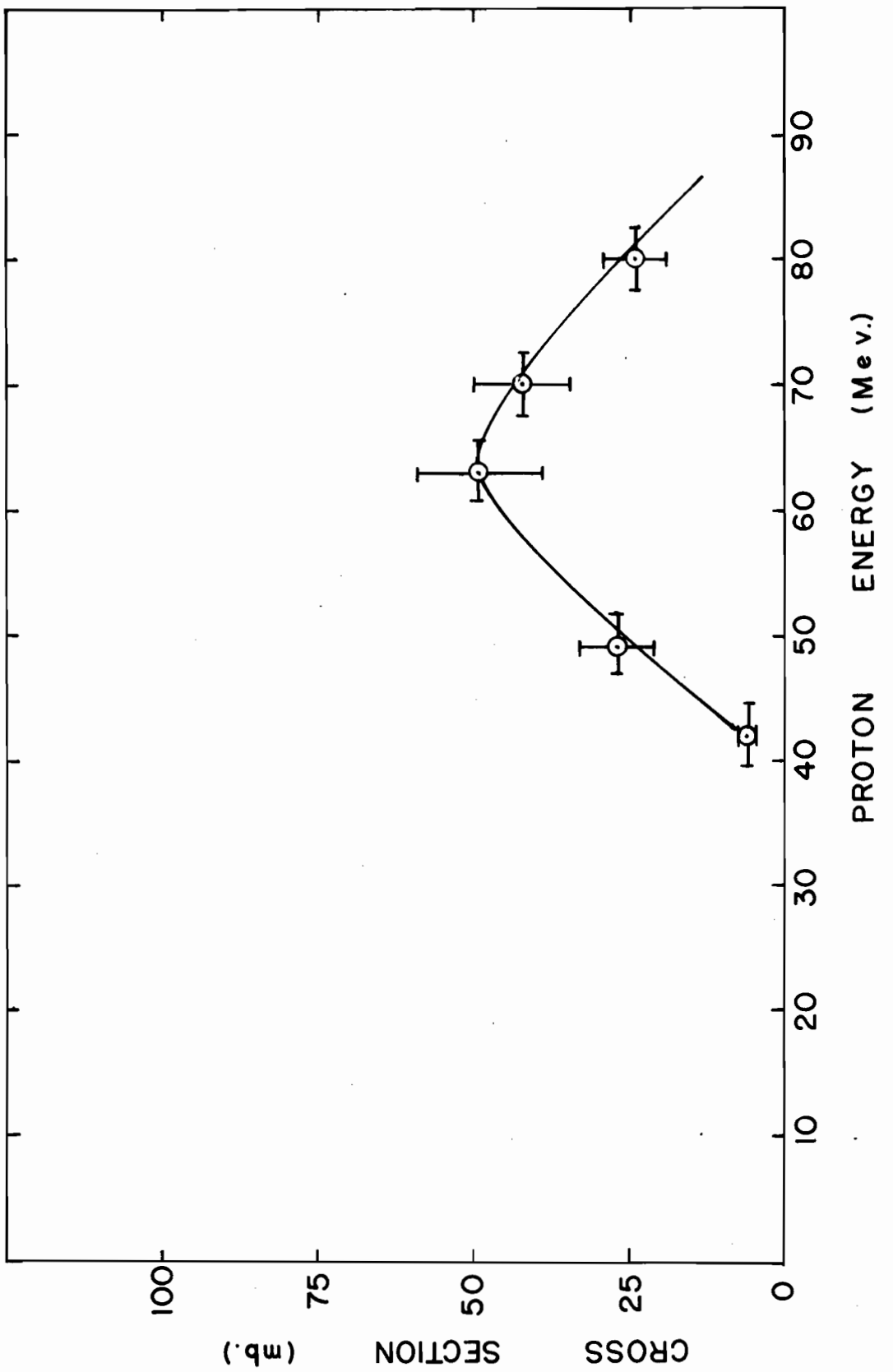
CROSS SECTION (mb.)
0
25
50
75
100
10
20
30
40
50
60
70
80
90
PROTON ENERGY (Mev.)

Figure 46

EXCITATION FUNCTION OF

$I^{127}(p,p4n)I^{123}$ REACTION

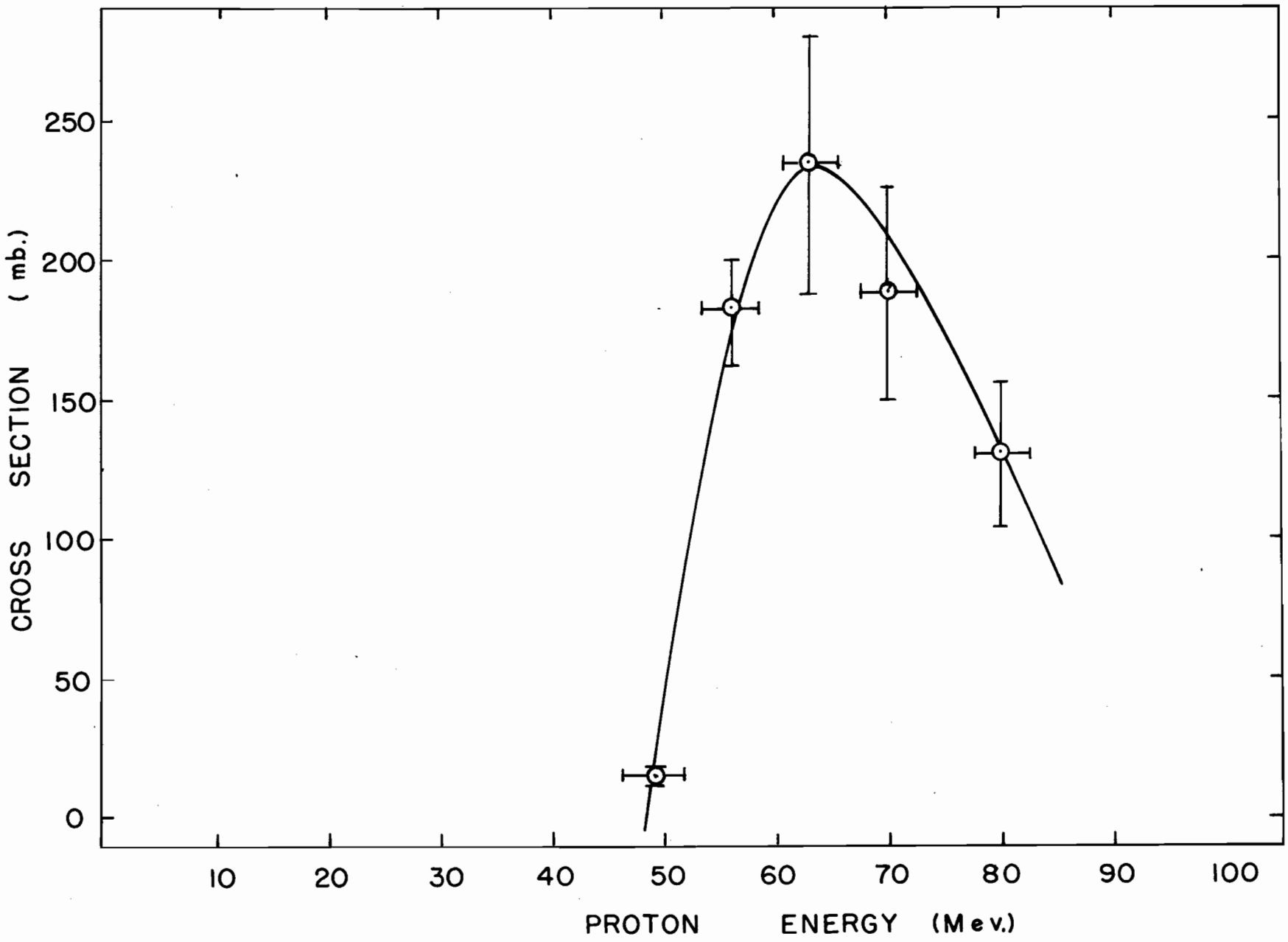
CROSS SECTION (mb.)
250
200
150
100
50
0
10
20
30
40
50
60
70
80
90
100
PROTON ENERGY (Mev.)

The decay of six samples was followed for the half-life determination. The value obtained in the present work was 13.7 ± 0.3 hours. This value is in close agreement with that of 13 hours obtained by Marquez and Perlman[139]. A typical decay curve is shown in Fig. 47.

6.2 DISCUSSION

6.2.1 $I^{127}(p,n)Xe^{127}$

The excitation function of the reaction $I^{127}(p,n)Xe^{127}$ (see Fig. 38) shows a sharp peak at 15 Mev and a tailing off at 21 Mev to almost a constant value of $\sim$ 8 mb. The shape of the excitation function strongly supports the compound nucleus mechanism[98,100].

Jackson[128] proposed a schematic model to describe (p,xn) reactions based on statistical assumptions. This model predicts that in the heavy target elements, such as bismuth and lead, the probability of evaporation of one neutron is a maximum in the energy range of 8 to 12 Mev. It was observed that the maximum probability of evaporation of one neutron lies at 15 ± 2.5 Mev.

Unfortunately, due to the practical limitations, further information for the (p,xn) reaction $x > 1$ could not be obtained and hence no definite statement can be made.

6.2.2 (p,pxn) Reactions

Aagaard et al.[140] reported the formation of 2.6-hr. I^{126m} while studying the fission of uranium induced

Figure 47

DECAY CURVE OF THE 159 KEV

PEAK HEIGHT OF I^{123}

(Bombarding Energy 63 Mev)

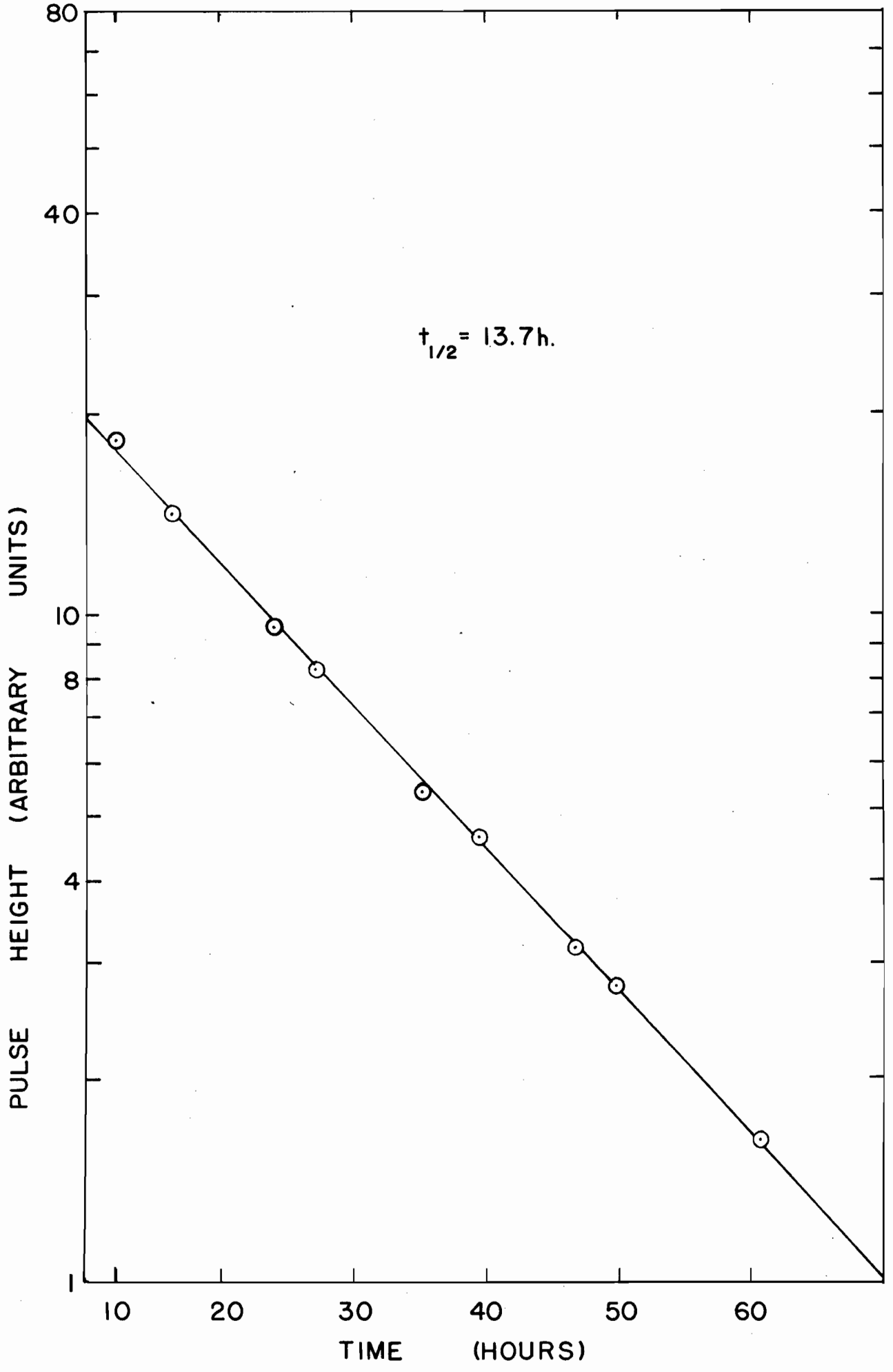
80
40
10
8
4
1
$t_{1/2}$ = 13.7h.
PULSE HEIGHT (ARBITRARY UNITS)
10
20
30
40
50
60
TIME (HOURS)

by 170 Mev protons. An intensive search was made to identify this metastable state of I^{126}. The β^-, γ, and X-ray measurements revealed negative results. Thus the author believes that at the proton bombarding energies used either it is not formed at all or the yield is so low that it could not be detected.

Examination of the excitation functions of (p,pxn) reactions (see Figs. 41, 44, 45, and 46) shows that with increasing proton bombarding energies the cross-section values decrease as x increases, with the exception of the $I^{127}(p,p4n)I^{123}$ reaction. The reason is that the correction, due to the growth of I^{123} from the decay of Xe^{123} (1.85 hrs) during the interval from the end of bombardment to the time of separation of the xenon fraction ($\sim$ 20 mins.), could not be made due to the limitations of the present work (Section 4.3). Thus, this accounts for the higher yields of I^{123}.

However, the nature of these excitation functions is in accordance with the cascade-evaporation model (Section 4.2.4) based on statistical theory. Since (p,pxn) reactions, which involve inelastic scattering of the incident protons, are inhibited by the coulomb barrier in both the entrance and exit channels, then on the basis of the statistical theory such reactions in general are expected to have much smaller cross sections than the (p,xn) reaction.

The results of the present work further reveal that

the (p,n) cross sections are higher than the (p,pn) cross sections by a factor of ~ 4, while statistical theory demands that this factor should be much larger. Bell and Kavanagh[113] also found this discrepancy in $Au^{197}(p,pxn)$ reactions while comparing their results with those obtained by Bell and Skarsgard[111]. These larger values are presumably due to the inelastic scattering of protons and thus can be interpreted in terms of nucleon-nucleon collision in the diffuse surface region of the target nucleus[164]. Statistical calculations were made by Metropolis et al.[129], Bernadini et al.[124] and Jackson[128] on the basis of a well-defined nuclear boundary.

Yule and Turkevich[165] obtained theoretical values for (p,pn) reaction cross sections at energies above 80 Mev. These calculations were based on the inter-nuclear cascade evaporation mechanism. In one of such calculations they found that at 83 Mev mass number 127 should have a cross-section value of 43 ± 5 mb, and this value decreases with the increase of incident proton energy. In the present work it was found that at 80 Mev the cross section of the $I^{127}(p,pn)$ reaction was 50 ± 10 mb, which shows an agreement with the predictions.

Bell and Kavanagh[113] found that $Au^{197}(p,pn)Au^{196}$ reaction cross sections are higher than those of the $Au^{197}(p,p2n)Au^{195}$ reaction. They gave the explanation that the (p,pn) reaction usually includes the contribution due to

the (p,d) pick-up reaction. But, in the present work, it was found that the values of the cross sections of the (p,pn) and (p,p2n) reactions are comparable except for the difference in threshold. Thus, if the pick-up reaction explanation is correct, these reactions appear to be less predominant in medium weight elements.

6.2.3 Surface interactions

In the present work, if one corrects for the threshold, it was observed that, as the incident energy of the protons increases, the ratios between the (p,pn) and (p,p3n) cross sections also increase. Similar conclusions can be drawn from the works of Ladenbauer[135], Kuznetsova et al.[137], and Fink and Wiig[166]. The results and comparisons are shown in Table XII.

Table XII

Energy	80 Mev	240 Mev (Ref.166)	660 Mev (Ref.137)	720 Mev (Ref.135)
Reaction cross section				
σ(p,pn)	52 $\pm$ 10.4 mb	59 mb	51 $\pm$ 10 mb	56.4 $\pm$ 6.8 mb
σ(p,p3n)	24.1 $\pm$ 4.8 mb	15 mb	17.3 $\pm$ 3 mb	19.1 $\pm$ 6.6 mb
$\frac{\sigma(p,pn)}{\sigma(p,p3n)}$	3.2	4.2	4.3	5.1

This shows that, as the incident proton energy increases, nuclear transparency also increases.

This could be explained on the basis of surface interactions[167]. In a (p,pn) reaction, nucleon-nucleon collision occurs in the outer surface of the nucleus. Thus, in the initial cascade, the incident proton strikes a neutron and both nucleons participating in the collision will leave the nucleus promptly without depositing enough energy for the loss of further nucleons by evaporation. If the initial collision occurs deep in the surface of the nucleus, then their escape becomes less probable, and it is rather unlikely that they will escape without undergoing further collisions. Winsberg and Ladenbauer[167] further stressed that this is particularly the case at the highest bombarding energies, where the meson production and reabsorption process provide a particularly efficient energy transfer mechanism. The cross sections for simple (p,pn) and (p,2p) reactions should therefore be dependent on whether the reaction occurs near the nuclear surface and hence on the bombarding energies.

6.2.4 Effects of Nuclear shell structure

According to Mayer and Jensen[115], there are certain numbers of neutrons and protons which form nuclei with particularly stable configurations. It is well known that the level structure yields shell closures at 'magic numbers' of N or Z = 2, 8, 20, 28, 50, 82, and 126. If one assumes that the magic number nuclei have abnormally low-level

densities, one can find the influence of shell structure on the reaction cross sections. It then follows from the statistical theory[101,102] that the probability of an evaporation step decaying to a magic number product is depressed. Since the excitation results from the knock-on process, evaporation dominates in the last steps of de-excitation, and thus the yields of the magic number products should be low.

The cross sections of the (p,pxn) reactions at 80 Mev in this study were compared with those obtained by Fink and Wiig[166] for the corresponding (p,pxn) reaction on Cs^{133}, since cesium differs only slightly from iodine in atomic weight. Moreover, the Z/N ratios are almost identical (1.42 and 1.40 respectively), and similar cross sections might be expected for the same reaction. Such a comparison is made in Table XIII (p. 149).

Iodine has Z = 53, three units more than required by a magic number configuration, while cesium has five units more than magic number configuration. Thus this may be one reason why the yields of (p,pxn) reactions on cesium are higher than yields of the corresponding iodine reactions.

If one takes the ratios of the yields of the corresponding odd-odd and odd-even reaction products, there is a great divergence in the ratios (see Table XII, Column IV) while it should be the same according to the statistical theory. A similar discrepancy was observed by Sharp et al.[168]

Table XIII

COMPARISON OF THE (p,pxn) CROSS SECTIONS OF Cs^{133} AND I^{127} AT 80 MEV

Reaction	odd-even character Z - N	σ_x mb	$\frac{\sigma_x \text{ I}}{\sigma_x \text{ Cs}}$
$I^{127}(p,pn)I^{126}$	0 - 0	52	0.046
$Cs^{133}(p,pn)Cs^{132}$	0 - 0	1120 (166)	
$I^{127}(p,p2n)I^{125}$	0 - E	47	0.098
$Cs^{133}(p,p2n)Cs^{131}$	0 - E	480 (166)	
$I^{127}(p,p3n)I^{124}$	0 - 0	24	0.522
$Cs^{133}(p,p3n)Cs^{130}$	0 - 0	46 (166)	

while comparing the results of the $Cu^{63}(p,pxn)$ and $Co^{59}(p,pxn)$ reactions. These discrepancies might be due to the shell closure effects.

6.3 APPLICATION OF THE RUDSTAM EQUATION

The cross section σ for a nucleus (A,Z) in general can be written

$$\sigma = f(A,Z) \quad \ldots\ldots\ldots\ldots\ldots\ldots \quad (29)$$

According to Rudstam[127] this function, f, is an exponential function, i.e.

$$\sigma = \exp\left[AP - Q - R(Z - SA)^2\right] \quad \ldots\ldots\ldots \quad (30)$$

where P, Q, R, and S are some unknown parameters, to be determined from the experimentally observed values of σ's for given (A,Z)'s, and where A and Z are the mass number and charge number of the nuclide under consideration.

Equation (30) can be expressed in a more convenient form

$$\ln \sigma = AP - Q - R(Z - SA)^2 \quad \ldots\ldots\ldots\ldots \quad (31)$$

One may tend to think that only four sets of observed values $(\ln \sigma, A,Z)$ are needed to solve equation (31) exactly for the four unknown parameters. But this is not true. The problem is slightly intricate and the intricacy arises due to

(i) non-linearity of S because

$$(Z - SA)^2 = S^2A^2 - 2SAZ + Z^2 \quad \ldots\ldots\ldots\ldots\ldots \quad (32)$$

& (ii) coupling of R and S, because of the term $R(Z - SA)^2$.

Besides, this 'exact solution' approach is not really a very good one, if we recall that equation (30) is an empirical equation.

The correct approach in cases like these is the so-called Regression analysis approach, because the problem is to determine that set of (P, Q, R, S) values which will give us the 'best' fit for the experimentally observed points ($\ln\sigma$, A, $\frac{z}{}$).

The author has solved equation (30) numerically with the help of a Burroughs 220 computer, by using the method of least squares.

Let $Y_c = \ln\sigma$, $U_1 = A$, $U_2 = -1$, $U_3 = -(\frac{z}{} - SA)^2$ ..... (32)

For a fixed value of S, equation (31) becomes

$$Y_c = U_1P + U_2Q + U_3R \quad \text{.....} \quad (33)$$

Suppose Y is the observed value of $\ln\sigma$ and n such observations have been made:

$$\text{Let} \qquad V = \sum_i^n E_i^2 = \Sigma(Y - Y_c)^2 \quad \text{.....} \quad (34)$$

$$\text{or} \qquad V = \sum_i^n [Y - (U_1P + U_2Q + U_3R)]^2 \quad \text{....} \quad (35)$$

According to the principle of least squares, V should be a minimum with respect to P, Q, and R.

$$\text{Therefore } \frac{\partial V}{\partial P} = 0 = -2 \sum_i^n [Y - (U_1P + U_2Q + U_3R)]U_1 \quad \text{..} \quad (36)$$

$$\frac{\partial V}{\partial Q} = 0 = -2 \sum_{i}^{n} \left[Y - (U_1 P + U_2 Q + U_3 R) \right] U_2 \quad \ldots\ldots\ldots (37)$$

$$\frac{\partial V}{\partial R} = 0 = -2 \sum_{i}^{n} \left[Y - (U_1 P + U_2 Q + U_3 R) \right] U_3 \quad \ldots\ldots\ldots (38)$$

Equations (36), (37), and (38) can be put in the form of a matrix equation:

$$\underbrace{\begin{bmatrix} \Sigma U_1^2 & \Sigma U_1 U_2 & \Sigma U_1 U_3 \\ \Sigma U_2 U_1 & \Sigma U_2^2 & \Sigma U_2 U_3 \\ \Sigma U_3 U_1 & \Sigma U_3 U_2 & \Sigma U_3^2 \end{bmatrix}}_{L} \underbrace{\begin{bmatrix} P \\ Q \\ R \end{bmatrix}}_{C} = \underbrace{\begin{bmatrix} \Sigma U_1 Y \\ \Sigma U_2 Y \\ \Sigma U_3 Y \end{bmatrix}}_{D} \quad \ldots (39)$$

(where $U_1 U_2 = U_2 U_1$, $U_3 U_1 = U_1 U_3$, $U_2 U_3 = U_3 U_2$).

Equation (39) can be written as

$$[C] = [L]^{-1} [D] \quad \ldots\ldots\ldots\ldots\ldots (40)$$

Five sets of values of U_1, U_2, U_3, and Y were taken for five nuclei: ${}_{54}Xe^{127}$, ${}_{53}I^{126}$, ${}_{53}I^{125}$, ${}_{53}I^{124}$, and ${}_{53}I^{123}$.

$\Sigma U_i U_j$, $\Sigma U_i Y$, $i = 1,2,3$, and $j = 1, 2, 3$

were computed.

Then the matrix equation (39) was computed. This gave the values of P, Q, and R for one fixed value of S.

Six such sets of (P, Q, and R) for six values of S (1, 0.5, 0.25, 0.4, 0.30, 0.356) were obtained by the above method. These values are listed in Table XIV.

Table XIV

VALUES OF P, Q AND R

Assumed values of S	Corresponding calculated values P	Q	R
1	4.171×10^{-3}	-3.277	-4.5×10^{-5}
0.5	-10.3799	-1.4037×10^{3}	9.2288×10^{-1}
0.25	-8.2902×10^{-1}	-1.3679×10^{2}	6.0476×10^{-2}
0.3	-9.4262×10^{-1}	-1.4191×10^{2}	8.1364×10^{-2}
0.356	-1.2251	-1.6785×10^{2}	1.9056
0.4	-1.2129	-1.5976×10^{2}	3.9623×10^{-1}

For these six sets of (P, Q, R, and S) values, the corresponding ln σ values were calculated by solving the matrix equation.

$$\begin{bmatrix} Y_{C_1} \\ Y_{C_2} \\ Y_{C_3} \\ Y_{C_4} \\ Y_{C_5} \\ Y_{C_6} \end{bmatrix} = \begin{bmatrix} & U_1 & U_2 & \\ A_1 & -1 & U_3 \\ A_2 & -1 & U_3 \\ A_3 & -1 & U_3 \\ A_4 & -1 & U_3 \\ A_5 & -1 & U_3 \\ A_6 & -1 & U_3 \end{bmatrix} \begin{bmatrix} P \\ Q \\ R \end{bmatrix} \quad \ldots\ldots\ldots (41)$$

The above matrix equation (41) was written down as:

$$[\sigma] = [L]\,[D] \qquad \ldots\ldots\ldots\ldots\ldots\ldots \quad (42)$$

Equation (41) again was solved on the computer.

The matrix $[\sigma]$ in equation (42) gave the five calculated values of $\ln \sigma$. Six such sets of $[\sigma]$ for six values of S were obtained. The corresponding six sets of calculated root mean square error, E's, were calculated. The value of E is given by the following expression:

$$E = \sqrt{\frac{\sum_{i}^{n} (Y - Y_0)^2}{n - 1}} \qquad \ldots\ldots\ldots\ldots \quad (43)$$

where Σ implies summation over the five nuclei under observation. The results are shown in Table XV.

Table XV

THE RMS ERROR E CORRESPONDING TO S VALUES

Assumed values of S	E	e^E
1	1.473	4.34923
0.5	0.865	2.36316
0.4	0.59	1.80398
0.356	0.55	1.73325
0.3	0.53	1.69893
0.25	0.54	1.71600

A graph was plotted, e^E as ordinate and S as the abscissa. This plot gave S = 0.3 for the minimum value of e^E. E corresponds to the error in $\ln\sigma$. We are interested in that set of (P,Q,R, and S) which will give the least root mean square error in σ and not in $\ln\sigma$.

A few remarks may be made on the functional relationship of E and S. The author, taking a clue from the equation

$$\sigma = \exp[AP - Q - R(Z - SA)^2] \quad \ldots\ldots\ldots\ldots (30)$$

wrote down the following equation

$$e^E = \alpha s^2 + \beta s + \gamma \quad \ldots\ldots\ldots\ldots\ldots\ldots (44)$$

expressing E as a function of S.

The matrix equation

$$\begin{bmatrix} e^{E_1} \\ e^{E_2} \\ e^{E_3} \end{bmatrix} = \begin{bmatrix} s_1^2 & s_1 & 1 \\ s_2^2 & s_2 & 1 \\ s_3^2 & s_3 & 1 \end{bmatrix} \begin{bmatrix} \alpha \\ \beta \\ \gamma \end{bmatrix} \quad \ldots\ldots\ldots (45)$$

was solved for three values of S = 1, 0.5, 0.25.

This gave

$$\alpha = 8.50074$$

$$\beta = -6.21571$$

$$\gamma = 2.07727$$

To find a minimum value of E with respect to S, the dE/dS of equation (44) gives

$$2\alpha S + \beta = 0 \quad \text{for (E) = minimum.}$$

$$\text{Therefore} \quad S = \frac{-\beta}{2\alpha} \qquad \ldots\ldots\ldots\ldots\ldots\ldots \quad (45)$$

$$\text{This gives} \quad S = 0.365.$$

This value is in agreement with that obtained graphically.

Calculated cross section

It was found (Table XV) that e^E is a minimum for $P = -9.4262 \times 10^{-1}$, $Q = -1.4191 \times 10^{2}$, $R = 8.1364 \times 10^{-2}$ and $S = 0.3$. The value of e^E in this particular case was 1.6989. This means that the calculated results are within the factor of 1.6989. This factor is not too large considering the empirical nature of the Rudstam equation (equation 30). Rudstam[127] himself found that this factor varied from 1.42 to 3.13.

The cross sections of various reactions calculated on the basis of the Rudstam equation for 63 Mev protons are shown in Table XVI.

Table XVI

COMPARISON OF OBSERVED CROSS SECTIONS WITH THOSE OBTAINED WITH THE RUDSTAM EQUATION FOR 63 MEV PROTONS

Reactions	Observed cross sections	Calculated cross sections
$I^{127}(p,n)Xe^{127}$	5 ± 1	5.3
$I^{127}(p,pn)I^{126}$	109 ± 21.8	70
$I^{127}(p,p2n)I^{125}$	87.5 ± 17.5	97
$I^{127}(p,p3n)I^{124}$	49.1 ± 9.8	112
$I^{127}(p,p4n)I^{123}$	235 ± 46.9	113

SUMMARY AND CONTRIBUTION TO KNOWLEDGE

A. Emanation methods originally developed by Hahn were used in Part A of the present work to study the phase changes in the solid state with increase of temperature.

The iodides of silver (I), thallium (I), mercury (II), copper (I), and lead (II) were studied by incorporating the $I^{135} \xrightarrow{\beta^-} Xe^{135}$ system. The Xe^{135} activity was measured in a flow type scintillation radiation detection system fabricated by the author. The carrier gas used in this work was Freon-12 (difluoro-di-chloro methane).

The results of the present study are in close agreement with those obtained by the conventional crystallographic techniques. It was further observed that the transition temperatures in this method were very sharp.

The phenomenon of Tammann's 'loosening temperatures' was also observed in the present work. The predictions of Tammann were found to hold for the above compounds. The ratios of the 'loosening temperatures' to the melting points on Absolute scale of the above compounds lay between 0.5 to 0.7, in close agreement with predicted values of 0.5 to 0.6. This substantiates the suggestion of Tammann and Sworykin that a molecular shift in the solid state occurs at temperatures approximately one-half of the melting point on the Absolute scale.

B. The (p,xn) and (p,pxn) reactions on iodine induced by protons of energies 7 to 80 Mev have been studied.

The absolute excitation functions of (p,n) and (p,pxn) reactions (x = 1 to x = 3), based on the known cross sections of the $Cu^{63}(p,n)Zn^{63}$ and $Cu^{65}(p,pn)Cu^{64}$ reactions studied radiochemically, are given.

The values of the half-lives of the various product nuclei, such as Xe^{127} and $I^{123-126}$, have been redetermined.

The cross sections were compared with those calculated on the basis of the Rudstam empirical equation

$$(A,Z) = \exp\left[\sqrt{P}A - Q - R(Z - SA)^2\right]$$

The calculated cross sections were found to be within $\pm$ 1.699 times the observed cross sections.

To find the value of the parameter, S, in the above equation, which would give a minimum error of σ, the following relation has been suggested

$$e^E = \alpha S^2 + \beta S + \gamma$$

The results in the present study have been compared with those of other workers. The reaction mechanisms have been discussed in the light of present knowledge about the theory of nuclear reactions.

APPENDIX I

DETERMINATION OF IODINE ACTIVITY IN FISSION PRODUCTS

The following method was developed by Glendenin and Metcalf[59], which has been shown to be satisfactory for achieving the interchange between inactive and active iodine.

It consists in the oxidation of I^- carrier to IO_4^- (periodate) with NaClO in alkaline solution. After the interchange reaction, the solution is acidified, the IO_4^- is reduced to I_2 with hydroxylamine hydrochloride ($NH_2OH.HCl$) and the I_2 is extracted with CCl_4. The I_2 is removed from the CCl_4 by shaking with water containing $NaHSO_3$ and it is then purified by another CCl_4 extraction cycle, in which $NaNO_2$ is used for the oxidation of I^- to I_2 and $NaHSO_3$ is used for the reduction of I_2 to I^-.

Procedure

Step 1. Add to the sample of fission products (containing not more than 5 g of uranyl nitrate) in a 60-ml separatory funnel about 10 ml of 2 M Na_2CO_3 and 2 ml of I^- (20 mg) of carrier. Add 1 ml of 5% NaClO, mix well (or heat), and acidify the solution by slowly adding 3 ml of concentrated HNO_3. Add 3 ml of 1 M $NH_2OH.HCl$ and extract the I_2 into 10 ml of CCl_4. Discard the aqueous layer.

Step 2. Shake the CCl_4 layer with 10 ml of H_2O containing a few drops of 1 M $NaHSO_3$ until both phases are colourless, and discard the CCl_4 layer.

Step 3. Add 1 ml of 6 M HNO_3 and a few drops of 1 M $NaNO_2$, extract the I_2 into 10 ml of CCl_4, and discard the aqueous layer.

Step 4. Repeat Step 2 to get I^- for the precipitation.

REFERENCES

1. Glossary of terms in Nuclear Science and Technology, ASA NI-1-1957. The American Society of Mechanical Engineers.
2. O. Hahn and O. Müller, Z. Elecktrochem., 29, 189 (1923).
3. A.P. Ratner, Trav. inst. état radium (U.S.S.R.) 3, 139 (1937).
4. S. Flügge and K. Zimens, Z. Physik. Chem., B-42, 179 (1939).
5. J. Kurbatov, J. Phys. Chem., 45, 851 (1941).
6. C. Chamie, J. Chim. Phys., 29, 242 (1932).
7. E.G. Gracheva and V.G. Baranov, Trav. inst. état radium (U.S.S.R.) 3, 117 (1937).
8. F. Strassmann, Z. Physik Chem., B-26, 362 (1934).
9. K. Zimens, Z. Physik. Chem., 191, 1 (1943).
10. R. Fricke and H. Bückmann, Ber., 72, 131 (1939).
11. R. Fricke and O. Glemser, Z. Physik. Chem., B-26, 27 (1937).
12. H. Müller, Z. Physik. Chem., A149, 257 (1930).
13. O. Hahn and M. Biltz, Z. Physik. Chem., A126, 323 (1927).
14. G. Graue and N. Riehl, Angew. Chem., 52, 112 (1939).
15. L.G. Cook, Z. Physik. Chem., B-42, 221 (1939).
16. O. Erbacher, Z. Physik. Chem., B-33, 47 (1936).
17. H. Götte, Z. Physik. Chem., B-40, 207 (1938).
18. O. Hahn, J. Chem. Soc., Pt. V, S259 (1949).
19. O. Hahn, 'Applied Radiochemistry', Cornell University Press, Ithaca, New York (1936).
20. G. Graue, Kolloid Chem., Beihefte 32, 403 (1931).
21. K. Zimens, Z. Physik. Chem., B-37, 231 (1937).
22. G. Tammann and A. Sworykin, Z. anorg. u. allgem. Chem., 176, 46 (1928).

23. R. Jagitsch, Z. Physik. Chem., B-33, 196 (1936).

24. O. Hahn, Proc. Internat. Symposium 'Reactivity of Solids' Gothenberg (1952) Pt. I, p. 21.

25. K. Zimens, Z. Physik. Chem., A191, 1 (1942).

26. A.C. Wahl and N.A. Bonner, 'Radioactivity Applied to Chemistry', John Wiley & Sons, New York (1950) p. 284.

27. G.B. Cook and E.W. Prout, J. Inorg. Nucl. Chem., 3, 255 (1956).

28. G.M. Zhabrova, S.Z. Roginskii, and M.D. Shibanova, Radiokhimeya, 4, 355 (1962).

29. W.J. Price, 'Nuclear Radiation Detection', McGraw-Hill Book Co., New York (1958).

30. K. Siegbahn, 'Beta- and Gamma-ray Spectroscopy', North Holland Publishing Co., Amsterdam, (1955).

31. C. Gatrousis, R. Heinrich, and C.E. Crouthamel, 'Progress in Nuclear Energy', Series IX, Analytical Chemistry, Vol. 2, 1 (1961).

32. D.H. Wilkinson, 'Ionisation Chambers and Counters', Cambridge University Press (1950).

33. J.B. Birks, 'Scintillation Counters', McGraw-Hill Book Co., New York (1953).

34. S.C. Curran, 'Luminescence and Scintillation Counters', Academic Press, New York (1953).

35. Scintillation Spectrometry, Baird Atomic Inc., Cambridge, Mass. (1960).

36. J.V. Weszelszky, Physik Z., 28, 757 (1927).

37. J. Zehradnicek, Z. Physik, 61, 719 (1930).

38. R.D. Evans, Rev. Sci. Instr., 6, 99 (1935).

39. R.D. Evans, Phys. Rev., 39, 1014 (1934).

40. J.H. Carrigue, J. Phys. Radium, 7, 107 (1936).

41. L.F. Curties and F.J. Davis, J. Research Natl. Bur. Standards, 31, 181 (1943).

42. D.H. Taysum and M.A. Van Dilla, Nucleonics, 13, 68 (1955).

43. F.F. Momyer, Jr., 'The Radiochemistry of Rare Gases', NAS-NS 3025, National Academy of Sciences, National Research Council, Washington, D.C. (1960).

44. C.S. Wu and E. Segrè, Phys. Rev., 67, 142 (1945).

45. W.S. Eggebert, Naturwissenschaften, 31, 491 (1943).

46. C.D. Coryell and N. Sugarman, 'Radiochemical Studies: The Fission Products', McGraw-Hill Book Co., New York (1951) Book II.

47. W. Bernstein and R. Ballentine, Rev. Sci. Instr., 21, 158 (1950).

48. E.K. Hyde and F.F. Momyer, Jr., J. Inorg. Nucl. Chem., 1, 274 (1955).

49. E.K. Hyde and H.B. Mathur, Phys. Rev., 96, 126 (1954).

50. R.B. Moore, M.Sc. Thesis, McGill University, Montreal (1959).

51. R. Overstreet and L. Jacobson, 'Radiochemical Studies: The Fission Products', Ed. C.D. Coryell and N. Sugarman, McGraw-Hill Book Co., New York (1951) Book II, Paper 67, p. 621.

52. C.R. Dillard, R.M. Adams, H. Finston, and A. Turkevich, 'Radiochemical Studies: The Fission Products', Ed. C.D. Coryell and N. Sugarman, McGraw-Hill Book Co., New York (1951) Book II, Paper 68, p. 624.

53. Chart of the Nuclides, 2nd Edition, July 1961, Issued by the Federal Minister of Nuclear Energy, Bad Godesberg, Federal Republic of Germany.

54. Nuclear Data Sheets, National Academy of Sciences, National Research Council, Washington, D.C.

55. A.M. Weinberg and E.P. Wigner, 'Physical Theory of Neutron Chain Reactors', University of Chicago Press (1958) p. 110.

56. P.C. Stevenson, H.G. Hicks, W. Nervik, and D.R. Nethaway, Phys. Rev., 111, 886 (1958).

57. J.S. Kirkaldy, Ph.D Thesis, McGill University, Montreal, (1953)

58. R.E. Bell, Private communication quoted by G. Grant, Ph.D Thesis, McGill University, Montreal (1961).

59. L.E. Glendenin and R.D. Metcalf, 'Radiochemical Studies: The Fission Products', Ed. C.D. Coryell and N. Sugarman, McGraw-Hill Book Co., New York (1951) Book II, Paper 278, p. 1625.

60. Handbook of Chemistry and Physics, 41st Edition, Chemical Rubber Publishing Co., Cleveland, Ohio (1959).

61. NBS Circular 539, 'Standard X-Ray Diffraction Powder Patterns', United States Dept. of Commerce, National Bureau of Standards, 4, 53 (1955).

62. G. Lunde and T. Barth, Z. Physik Chem., 122, 293 (1926).

63. L. Helmholz, Z. Krist., 95A, 129 (1936).

64. Conversion Tables for Thermocouples, Report No. 077989, Issue 2, Leeds & Northrup Co., Philadelphia, Pa.

65. B.D. Pate, L. Yaffe and J.S. Foster, Can. J. Chem., 36, 1691 (1958).

66. B.D. Pate and L. Yaffe, Can. J. Chem., 33, 15 (1955).

67. B.D. Pate and L. Yaffe, Ibid. 33, 610 (1955).

68. B.D. Pate and L. Yaffe, Ibid. 33, 929 (1955).

69. B.D. Pate and L. Yaffe, Ibid. 33, 1658 (1955).

70. B.D. Pate and L. Yaffe, Ibid. 34, 265 (1956).

71. A. Kjelberg and H. Taniguchi, Unpublished work 1958-1959, Radiochemistry Laboratory, McGill University.

72. R. Kelly, Can. J. Chem., 39, 664 (1961).

73. M.H. Lloyd and R.A. McNees, ORNL - 3228, Oak Ridge National Laboratory, Oak Ridge, Tenn., (1961).

74. R.A. Lad and T.F. Young, 'Radiochemical Studies: The Fission Products', Ed. C.D. Coryell and N. Sugarman, McGraw-Hill Book Co., New York (1951) Book III, Paper 317, p. 1833.

75. G.A. Cook, 'Argon, Helium and The Rare Gases', Vol. I, Interscience Publishers, New York (1961) p. 221.

76. J.S. Anderson, Proc. Internat. Symposium 'Reactivity of Solids', Gothenberg (1952) Pt. I, p. 37.

77. P.R. Bell, 'Beta- and Gamma-ray Spectroscopy', Ed. K. Siegbahn, North Holland Publishing Co., Amsterdam (1955) Chapter V.

78. G.A. Cook, 'Argon, Helium and The Rare Gases', Vol. I, Interscience Publishers, New York (1961)

79. Facts about 'Freon', Publication RI-156, Du Pont Company of Canada Limited, Kingston, Ontario.

80. J.H. Singleton and G.D. Halsey, Jr., J. Phys. Chem., 58, 330 (1954).

81. W.H. Sullivan, O. Johnson, and R. Nottrof, 'Radiochemical Studies: The Fission Products', Ed. C.D. Coryell and N. Sugarman, McGraw-Hill Book Co., New York (1959) Book II, Paper 139, p. 984.

82. A. Lottermoser and W. Peterson, Z. Physik. Chem., 133, 69 (1928).

83. E.N. Gapon, Lenin Acad. Agric. Sci., Gedroiz Research Inst., 'Fertilizers, Soil Management, Soil Science', Proc. Leningrad Dept., Part II, 83 (1938).

84. J.H. Singleton and G.D. Halsey Jr., Can. J. Chem., 33, 184 (1955).

85. A.F. Wells, 'Structural Inorganic Chemistry', Oxford University Press (1950) p. 271.

86. D. Gernez, C.R., 129, 1234 (1899).

87. N.V. Sidgwick, 'The Chemical Elements and Their Compounds', Oxford University Press, London (1950), p. 486.

88. L.G. Schulz, J. Chem. Phys., 18, 996 (1950).

89. L.G. Schulz, Acta Crystallographica, 4, 487 (1951).

90. R.J. Maurer, J. Chem. Phys., 13, 321 (1945).

91. S. Miyake, S. Hoshino, and T. Takenaka, J. Phys. Soc., Japan, 7, 19 (1952).

92. Z.G. Pinsker, L.I. Tatrinova, and V.A. Novikova, Structural Reports, 9, 146 (1942-44).

93. G.H. Herty, Am. Chem. J., 14, 110 (1892).

94. C.A. Jacobson (Editor), 'Encyclopedia of Chemical Reactions', Reinhold Publishing Corporation, New York (1951) Vol. V, p. 235.

95. F. Felix and P. Schmeling, Report No. EUR 111.e, Hahn-Meitner Institut für Kernforschung, Berlin.

96. J.M. Miller and J. Hudis, Ann. Rev. Nucl. Science, 9, 159 (1959).

97. R.J. Eden, Progress in Nuclear Physics, 6, 26 (1957).

98. N. Bohr, Nature, 137, 344 (1936).

99. E.P. Wigner and L. Eisenbud, Phys. Rev., 72, 29 (1947).

100. S.N. Ghoshal, Phys. Rev., 80, 939 (1950).

101. V.F. Weisskopf and D.H. Ewing, Phys. Rev., 57, 472 (1940).

102. V.F. Weisskopf and D.H. Ewing, Ibid. 57, 935 (1940).

103. V.F. Weisskopf and F.L. Friedman, Niels Bohr 70th Birthday volume, McGraw-Hill Book Co., New York, 1955.

104. V.F. Weisskopf and H. Feshbach, Phys. Rev., 76, 1550 (1949).

105. P.C. Gugelot, Phys. Rev., 81, 51 (1951).

106. R. Serber, Phys. Rev., 72, 1114 (1947).

107. B.G. Whitmore and G.E. Dennis, Phys. Rev., 84, 296 (1951).

108. E.R. Graves and L. Rosen, Phys. Rev., 89, 343 (1953).

109. P.C. Gugelot, Phys. Rev., 93, 425 (1954).

110. M. Shapiro, Phys. Rev., 90, 171 (1953).

111. R.E. Bell and H.M. Skarsgard, Can. J. Phys., 34, 745 (1956).

112. E.M. Toms and W.E. Stevens, Phys. Rev., 95, 1209 (1954).

113. R.E. Bell and T.M. Kavanagh, Can. J. Phys., 39, 1172 (1961).

114. H. Waffler, Helv. Phys. Acta, 23, 239 (1950).

115. M.G. Mayer and J.H.D. Jensen, 'Elementary Theory of Nuclear Shell Structure', John Wiley & Sons, New York (1955).

116. S. Fernbach, R. Serber, and T.B. Taylor, Phys. Rev., 75, 1352 (1949).

117. L.R.B. Elton, 'Introductory Nuclear Theory', Interscience Publishers, Inc., New York (1959).

118. B.B. Cunningham, H.H. Hopkins, M. Lindner, D.R. Miller, P.R. O'Connor, I. Perlman, G.T. Seaborg, and R.C. Thompson,
Phys. Rev., 72, 739 (1947).
Ibid. 72, 740 (1947).

119. W. Chupp and E.M. McMillan, Phys. Rev., 72, 873 (1947).

120. R. Thornton and R.W. Senseman, Phys. Rev., 72, 872 (1947).

121. R. Serber, Phys. Rev., 72, 114 (1947).

122. B.G. Harvey, Progress in Nuclear Physics, 7, 89 (1959).

123. M.L. Goldberger, Phys. Rev., 74, 1268 (1948).

124. G. Bernadini, E.T. Booth, and S.J. Lindenbaum,
Phys. Rev., 85, 826 (1952).
Ibid. 88, 1017 (1952).

125. G.C. Morrison, H. Muirhead, and W.G.V. Rosser,
Phil. Mag., 44, 1326 (1953).

126. V. De Sabbata, E. Manresi, and G. Puppi, Nuovo Cimento, 9(10), 1704 (1953).

127. G. Rudstam, Ph.D Thesis, University of Uppsala, Sweden (1956).

128. J.D. Jackson, Can. J. Phys., 34, 767 (1956).

129. N. Metropolis, R. Bivins, M. Storm, J.M. Miller, G. Friedlander, and A. Turkevich,
Phys. Rev., 110, 185 (1958).
Ibid. 110, 204 (1958).

130. R.E. Batzel, D.R. Miller, and G.T. Seaborg, Phys. Rev., 84, 671 (1951).

131. B. Dropesky and E.O. Wiig, Phys. Rev., 88, 683 (1952).

132. H.B. Mathur and E.K. Hyde, Phys. Rev., 96, 126 (1954).

133. R.B. Moore, Bull. Am. Phys. Soc., 5, 338 A4 (1960).

134. D.L. Anderson and M.L. Pool, Phys. Rev., 77, 142 (1950).

135. I.M. Ladenbauer, UCRL-8200, Radiation Laboratory, University of California, Berkeley, California (1958).

136. B. Dropesky, Ph.D Thesis, University of Rochester, Rochester, N.Y., (1953).

137. M. Ya Kuznetsova, V.N. Mekhedov, and V.A. Khalkin, Soviet Physics, JETP, 34(7), 759 (1958).

138. R.K. Gupta, Nuclear Phys., 14, 606 (1960).

139. L. Marquez and I. Perlman, Phys. Rev., 78, 189 (1950).

140. P. Aagaard, G. Andersson, J.O. Burgman, and A.C. Pappas, J. Inorg. Nuclear Chem., 5, 105 (1957).

141. G. Friedlander and W.C. Orr, Phys. Rev., 84, 484 (1951).

142. L. Winsberg, Phys. Rev., 95, 198 (1954).
Ibid. 95, 205 (1954).

143. D.J. Silvester and G.C. Jack, J. Inorg. Nuclear Chem., 24, 1181 (1962).

144. Johnson Matthey & Co., Limited, Chemical Division, London, England, Report on Matthey Spectrographically Standardised Cuprous Iodide, Laboratory No. 16624 (1960).

145. Y. Adda, G. Brebec, and Mlle V. Levy, Revue de Métallurgie, 58, 743 (1961).

146. D.J. Neil, Physics Division, Aluminium Laboratories Ltd., Kingston, Canada, Private Communication.

147. R.M. Sternheimer, Phys. Rev., 117, 137 (1959).

148. S.N. Ghoshal, Phys. Rev., 80, 939 (1950).

149. S. Meghir, Ph.D Thesis, McGill University, Montreal (1962).

150. J.W. Mellor, 'A Comprehensive Treatise on Inorganic and Theoretical Chemistry', Longmans, Green and Co., London, England, (1923) Vol. III, p. 204.

151. K.A. Kraus and F. Nelson, Proc. International Conference on the Peaceful Uses of Atomic Energy, Geneva (1955), Vol. 7, pp. 113-125.

152. D.R. Stull, 'Vapour Pressure of Pure Substances', The Dow Chemical Co., Midland, Michigan (1947).

153. C.J. Rodden, 'Analytical Chemistry of the Manhattan Project', First Edition, McGraw-Hill Book Co., New York (1950).

154. G.V.S. Rayudu, Ph.D Thesis, McGill University, Montreal, (1961).

155. A.G. Collins and J.W. Watkins, Anal. Chem., 31, 1182 (1959).

156. F.J. Welcher, 'The Analytical Uses of Ethylenediamine Tetra Acetic Acid', D. Van Nostrand Co., New York (1958).

157. G.R. Grant, Ph.D Thesis, McGill University, Montreal (1961).

158. D. Strominger, J.M. Hollander, and G.T. Seaborg, Rev. Mod. Phys. 30, 585 (1958).

159. L.A. Sliv and I.M. Band, 'Coefficients of Internal Conversion of Gamma Radiation, Part I and Part II, Academy of Sciences, U.S.S.R. (1958). (Issued in U.S.A. as Report 57 ICC kI and 58 ICC kI, Physics Department, University of Illinois, Urbana, Illinois.)

160. C.D. Broyles, D.A. Thomas, and S.K. Haynes, Phys. Rev., 89, 715 (1953).

161. S. Balestrini, Phys. Rev., 95, 1502 (1954).

162. M.L. Perlman and J. Welker, Phys. Rev., 95, 133 (1954).

163. A.C.G. Mitchell, J.O. Julliano, C.B. Creager, and C.W. Kocher, Phys. Rev., 113, 628 (1959).

164. R.J. Griffiths and R.M. Eisberg, Nuclear Phys., 12, 225 (1959).

165. H.P. Yule and A. Turkevich, Phys. Rev., 118, 1591 (1960).

166. R.W. Fink and E.O. Wiig, Phys. Rev., 96, 185 (1954).

167. I.M. Ladenbauer and L. Winsberg. Private Communication to B.G. Harvey. Progress in Nuclear Physics, I, 89 (1959).

168. R.A. Sharp, R.M. Diamond, and G. Wilkinson, Phys. Rev., 101, 1493 (1956).